AD-A211 661 THE PREPARATION AND PROPERTIES OF SUPERFINE METAL
PARTICLES(U) MARTIN MARIETTA LABS BALTIMORE MD
K BRIDGER 15 JUN 88 MML-TR-89-78C N00014-85-C-0637

UNCLASSIFIED F/G 11/7 NL

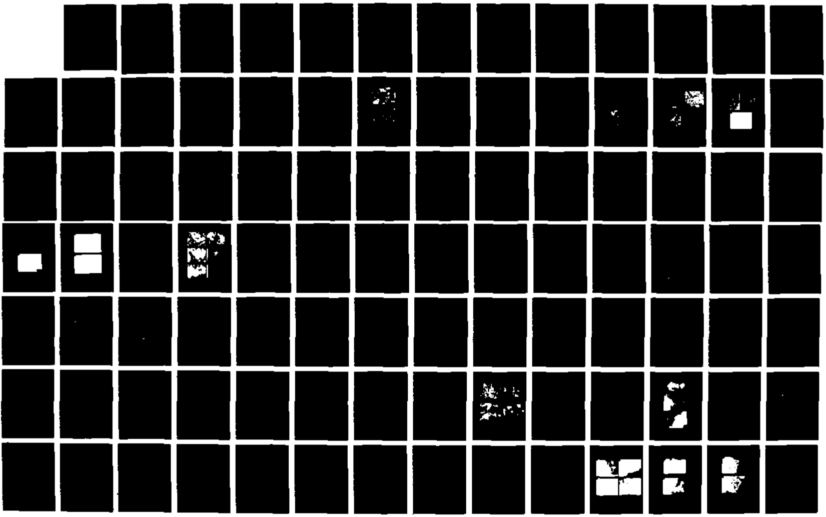

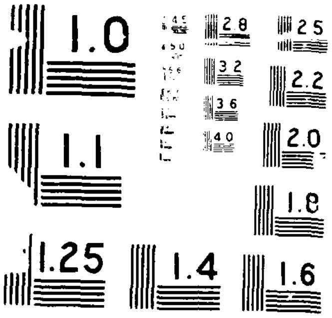
1.0
2.8
2.5
3.2
2.2
3.6
4.0
1.1
2.0
1.8
1.25
1.4
1.6

MML TR 89-78c

Final Report

Contract N00014-85-C-0637; NR 653-047

THE PREPARATION AND PROPERTIES OF SUPERFINE METAL PARTICLES

Martin Marietta Laboratories
1450 South Rolling Road
Baltimore, MD 21227

Final Report for Period 15 June 1985 - 15 June 1988

Approved for public release. Distribution unlimited. Reproduction in whole or in part is permitted for any purpose of the United States Government.

Prepared for

OFFICE OF NAVAL RESEARCH
800 N. Quincy Street
Arlington, Virginia 22217

REPORT DOCUMENTATION PAGE

READ INSTRUCTIONS
BEFORE COMPLETING FORM

1. REPORT NUMBER

2. GOVT ACCESSION NO.

3. RECIPIENT'S CATALOG NUMBER

4. TITLE (and Subtitle)
The Preparation and Properties of Superfine Metal Particles

5. TYPE OF REPORT & PERIOD COVERED
Final 6/15/85 - 6/15/88

6. PERFORMING ORG. REPORT NUMBER
MML TR 89-78c

7. AUTHOR(s)
Keith Bridger

8. CONTRACT OR GRANT NUMBER(s)
N00014-85-C-0637

9. PERFORMING ORGANIZATION NAME AND ADDRESS
Martin Marietta Laboratories
1450 South Rolling Road
Baltimore, MD 21227

10. PROGRAM ELEMENT, PROJECT, TASK AREA & WORK UNIT NUMBERS

11. CONTROLLING OFFICE NAME AND ADDRESS
Office of Naval Research
800 N. Quincy Street
Arlington, VA 22217

12. REPORT DATE

13. NUMBER OF PAGES
87

14. MONITORING AGENCY NAME & ADDRESS (if different from Controlling Office)

15. SECURITY CLASS. (of this report)
Unclassified

15a. DECLASSIFICATION DOWNGRADING SCHEDULE

16. DISTRIBUTION STATEMENT (of this Report)

Approved for public release; distribution unlimited.
Reproduction in whole or in part is permitted for any purpose of the United States Government.

17. DISTRIBUTION STATEMENT (of the abstract entered in Block 20, if different from Report)

18. SUPPLEMENTARY NOTES

19. KEY WORDS (Continue on reverse side if necessary and identify by block number)

Magnetic properties, superfine iron particles

20. ABSTRACT (Continue on reverse side if necessary and identify by block number)

Superfine iron and iron alloy particles have been prepared by reduction from the parent oxide. The superfine iron particles were rather uniform and cubic in shape, with sides ~500Å. The coercivities of these particles depended on reduction temperature. In particular, too high a reduction temperature led to sintering of the particles with a loss in coercivity. This effect could be overcome by coating the oxide particles with sodium silicate

20. (Continued)

prior to reduction. Coercivities as high as 1100 Oe were obtained at 4 K, whereas room temperature coercivities peaked at 700-900 Oe. The coercivities of the coated iron particles were independent of packing fraction in a polymer matrix. The particles were found to be porous under certain reduction conditions. However, this porosity collapses if the reduction is run for long enough at a high enough temperature. The final particles were essentially single crystallites. The kinetics of the reduction are complex and could not be adequately described by simple models. Rate constants estimated from the data were much lower than those reported in the literature.

The alloy particles were prepared by the reduction of ferrites which did not have highly uniform shapes. The alloy particles, in turn, were not as uniform as the iron particles. The coercivities of the alloy particles reached a maximum of 600-700 Oe and appeared to correlate with the degree of crystallinity as measured by x-ray diffraction. Particles reduced at low temperatures appeared amorphous to x-rays and had relatively low coercivities, which might suggest the presence of residual oxide, but Mossbauer spectra indicated the iron to be in its zero valent state. As the reduction temperature increased, bcc peaks became apparent and the coercivities increased. Reduction of the ferrite particles proceeded via a single-step process and was much faster than that of the hematite particles. If a suitable combination of elements yielding higher coercivities can be found, then this route would form the basis for future research and development, and could conceivably result in a superior recording material.

SUMMARY

Superfine iron and iron alloy particles have been prepared by reduction from the parent oxide. The superfine iron particles were rather uniform and cubic in shape, with sides ~500Å. The coercivities of these particles depended on reduction temperature. In particular, too high a reduction temperature led to sintering of the particles with a loss in coercivity. This effect could be overcome by coating the oxide particles with sodium silicate prior to reduction. Coercivities as high as 1100 Oe were obtained at 4 K, whereas room temperature coercivities peaked at 700-900 Oe. The coercivities of the coated iron particles were independent of packing fraction in a polymer matrix. The particles were found to be porous under certain reduction conditions. However, this porosity collapses if the reduction is run for long enough at a high enough temperature. The final particles were essentially single crystallites. The kinetics of the reduction are complex and could not be adequately described by simple models. Rate constants estimated from the data were much lower than those reported in the literature.

The alloy particles were prepared by the reduction of ferrites which did not have highly uniform shapes. The alloy particles, in turn, were not as uniform as the iron particles. The coercivities of the alloy particles reached a maximum of 600-700 Oe and appeared to correlate with the degree of crystallinity as measured by x-ray diffraction. Particles reduced at low temperatures appeared amorphous to x-rays and had relatively low coercivities, which might suggest the presence of residual oxide, but Mossbauer spectra indicated the iron to be in its zero valent state. As the reduction temperature increased, bcc peaks became apparent and the coercivities increased. Reduction of the ferrite particles proceeded via a single-step process and was much faster than that of the hematite particles. If a suitable combination of elements yielding higher coercivities can be found, then this route

would form the basis for future research and development, and could conceivably result in a superior recording material.

TABLE OF CONTENTS

LIST OF FIGURES

1. INTRODUCTION

1.1. Structure of this report

This report contains a description of work performed over a three-year period (June 1985 to June 1988). The work involved the study of various aspects of the preparation and properties of superfine iron and iron alloy particles, where the term superfine is used to denote sizes $< 0.1\ \mu m$. The report is divided into three main chapters:

- Preparation and properties of uniform iron particles
- Kinetics of the reduction of superfine hematite
- Preparation and properties of uniform iron alloys.

It is intended that each of these chapters be sufficiently complete and self-contained that they can be translated into three publications subsequent to acceptance of this report.

1.2. Background

Superfine iron and iron alloy particles are of tremendous interest from the point of view of their magnetic properties and use in recording media. Useful particles in magnetic recording should have high coercivities, H_c (to prevent accidental erasure) and large magnetizations, M_s (to provide a large signal). In practice most recording media consist of fine, single-domain particles embedded in a polymer film. The particles should have coercivities ($250 < H_c < 1200$ Oe) and magnetizations ($1250 < 4\pi M_s < 18850$ G)[1]. The most commonly used material is acicular $\gamma-Fe_2O_3$ particles with $250 < H_c < 400$ Oe and $4\pi M_s \sim 5$ kG.

The attractiveness of metal particles lies in their higher magnetizations and coercivities. These allow greater signal levels and resistance to demagnetization, both of which are crucial to increasing bit densities and recording higher frequencies. Like the oxide particles, metal particles should fall within that narrow size-range that yields single domains (too large → multi domain, too small → superparamagnetic behavior) and should be well dispersed, i.e., neither sintered nor bonded together. In addition to the two issues above, ultrafine metal particles are extremely reactive (in some cases pyrophoric) so they must be passivated against reaction with the atmosphere and the binder/solvent mixture in which they are cast. Alloy particles offer the potential for even higher coercivities and may also provide self-passivation of the particles.

2. PREPARATION AND PROPERTIES OF UNIFORM IRON PARTICLES

2.1. Summary

The work described in this section was performed during the period from June 15, 1985, to June 15, 1987. The objectives of the program were to synthesize ultrafine (<0.1 μm) iron particles and study their magnetic properties as a function of packing fraction in an inert medium. Because the work has been described in two reports[2,3] and two papers[4,5], only an overview will be presented in this section. The more detailed work on the kinetics of the reduction of the uniform submicron hematite particles will be described in Section 3 since it has not been previously published.

The issues studied were:

- The uniformity of the iron particles synthesized by the reduction of uniform iron oxide particles.
- The relationship between the morphology of the iron particles and that of the oxide.
- The tendency of the iron particles to sinter.
- The effect of packing fraction upon the magnetic properties of the iron particles in polymer films

The results are summarized as follows:

- Uniform cubic iron particles 0.05 μm on a side were prepared.
- The reduction was pseudomorphic depending on the reduction conditions.

- The iron particles formed were essentially nonporous.
- The magnetic properties and microstructure depend on coatings applied to the iron oxide particles prior to reduction. Sodium silicate was found to effectively inhibit sintering and permitted attainment of higher coercivities at higher temperatures.
- The magnetic properties do not correlate well with the sizes calculated from gas adsorption.
- The coercivities of iron particles dispersed in a polymer film are independent of packing fraction ($s < 0.2$).
- Pellets formed from Na_2SiO_3-coated iron particles had high coercivities, whereas pellets formed from uncoated iron particles had coercivities resembling that of bulk iron.

2.2. Experimental

2.2.1. General

The preparative work was done in 3 steps:

- Preparing and coating the iron oxide dispersions
- Freeze drying and reducing the coated (or uncoated) iron oxide particles
- Packaging the iron powder into suitable forms for the various analyses.

The iron powders formed were pyrophoric and, consequently, the last step was carried out in a glove box. The alloy particles described in section 6 were prepared in a similar manner except for the oxide preparation. This section will, therefore, also serve as a procedure for the work reported in Section 4 except where noted. All the experimental work is described in more detail on the following pages.

2.2.2. Preparation of uniform hematite particles

The preparation of uniform iron oxide particles has been extensively studied by Matijevic[6] and coworkers. Likewise, the preparation of monodispersed hematite[7-9], magnetite[10,11] and various ferrites[12,13] has been described. The particles produced ranged in size from less than 0.1 μm to several microns and included various shapes such as spheres, cubes, rods, and bipyramids. The uniformity of these particles is excellent as can be seen from the beautiful micrographs contained in Refs. 6-13. However, the solids contents of the dispersions are not very high.

The methods described in the references cited above can be categorized as either forced-hydrolysis or phase-*transformation reactions*. We chose to use the forced hydrolysis of ferric salts[7] to prepare our uniform oxide particles. In the forced-hydrolysis method, acidic solutions of ferric salts are aged at elevated temperatures to promote hydrolysis of the ferric ion. This leads to nucleation and growth of oxide particles. Particle size and shape are controlled by the nature and concentration of the anion, reaction temperature, and the aging time.

The solutions used in the preparations were made up from 'Baker Analyzed' grade of reagents, and all water was ion exchanged and then distilled. Stock solutions of the ferric salts were highly concentrated ($> 2\ M$) to avoid their aging prematurely.[7] Dilutions were made by addition of the ferric stock to the acid (if any), followed by the anion stock solution (if any) and then water. These diluted solutions were then filtered through 0.2-μm Nuclepore membranes and distributed in 10-cm^3 screw-capped culture tubes. The solutions were heated in a forced convection oven. After the reaction was complete, the samples were repeatedly centrifuged and redispersed in water in order to remove residual ions from the continuous phase.

Our study of the oxide preparation is described in Ref. 2. Because our objective was to study iron particles rather than the iron oxide preparations, we took advantange of prior art as much as possible. Reaction conditions were optimized and we began making larger batches (2 L). Two recipes, designated *Fe2O3-A* and *Fe2O3-B*, were adopted. The solution concentrations in the larger batches were as follows:

Fe2O3-A 0.05 M $Fe(ClO_4)_3$, 0.001 M HCl, and 0.01 M NaCl. The initial pH of the solutions was 2. The solutions were aged at 125°C for 24 h; after the washing cycle, each 2-L batch yielded approximately 5 g of solid.

Fe2O3-B 0.018 *M* $FeCl_3$ and 0.001 *M* HNO_3. The procedure was similar to *Fe2O3-A* except that these oxides were coagulated by the addition of 0.1 *M* KCl prior to washing.

Transmission electron micrographs (TEM's) of the iron oxide particles used in the reduction experiments are shown in Fig. 1. The *Fe2O3-A* sample is slightly larger than the *Fe2O3-B* sample, i.e., 550 Å vs 350 Å. The *Fe2O3-A* sample shown was used extensively in the first two years of this work[2,3]. In a subsequent test of the effect of particle size the sightly smaller oxide was reduced.

2.2.3. Reduction of hematite to iron.

The as-washed iron oxide dispersions described above were either freeze dried immediately or premixed with a coating material and then freeze dried. The coatings used include sodium silicate (Na_2SiO_3), polyvinylalcohol (PVA), silicic acid, barium dodecyl sulfonate, and silica. The coating materials were added as either

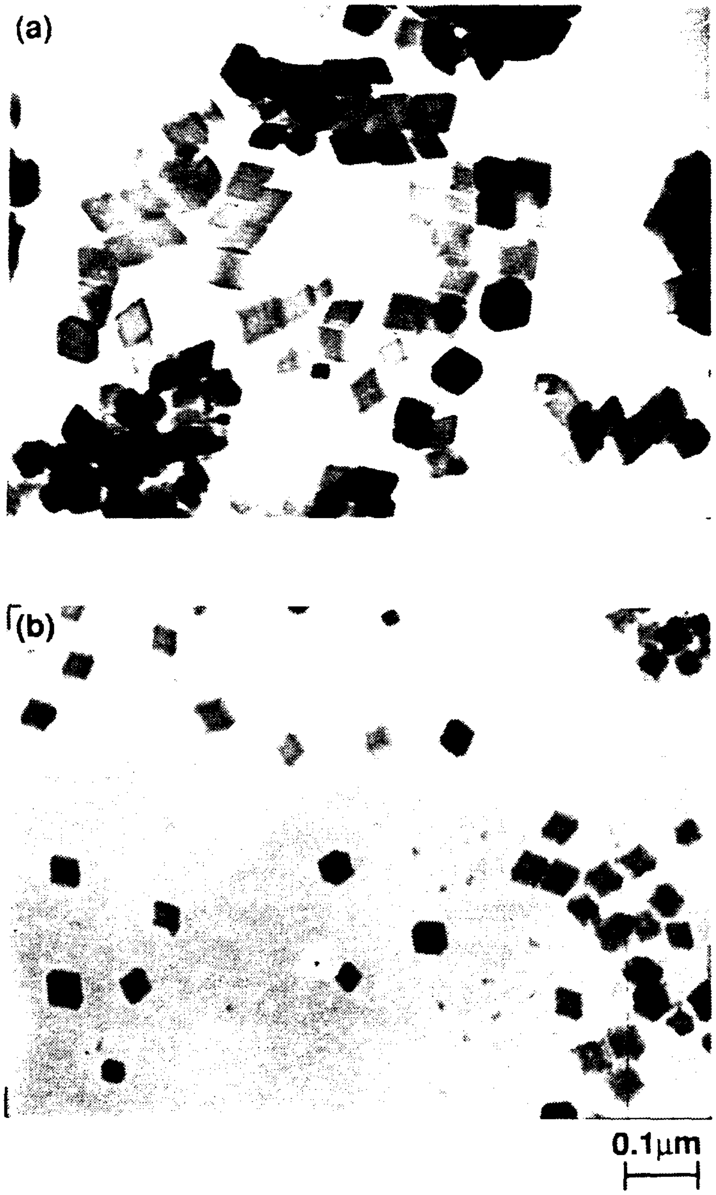

Figure 1. Transmission electron micrograph of hematite particles used in reduction experiments: a) *Fe2O3-A* and b) *Fe2O3-B*.

an aqueous solution (e.g., 0.1 M or 0.001 M Na_2SiO_3, 0.1% PVA, or 0.001M silicic acid) or a dispersion (e.g., silica).

The freeze-dried powders were reduced under hydrogen in a tube furnace. A typical heating cycle is shown in Fig. 2. When the run was completed, stopcocks at each end of the furnace tube were closed, and the entire tube was disconnected from the gas supply and transferred to a glove box. The tube was opened and the sample distributed under a nitrogen atmosphere. Samples for magnetic characterization were carefully weighed into a known weight of a polyurethane or epoxy resin. The slurry thus formed was milled for 20 min in a small shaker (Wigg-L-bug). A single stainless steel ball was used as the grinder. The dispersions thus formed were mixed with known weights of resin and hardener, and films were cast on microscope slides. The mass fraction and total weight of iron in each film were calculated from a mass balance. The iron particles on the slides were characterized by X-ray diffraction (XRD), Mossbauer spectroscopy, and magnetization measurements. Samples for electron microscopy were prepared by first milling a quantity of powder in toluene and then dispersing the particles using an ultrasonic bath. It should be noted that the dispersions formed were unstable with respect to coagulation, as is to be expected for ferromagnetic particles having diameters greater than 10-20 nm. Consequently, the grids for electron microscopy were prepared immediately after the ultrasound had been switched off. Sample holders for the gas adsorption analysis were filled in the glove box and transferred to the gas adsorption equipment without exposing the powder to air. Gas adsorption data were analyzed using the BET equation to calculate specific surface areas.

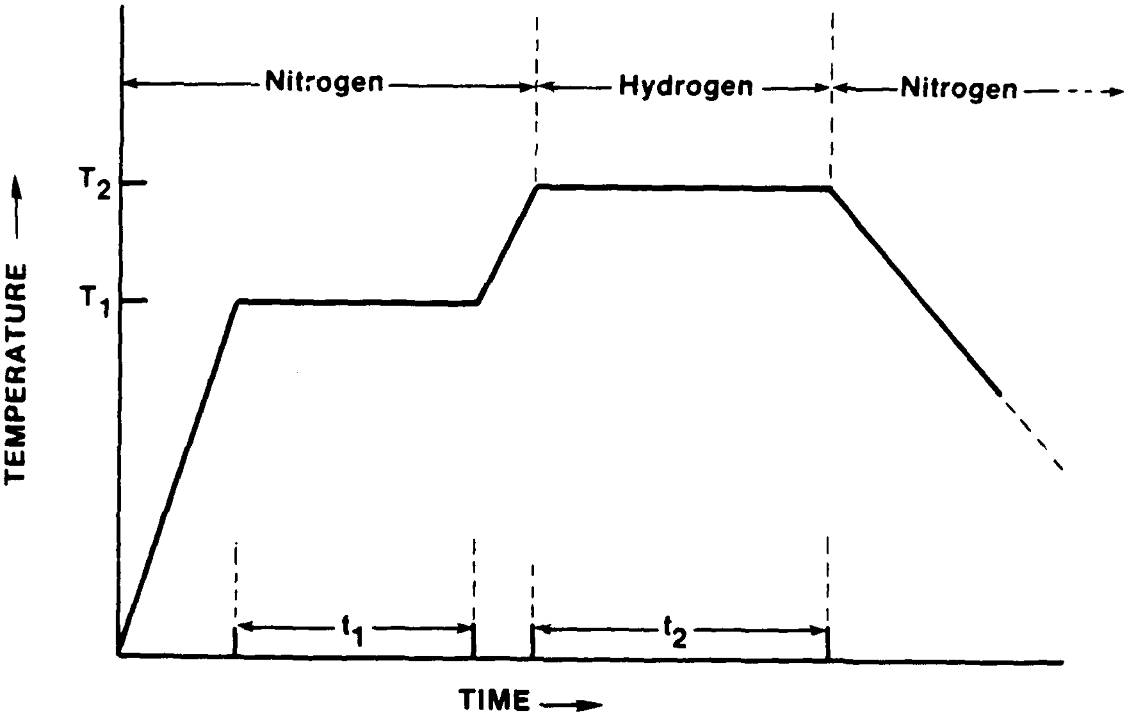

Parameter Values: $t_1 = 1$ h; $T_1 = 300^\circ$C

$1 \text{ h} \leqslant t_2 \leqslant 6$ h; $300^\circ\text{C} \leqslant T_2 \leqslant 600^\circ$C

Figure 2. Typical heating cycle for the reduction of iron oxides to iron.

2.3. Results

2.3.1. Particle Morphology

Figure 3 shows TEM's of iron particles together with their parent oxide (*Fe2O3-A*). The iron particles show little sintering and their size and shape are remarkably similar to the oxide. Such a transformation is referred to as pseudomorphic (i.e., without a change in morphology). Figures 4 and 5 show the effect of reduction conditions on uncoated and Na_2SiO_3-coated 350-Å oxide particles. Morphology is essentially maintained in these cases but some rounding and aggregation of the particles is observed after reduction. The lowest reduction temperature (325°C) did not yield iron in the coated sample and so its TEM is not shown. The most severe reduction conditions produced iron particles with a low coercivity (H_c = 230 Oe) in the uncoated case, whereas the Na_2SiO_3-coated iron particles had a coercivity of 550 Oe.

There is considerable interest in the porosity of ultrafine magnetic particles. Essentially it would be preferable for the particles to be nonporous since porosity reduces the saturation magnetization of each particle. However, commercial magnetic iron oxide particles formed by dehydroxylation and partial reduction of goethite (FeOOH) are porous[14-16] as are iron particles produced from FeOOH[16]. The pore and crystallite sizes of these iron particles depend upon the dehydroxylation temperature of the goethite particles[16]. As will be seen below, the particles prepared in this work show considerably less, and in many cases no, porosity.

Nitrogen adsorption data were used to study the volume and size of the pores. The data were analyzed using the t-plot technique,[17-19] whereby adsorbed volumes (V_L) are plotted against the expected adsorbed layer thickness (t) for the measured

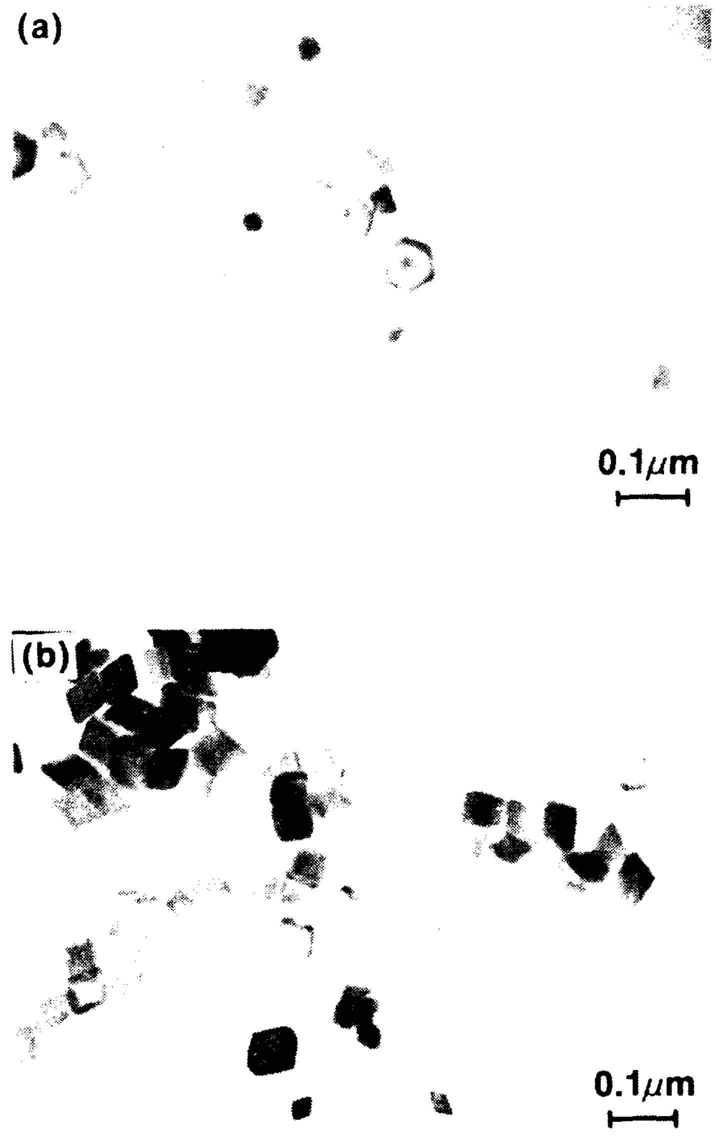

Figure 3. Transmission electron micrographs of a) iron particles reduced at 400°C for 1 h and b) the parent iron oxide particles.

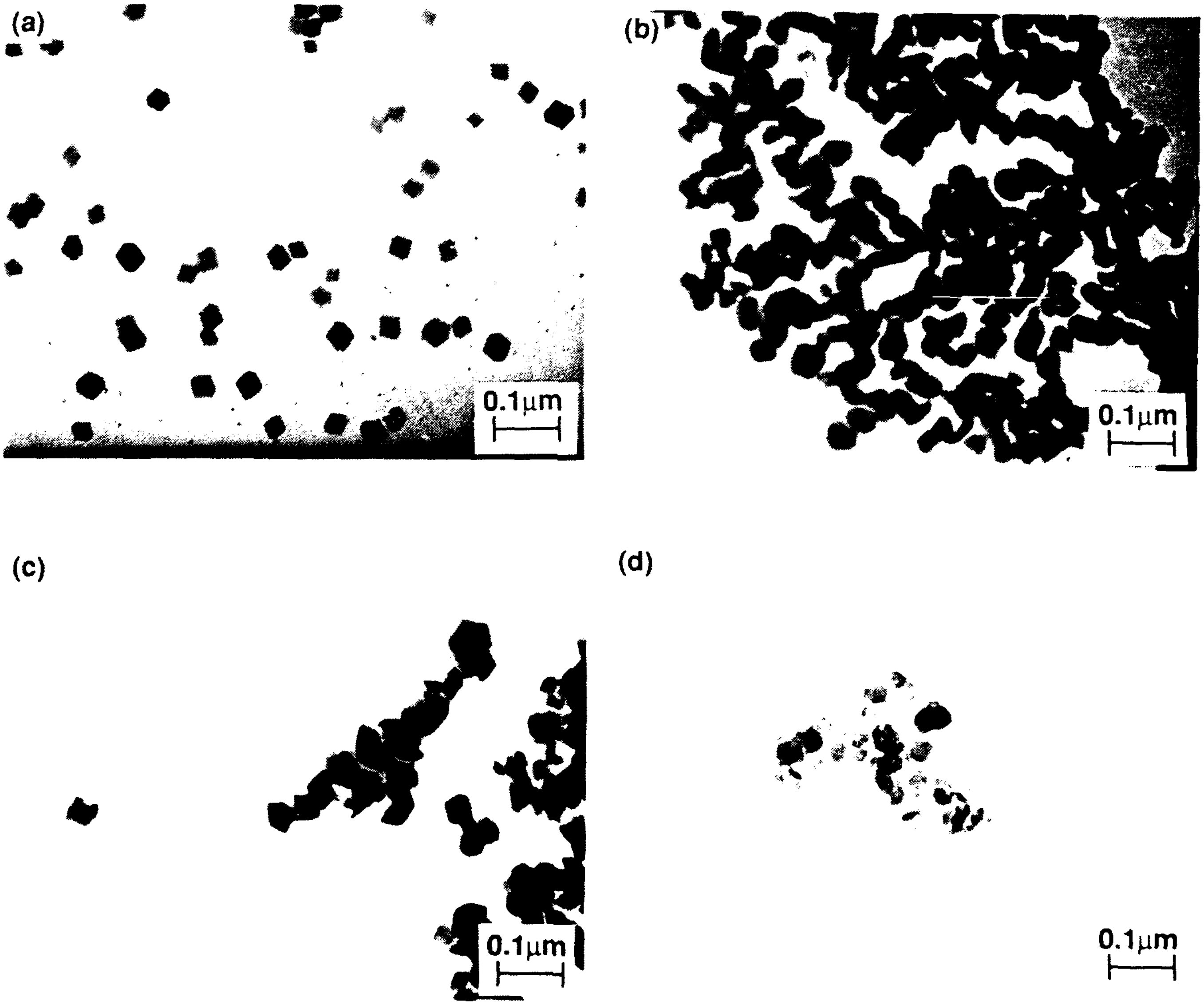

Figure 4. Transmission electron micrographs of a) the parent iron oxide particles, and uncoated iron particles reduced at b) 325°C for 3 h, c) 400°C for 1 h, and d) 400°C for 3 h.

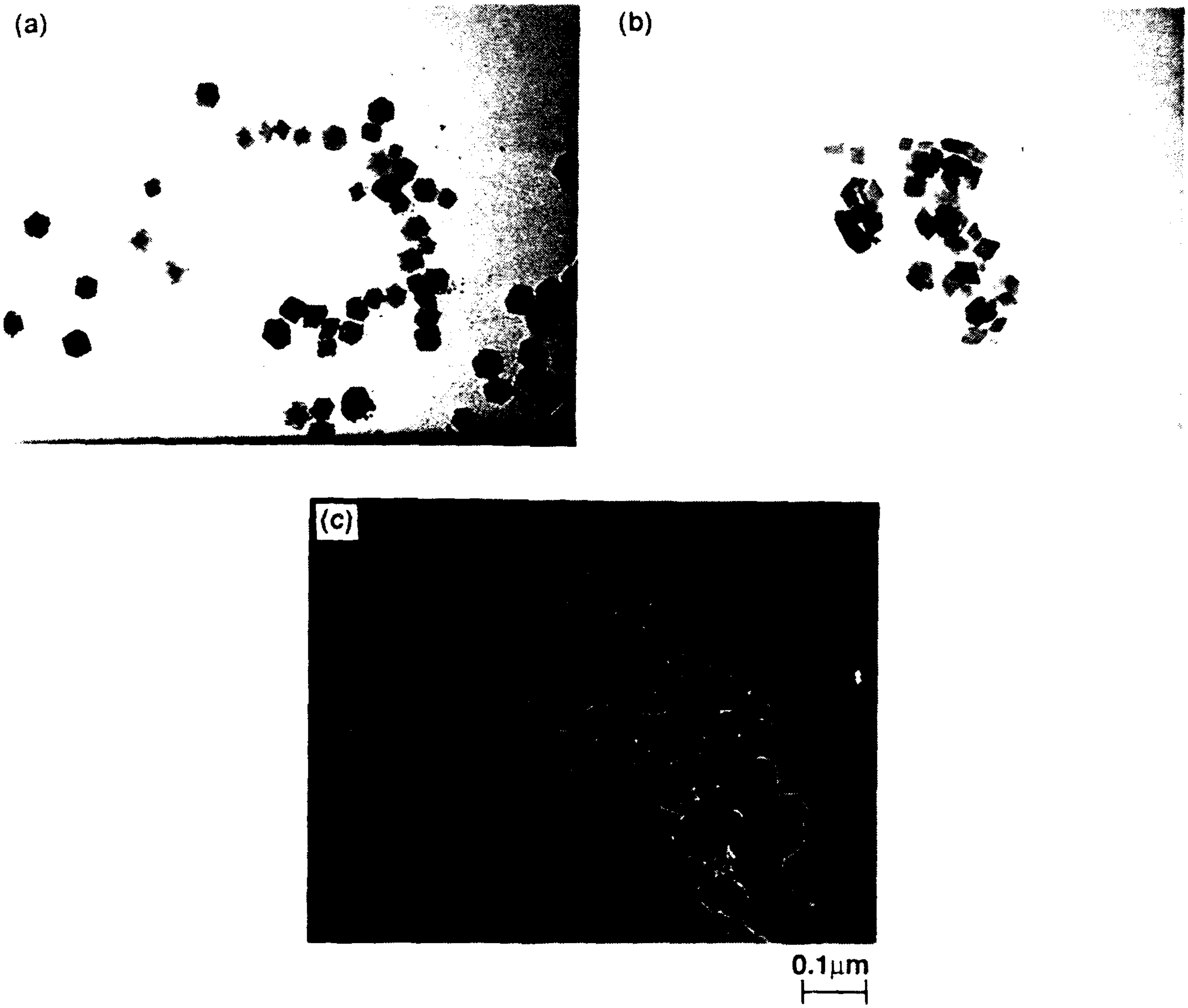

Figure 5. Transmission electron micrographs of a) parent Na_2SiO_3-coated iron oxide particles, and Na_2SiO_3-coated iron particles reduced at b) 400°C for 1 h and c) 400°C for 3 h.

partial pressure (p/p_0). The values for t have been collected from studies on known nonporous adsorbents and are given by the empirical expressions:

$$t = 3.54\left[\frac{5}{\ln(p_0/p)}\right]^{\frac{1}{3}} \tag{1}$$

or

$$t = \left[\frac{13.99}{0.034 - \log(p/p_0)}\right]^{\frac{1}{2}} \tag{2}$$

In the schematic t-plots seen in Fig. 6, curve A is the expected linear plot for a nonporous sample. Its slope is equal to the surface area (Σ) of the sample because:

$$vL = \Sigma t. \tag{3}$$

Curve B shows a deviation from the straight line, indicating that more nitrogen is being taken up than would be expected from multilayer adsorption. Capillary condensation has set in at this point. At higher t values, the pores responsible for this phenomenon are filled and a new straight line shows the continuation of the multilayer adsorption on the remaining surface. Note that the surface area (slope) of the remaining (external) surface is lower than the initial surface area. Curve C shows the expected plot for a microporous sample. At low t values, all the narrow pores are being filled, giving rise to an apparently high surface area. When these pores are filled, the lower slope corresponds to the external surface alone.

Figure 7 shows the surface area of the iron oxide particles after different outgassing temperatures. A maximum area of 39 m^2/g is observed after degassing at 400°C. We expect this condition to correspond to maximum porosity if any exists. Figure 8 shows a t-plot for the iron oxide after heating to 400°C. The linearity of the plot indicates that the iron oxide is nonporous, and the slope yields a value of 35 m^2/g for the external surface area. Figure 9 shows the t-plot for Na_2SiO_3-

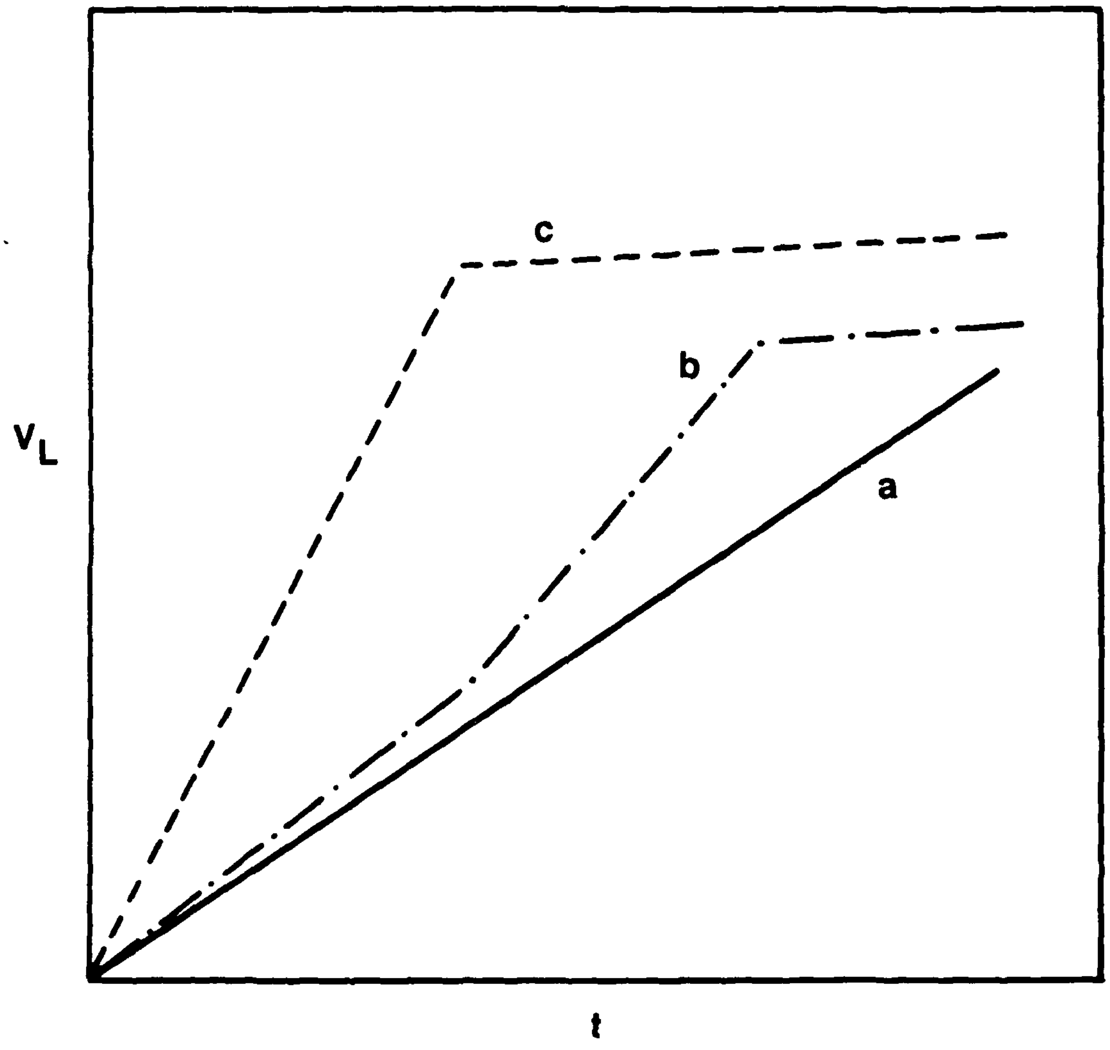

Figure 6. Schematic diagram of t-plots for a) nonporous, b) porous, and c) microporous materials.

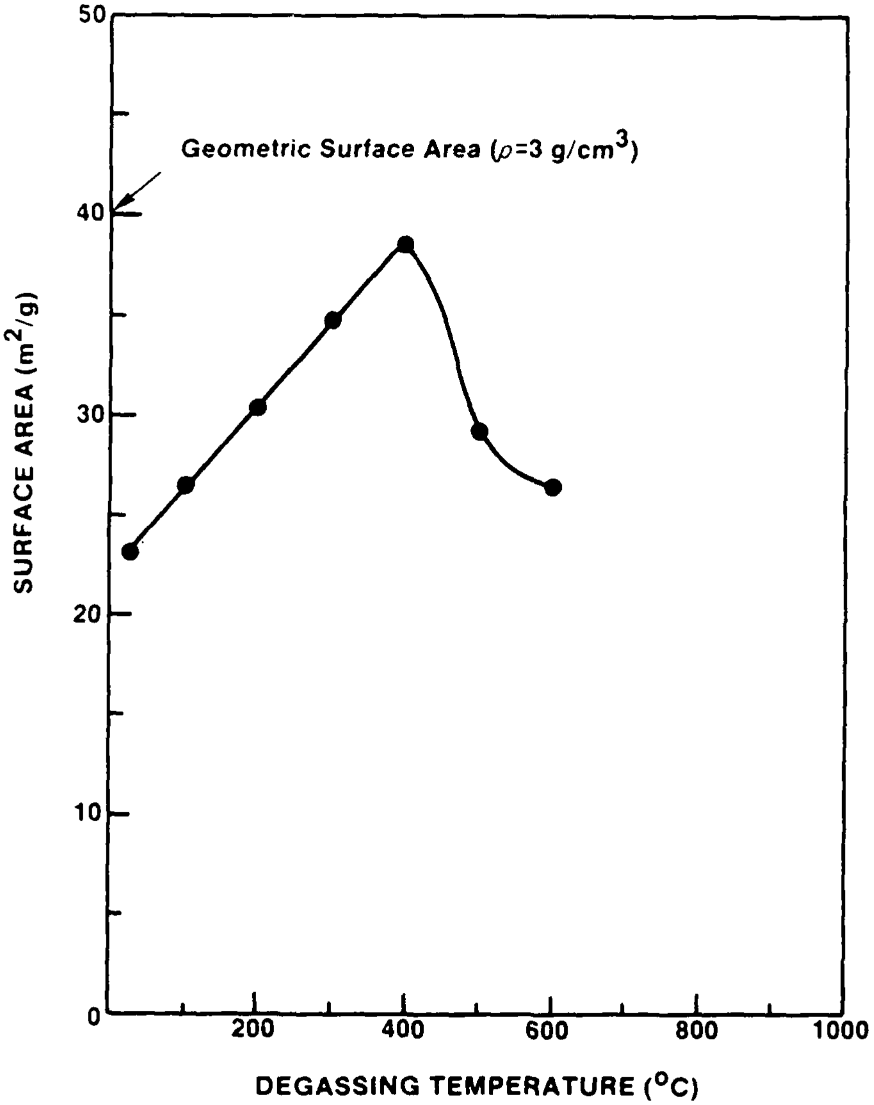

Figure 7. Surface area of iron oxide particles as a function of outgassing temperature.

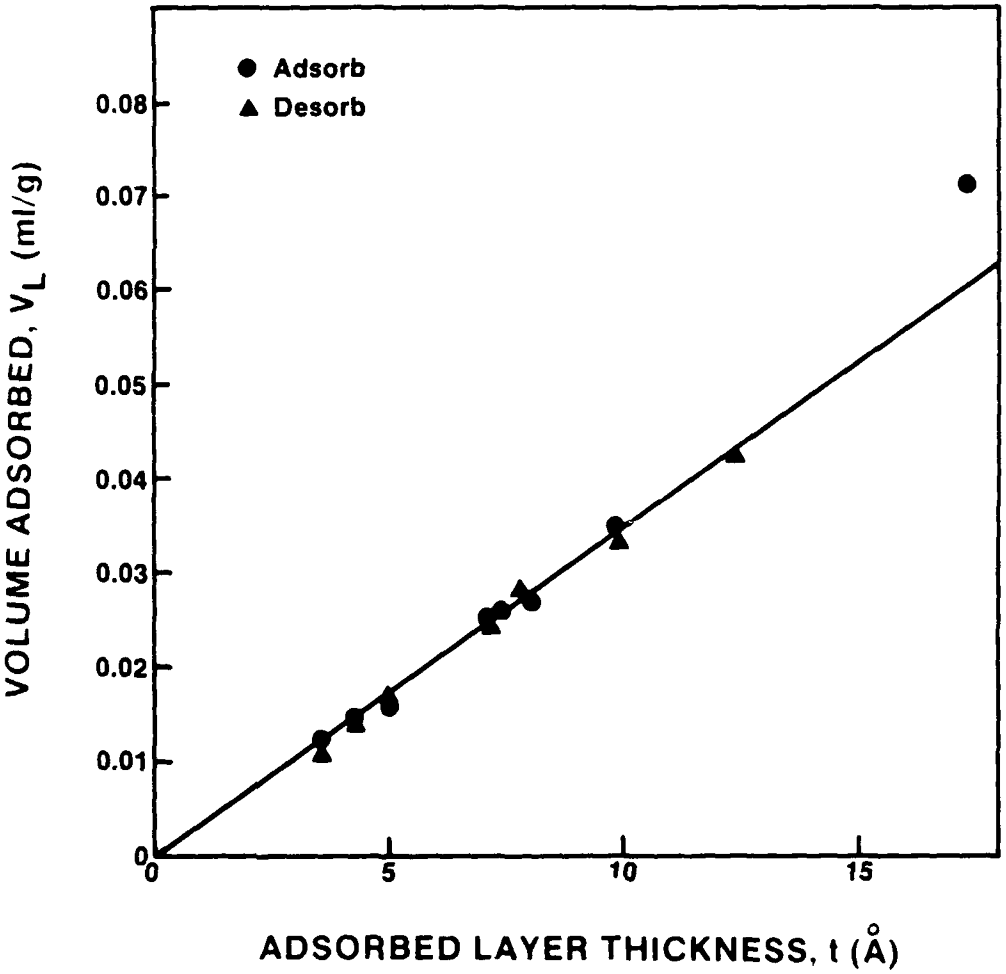

Figure 8. t-plot of iron oxide particles degassed at 400°C.

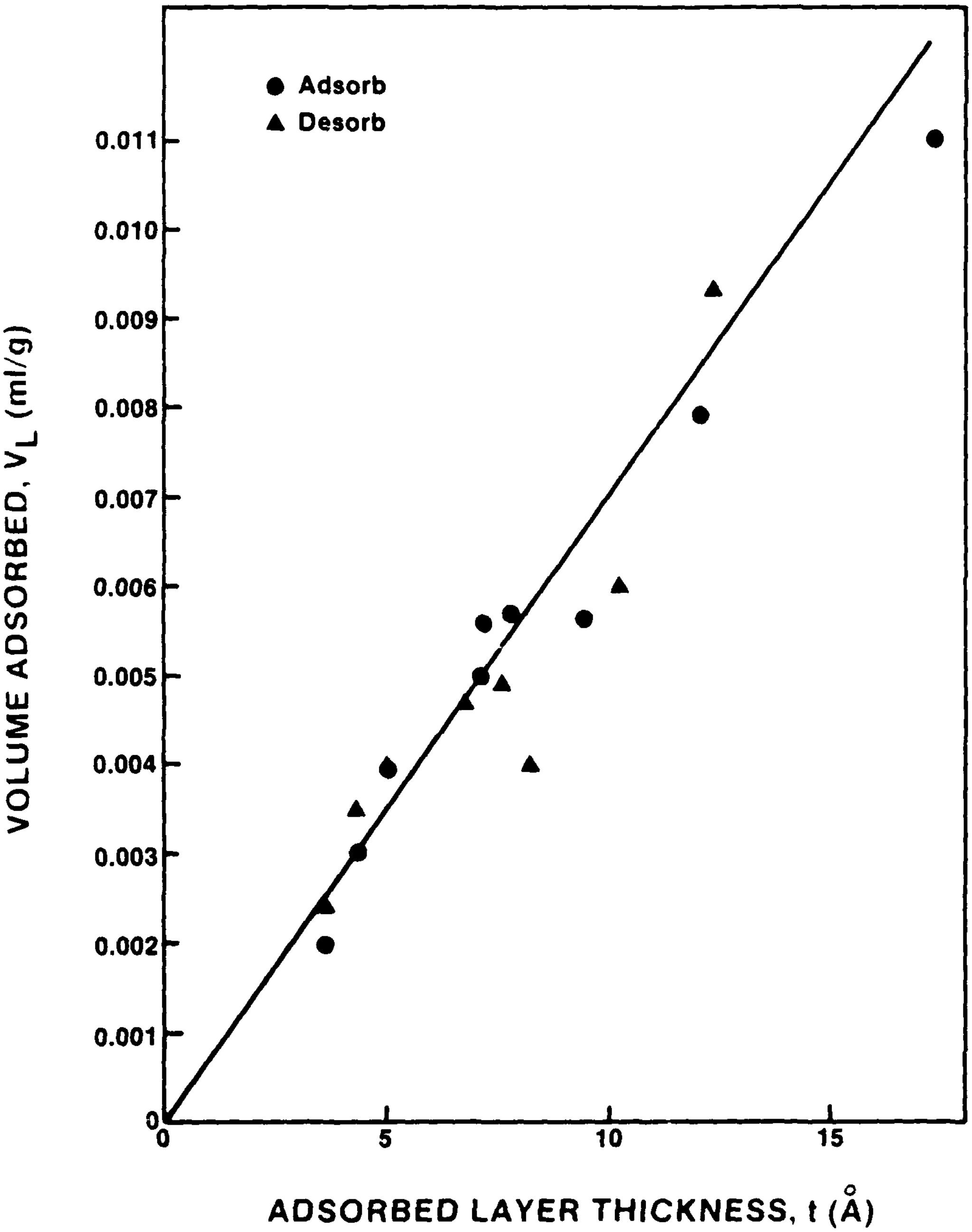

Figure 9. t-plot of Na_2SiO_3-coated iron particles reduced at 500°C.

coated iron particles prepared by reduction at 500°C. The plot shows no evidence of any porosity.

However, particles reduced at 300°C show some evidence of porosity at high t values, as shown in Figs. 10 and 11. Deviation at such high t values, i.e., $t > 10$ Å, indicates that the pores are large. Indeed, using the Kelvin equation

$$\ln(p/p_0) = \gamma \bar{v}_m / rRT \tag{4}$$

where γ and $\bar{v}_m$ are the surface tension and molar volume of liquid nitrogen, respectively, we predict the radius $(r+t)$ of the pores that begin filling to be ˜50 Å. Because the adsorption isotherms show no hysteresis, we conclude that the pores must be cone shaped and near the surface of the particles and might be thought of as a surface roughness. The volume of the pores is of the order of 0.05 cm^3/g. Note that no micropores are found, unlike the particles formed from goethite.[16] Thus, we conclude that the porosity in those iron particles originated from the oxide.

Some micropores are evident in iron samples reduced at 400°C. Figures 12 and 13 show t-plots for particles after reduction at 400°C for 3 and 1 hours, respectively. The 3-hour sample, which corresponds to the time used for the magnetic measurements, has only very slight porosity (˜0.003 cm^3/g). Its external surface area (14 m^2/g) is lower than the BET value (24 m^2/g) but compares well to the expected geometric value (15 m^2/g). Significant micropore volume (˜0.012 cm^3/g) is seen in the 1-hour sample, which has an external surface area of 23 m^2/g and a BET area of 49 m^2/g. Examination of the kinetic data (c.f. Section 3.2.3) reveals that after 1 hour at 400°C, reduction of the Na_2SiO_3-coated particles is expected to be between 50 and 75% complete. We believe that micropores are formed during

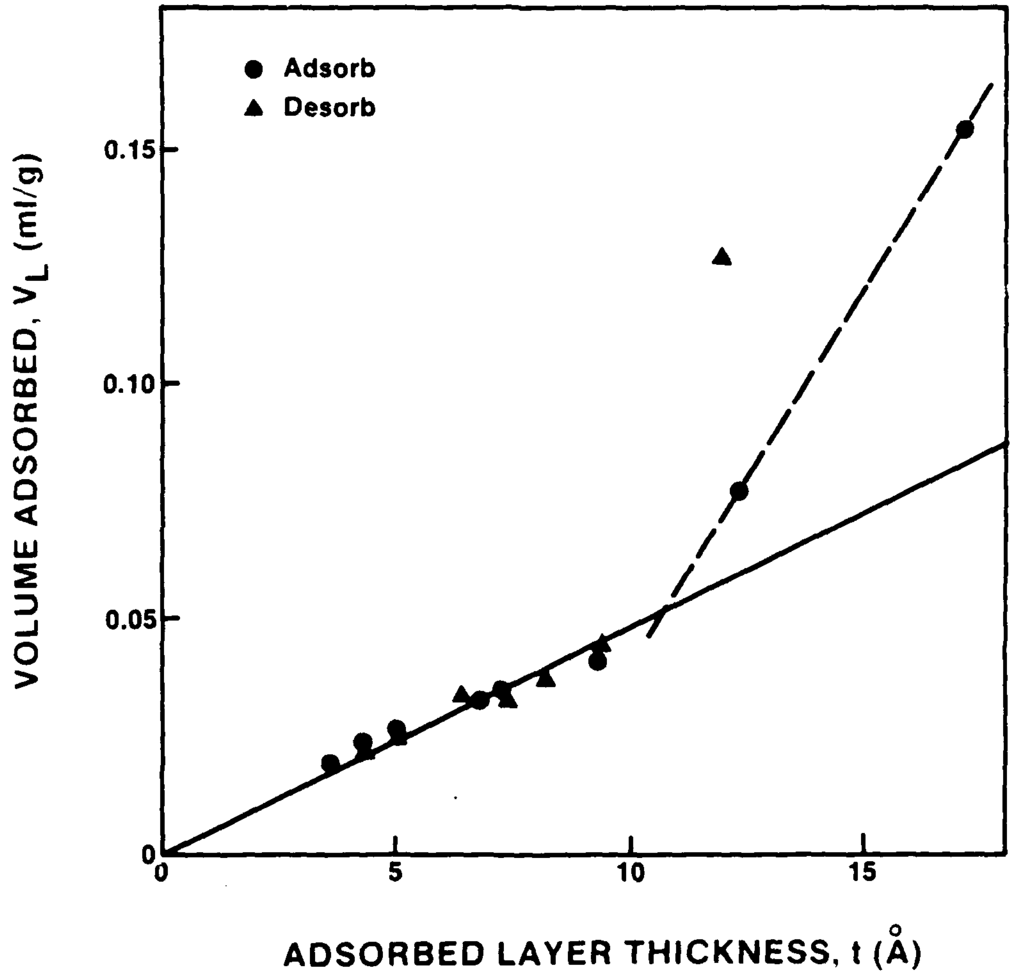

Figure 10. *t*-plot of uncoated iron particles reduced at 300°C.

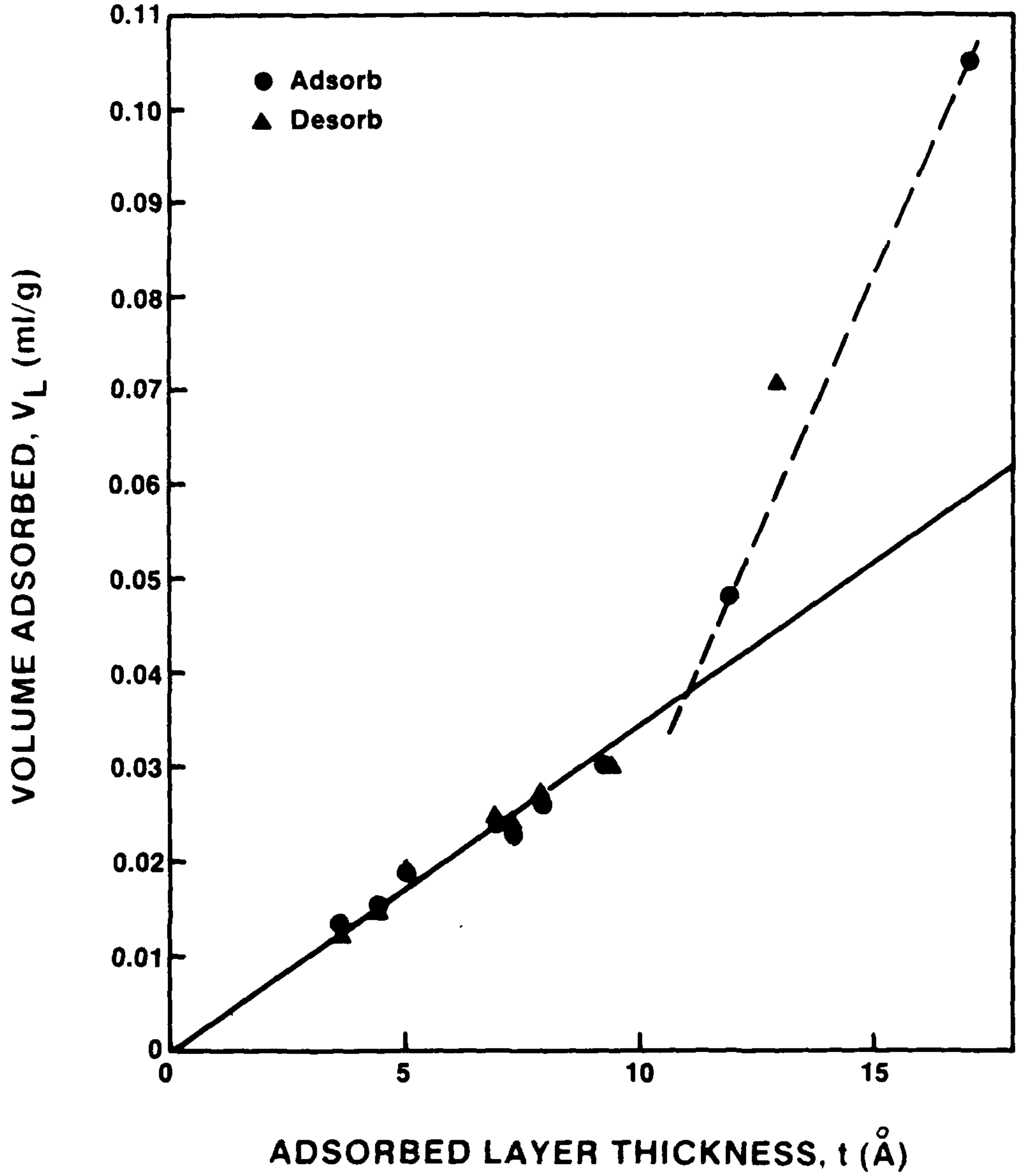

Figure 11. *t*-plot of Na_2SiO_3-coated iron particles reduced at 300°C.

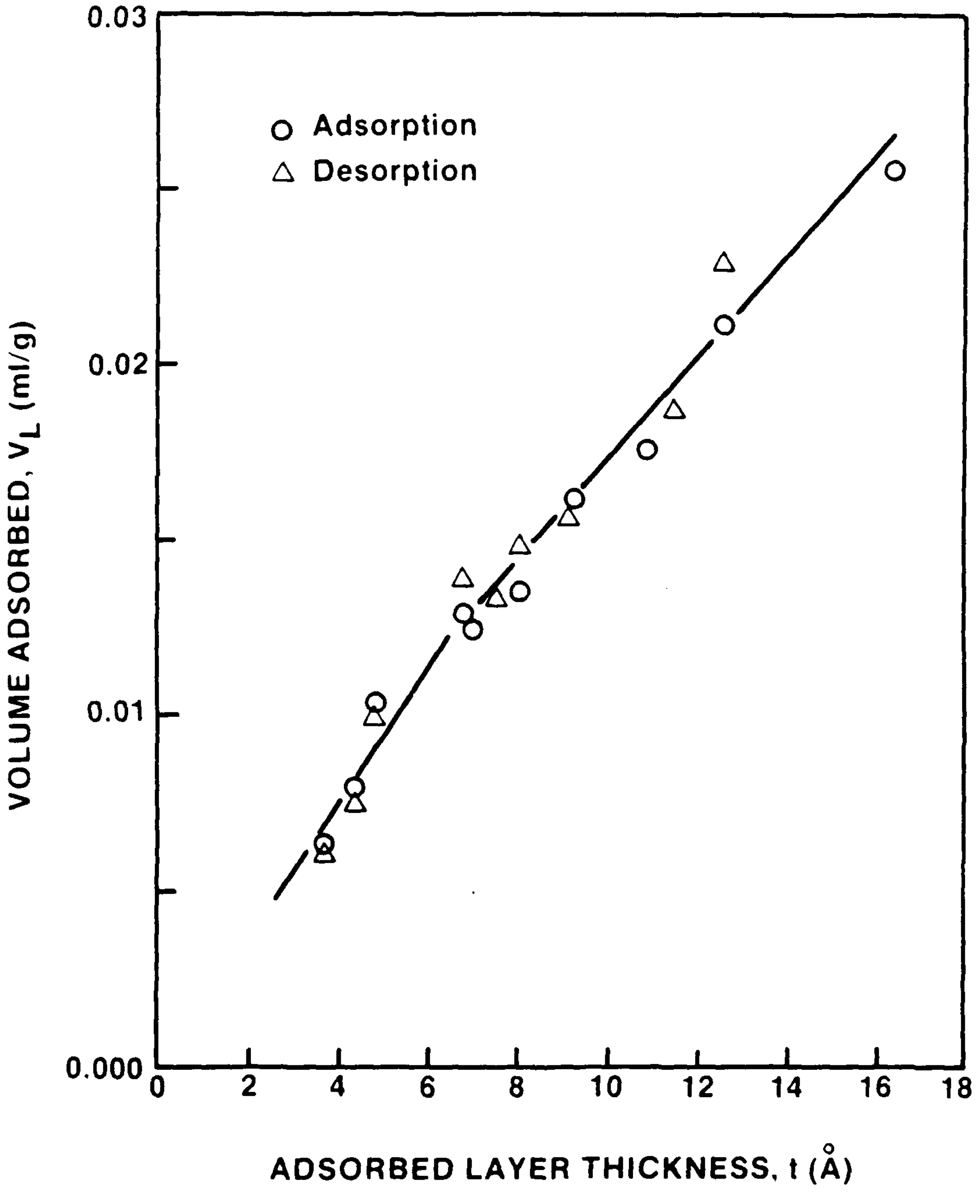

Figure 12. *t*-plot of Na_2SiO_3-coated iron particles reduced at 400°C for 3 h

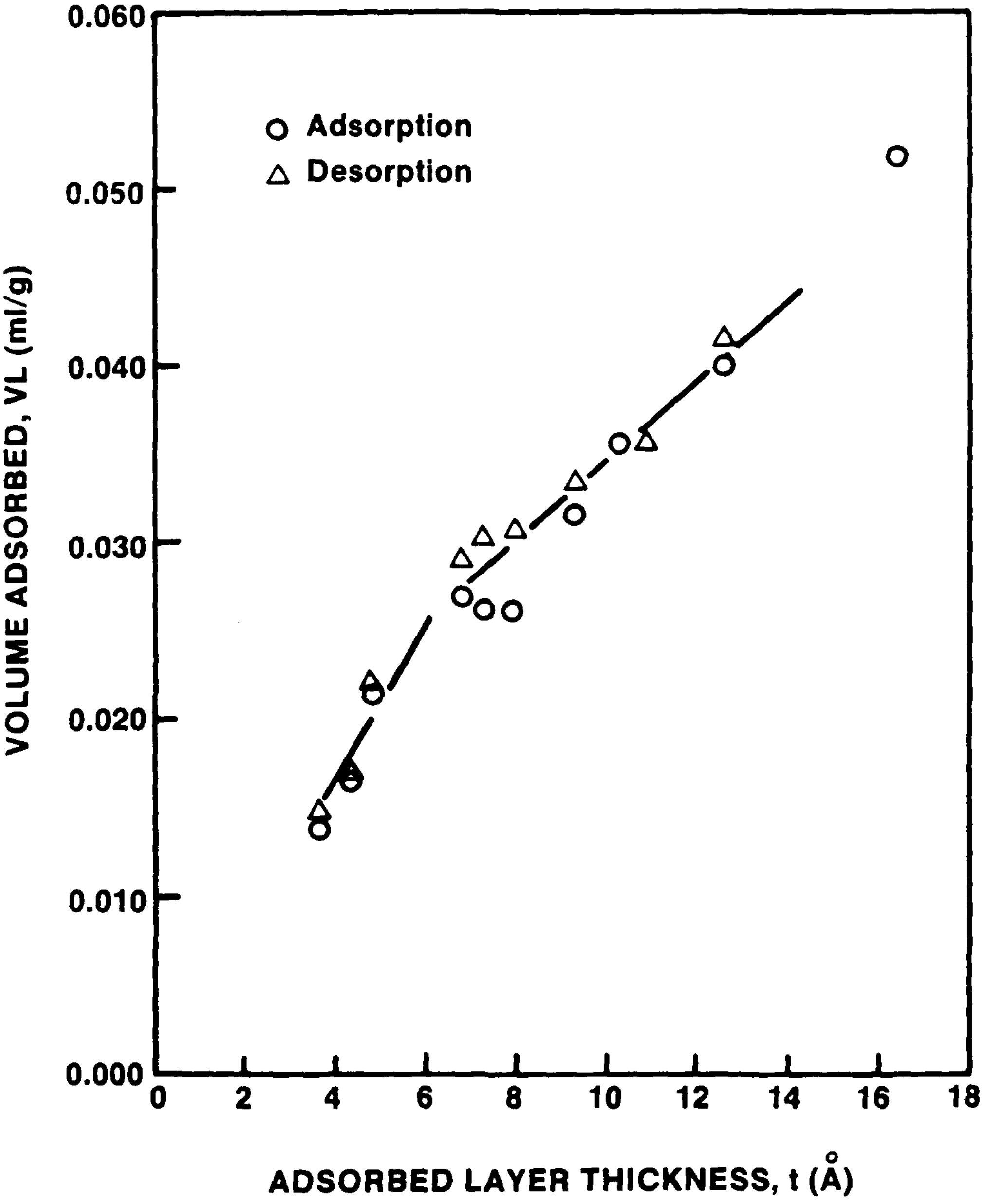

Figure 13. *t*-plot of Na_2SiO_3-coated iron particles reduced at 400°C for 1 h

the reduction, as might be expected since water is being evolved from the particles, but that as the reduction proceeds to completion this porosity collapses.

2.3.2. Magnetic properties

Samples of the particles dispersed in polymer films were transferred to the Johns Hopkins University (JHU) for magnetic characterization. Bulk magnetic properties of dilute films ($<1\%$ particles) were measured with a SQUID magnetometer from 6 to 300K with a field range of 0 to 50 kG. The variation of magnetic properties at ambient temperature with particle packing fraction was measured with a vibrating sample magnetometer. Conventional Mössbauer spectroscopy was used to determine the microscopic content of the magnetic particles on some but not all samples; samples with very low particle concentration are unsuitable for a meaningful Mössbauer measurement. Mössbauer spectroscopy provides a clear diagnosis of the phases of the particles, even after they are dispersed into a medium, and it confirmed that iron was the only phase in the film[2]. Incomplete reduction was found in the Na_2SiO_3-coated hematite samples reduced at 300°C in some instances; these samples were discarded.

As expected, coercivity, H_c, remanence, Mr, and saturation magnetization, M_s, all depend on temperature. Saturation values were obtained by taking measurements on the dilute films ($< 1\%$ particles) at 6K; at 300K, the values are lower but are within 20% of those at 6K. The coercivities of the dilute films largely depend upon the degree of aggregation in the particles; the more aggregated the particles, the lower the coercivity. Figure 14 demonstrates the effectiveness of Na_2SiO_3 in preventing loss of coercivity at the higher reduction temperatures. Barium dodecyl sulphonate was also found to be effective (as had been reported earlier[20]), but polyvinylalcohol, and silicic acid were ineffective[2,4]. The retention of

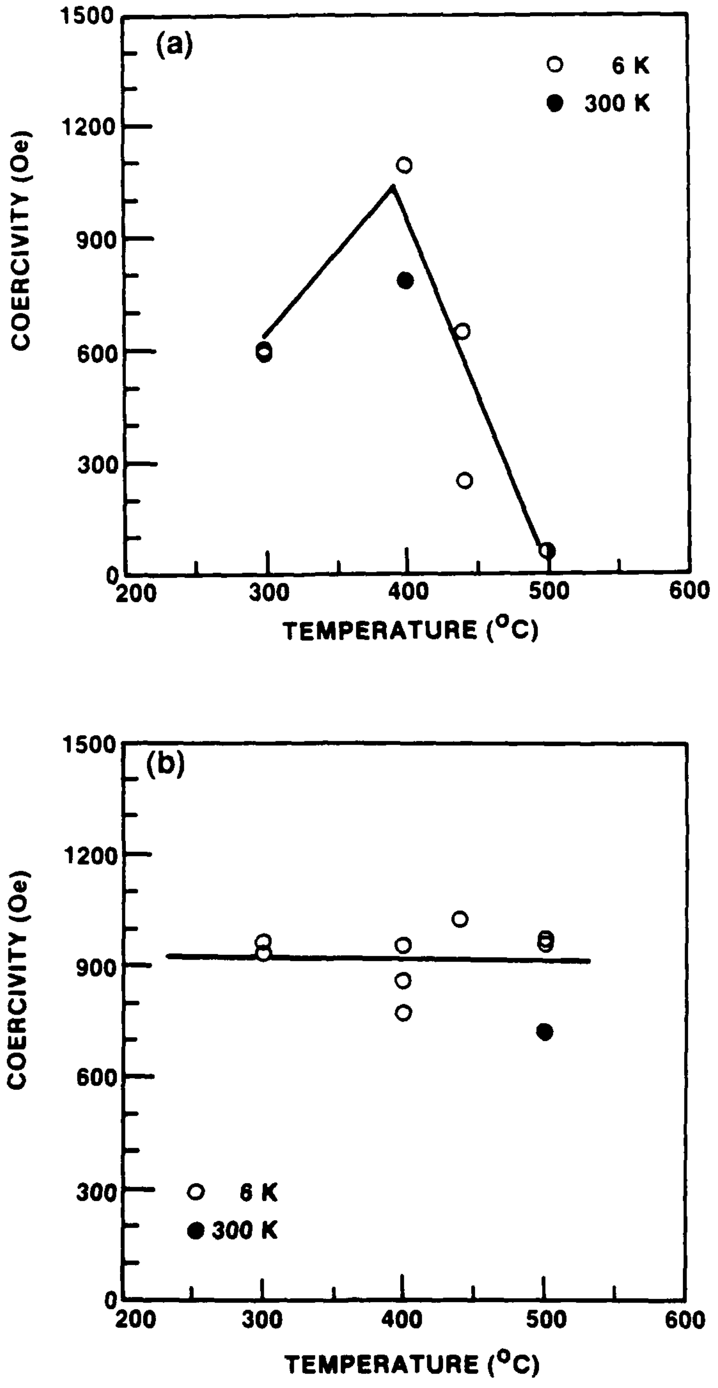

Figure 14. Coercivities of dilute films of a) uncoated and b) Na_2SiO_3-coated iron particles as a function of reduction temperature.

high coercivities at the higher reduction temperatures with the Na_2SiO_3-coated iron particles appears to correlate with the microstructure. Electron micrographs of iron particles coated with Na_2SiO_3, as shown in Fig. 5 and in Refs. 2 and 4, indicate little or no sintering between the particles. Electron micrographs of uncoated iron particles reduced at 500°C exhibited signs of sintering[2], and the uncoated particles shown in Fig. 4 appear more aggregated than their Na_2SiO_3-coated counterparts. On the other hand, it should be noted that comparison of the coercivity and BET surface area behaviors of the uncoated and sodium-silicate-coated particles has shown no correlation between the two measurements.

The large coercivities observed in the dilute films depend upon the iron particles being isolated from each other. If contact occurs between the particles, they begin to behave as dimers, trimers, etc., until in some limiting case a network has built up and the particles behave as one large particle, i.e., like bulk iron. Figure 15 shows the coercivities of iron particles dispersed in a polymer film plotted as a function of mass fraction, s, of the particles in the film. Also included are values obtained from pressed pellets of the particles, i.e., $s \to 1$. It is seen that H_c for both the uncoated and Na_2SiO_3-coated particles is independent of s for $s < 0.2$. This is quite reasonable since, assuming a density of 7.8 g/cm^3, $s = 0.2$ corresponds to a volume fraction of particles, f, of only 0.031. However, it should be noted that at this concentration the films have become brittle and no longer maintain the shiny surface seen at the lower concentrations. The pellet made from the uncoated iron particles has a very much lower coercivity -- almost as low as bulk iron. The pellet made from the Na_2SiO_3-coated particles has a coercivity of 425 Oe -- only slightly lower than that of the films. We believe that the coating prevents contact between the particles, allowing them to behave as though they were isolated.

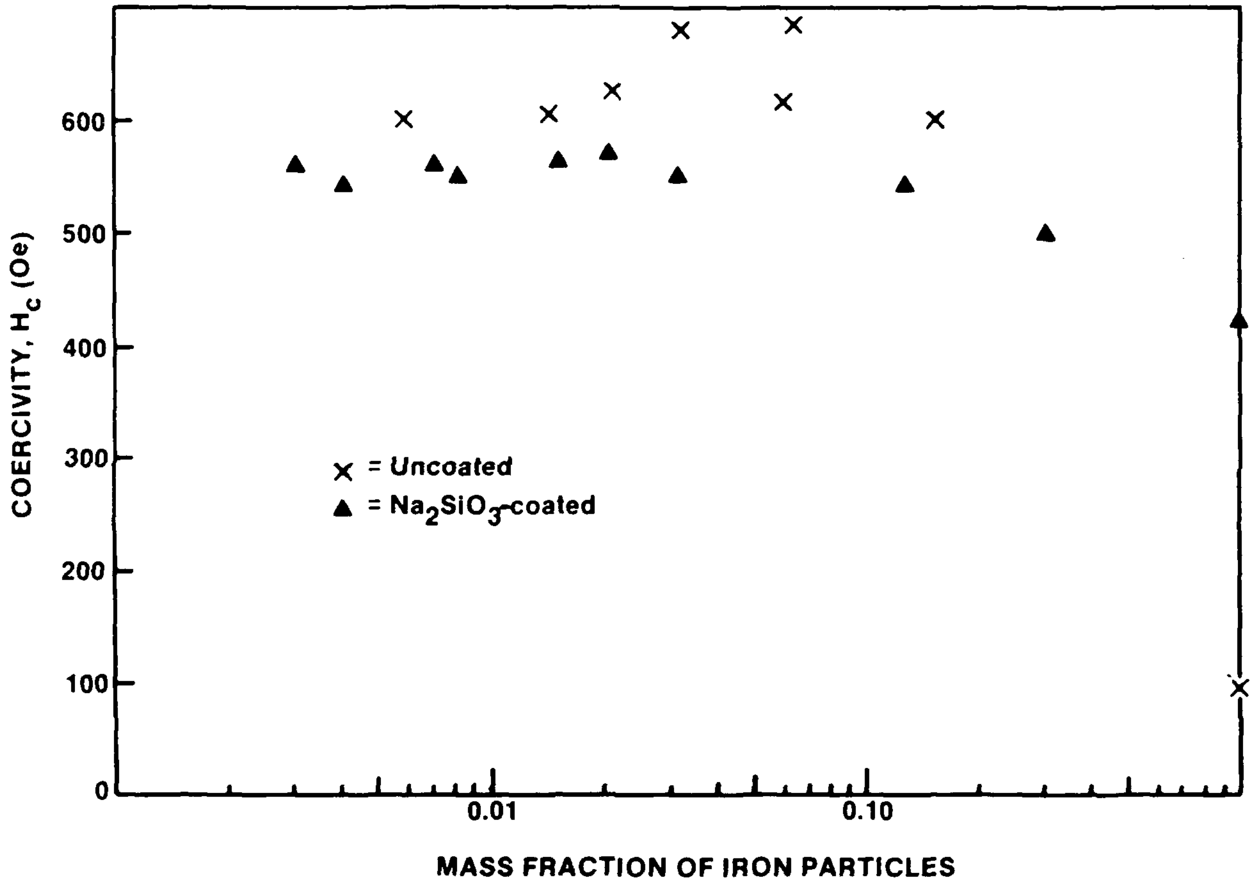

Figure 15. Coercivities of iron particles dispersed in a polymer film plotted as a function of mass fraction s of the particles in the film.

Figure 16 is a TEM of a cross section of a thinned polymer film containing the iron particles. It is apparent that the cubic shape has not been maintained and that the size of the particles has been reduced. The small particles in the photograph are only 10-20 nm. However, they do have some straight edges and 90° corners as might be expected from cubes that are being "eaten away". It is still unclear whether the iron cubes react with the polymer film or are etched by the ion beam during milling. An electron diffraction pattern from the area shown in Fig. 16 corresponds to iron (cubic, $a = 2.82$ Å), which is to be expected since an XRD pattern of the whole film showed α-Fe as the only phase. In the dark-field image of this area with the aperture selectively viewing the 110 diffraction line (Fig. 16b), the particles are essentially single crystals. This is apparent from the high contrast and the fact that whole particles show up in the dark-field image. The dark-field image also resembles the cubic shapes from which the more irregular particles evolved.

Figure 17a is a scanning electron micrograph (SEM) of a pellet pressed from uncoated iron particles and immediately transferred from the glove box to the microscope chamber. The pellet surface initially was shiny but it rapidly dulled during the transfer. The surface shown in the SEM is rough and heterogeneous although the fine particulate nature of the iron powder has disappeared except for some very fine pores. The latter occurred without the application of heat. The surface of an equivalent pellet pressed from Na_2SiO_3-coated particles (Fig. 17b) contains numerous cubic, platelet crystals and again there is little evidence of the starting particles.

Because the pellets studied corroded upon standing in the atmosphere, it is feasible that differences in the magnetic properties of the pellets arise from differing degrees of oxidation, e.g., the Na_2SiO_3 coating might inhibit reoxidation

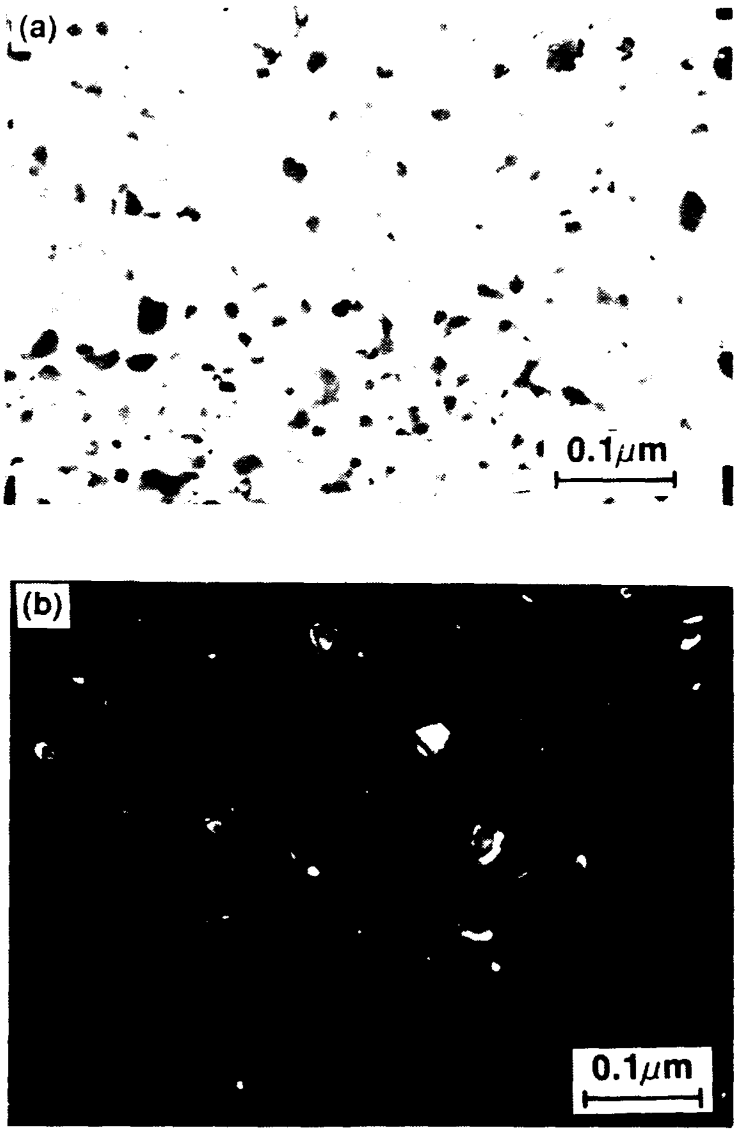

Figure 16. Transmission electron micrograph of a cross section of a thinned polymer film containing the iron particles: a) bright field and b) dark field images.

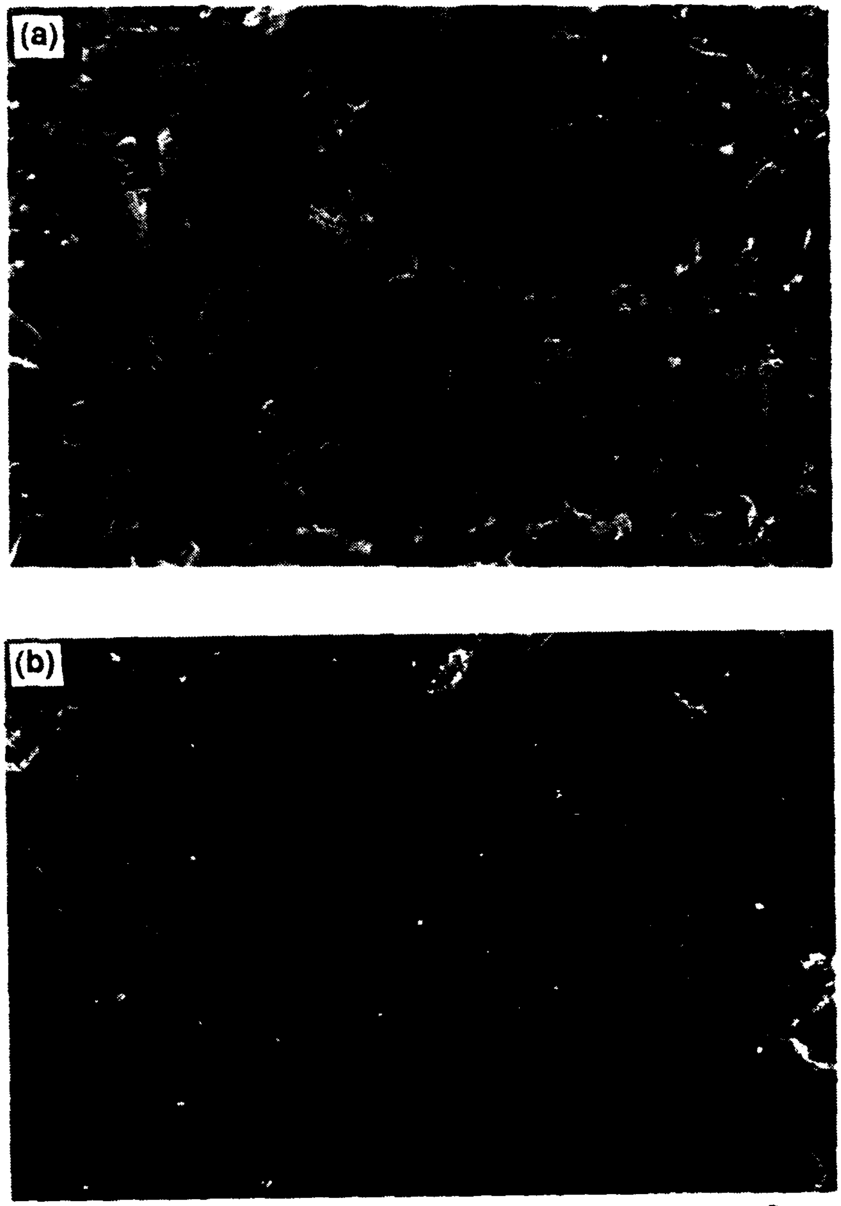

Figure 17. Scanning electron micrograph of a pellet pressed from a) uncoated and b) Na_2SiO_3-coated iron particles.

of the particles in the pellet and thus maintain the high coercivity. Scanning Auger microscopy indicated that the surfaces of the pellets were essentially iron oxides. After a four-minute sputter a pellet formed from Na_2SiO_3-coated particles had a surface consisting of ˜58 at.% Fe, ˜35 at.% O, and ˜5 at.% Cl. The comparable pellet of uncoated particles had ˜48 at.% Fe, ˜38 at.% O, and ˜10 at.% Si! The appearance of Si in an uncoated pellet is regrettable and makes the data very questionable. Unfortunately only 3 pellets of each type were studied. In none of the other five were such significant amounts of silicon detected, and moreover the appearance of the silicon is not matched by that of sodium. Chlorine, appears as a contaminant at levels ≤ 5 at.% in all of the samples, probably originates from incomplete washing of the hematite which was prepared in the presence of chloride ions. The presence of oxygen in the surface after sputtering is due to the porosity in these pellets. Whether or not the difference in Fe/O between the coated and uncoated pellets is significant is debatable. Oxygen and iron maps of the surfaces of uncoated and Na_2SiO_3-coated pellets are shown in Fig. 18; the lighter regions correspond to the greatest concentrations. The uncoated sample appears to be more heterogeneous, even allowing for the obvious effect of the porosity upon the apparent distribution of iron. The Na_2SiO_3-coated sample shows no great segregation of the two elements at the surface.

Conventional wisdom states that the Na_2SiO_3 coating enhances coercivities of the iron particles by preventing sintering and we have shown some evidence that this is indeed the case. This should only be valid for isolated particles dispersed in a matrix. The enhancement of coercivity in the pellets implies that a grain boundary phase is effectively isolating the particles from one another. It could also be true that the Na_2SiO_3 acts to prevent reoxidation and the scanning Auger microscopy data do not contradict this. Unfortunately the resolution obtained in the

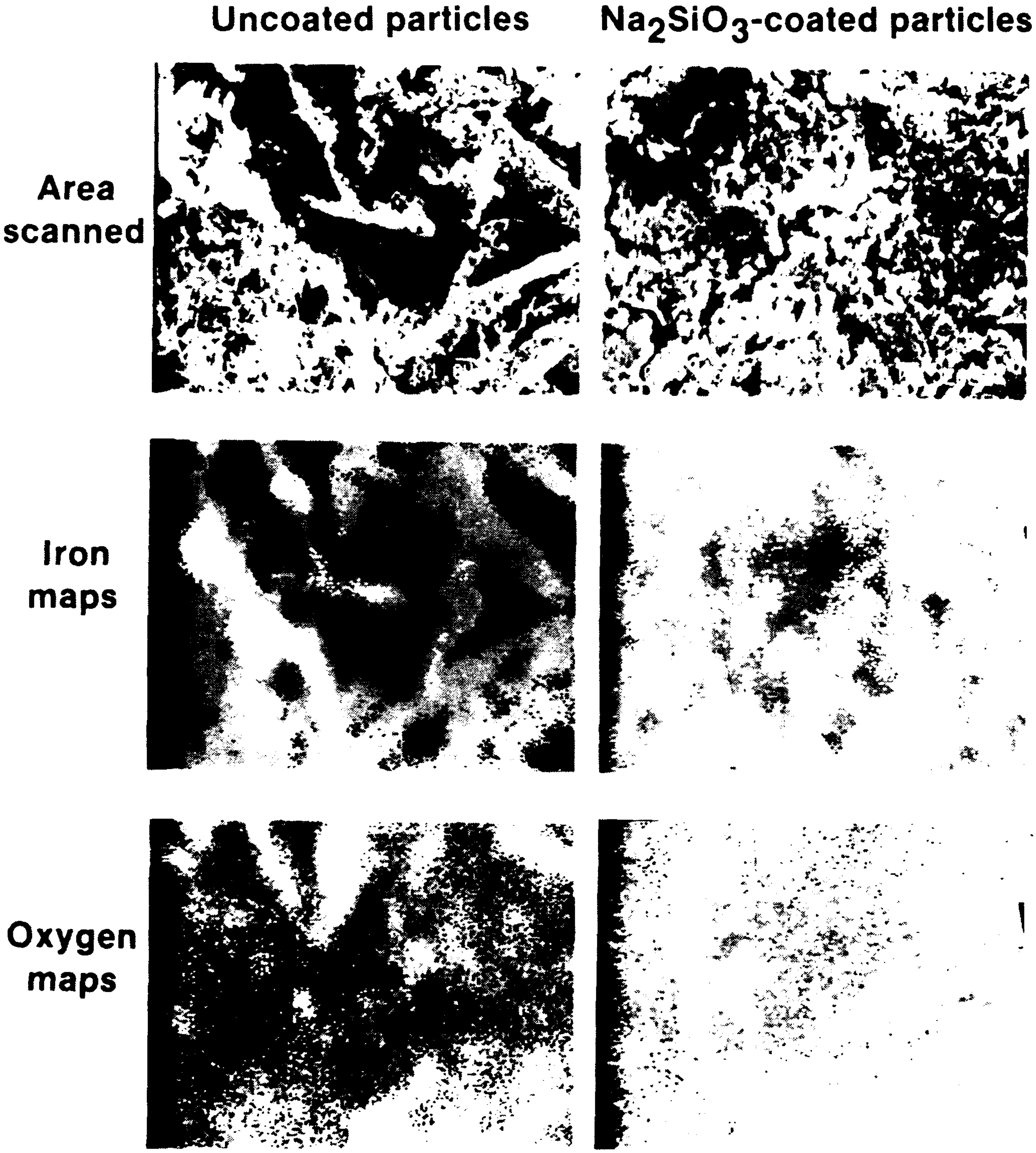

Figure 18. Iron and oxygen maps of the surfaces of pellets of uncoated and Na_2SiO_3-coated iron particles.

SEM's and the scanning Auger maps does not allow investigation of the grain boundaries between 500 Å particles. The particles themselves are barely discernible. The explanation of this phenomenon will have to await future work.

3. KINETICS OF THE REDUCTION OF SUPERFINE HEMATITE

The kinetics of the reduction of hematite to iron have been important long before the advent of magnetic recording. However, the reduction of fine hematite particles to iron takes on additional importance where recording is involved. This arises from the need to produce iron particles with good magnetization while at the same time minimize the sintering between the particles so that the coercivity can be optimized. In addition, for the process to be viable the reduction should proceed at a reasonable rate.

Van der Giessen and Klomp[21,22] studied the overall rates of reduction of acicular FeOOH. They reported that complete reduction takes about 35 minutes at 350°C and was more rapid when small amounts (1%) of cobalt or silver salts were adsorbed on the surface. The presence of these ions did not alter the coercivity of the iron particles formed at 350°C, but by increasing the reduction rate particles with higher coercivities were formed at lower temperatures. From available thermodynamic data the authors calculated that in the temperature range 25-400°C the reaction:

$$3Fe_2O_3 + H_2 = 2Fe_3O_4 + H_2O$$

is favored if $p_{H_2O}/p_{H_2} < 10^4$. The reduction of Fe_3O_4 to Fe can only take place at much lower partial pressures of H_2O. It was concluded that at high temperatures ($>350°C$) the removal of the water formed is the limiting factor, whereas at low temperatures ($<350°C$) another factor, e.g., the rate of formation of metallic nuclei, predominates. A more detailed study has been made by Rao and Moinpour[23] using sheets of Fe_2O_3 made by carefully oxidizing iron foils. They found that the reduction began with an incubation period during which the rate of reduction is small and the extent of reduction modest. The incubation period is followed by a steady-state region over which the extent of the reduction can range from as low as 20% to as high as 80%. After the steady-state period is a decay stage during which the reduction rate gradually tapers off. The incubation period was reported to correspond to the formation of iron nuclei, the steady state period to the growth of these nuclei, and the decay period to excessive overlapping of the growing nuclei. The activation energy was calculated to be 61 kJ/mole and the steady state reaction rate was 2.609×10^{-7} g.atom O/cm^2.s.atm at 356°C. The purpose of this work is to compare the reduction kinetics of the superfine particles with the literature data on films.

3.1. Method

The reduction of iron oxide to iron was monitored by means of a DuPont 951 thermogravimetric analyzer. Samples are placed in a platinum boat suspended from a quartz rod attached to a balance beam; sample masses w_0 ranged from 3 to 12 mg. The sample chamber is enclosed in a quartz tube that is placed inside a furnace. The temperature of the sample is monitored by a thermocouple close to the sample while the weight loss or gain is measured by a taut-band meter movement attached to the balance beam. The sample thermocouple was calibrated by suspending a piece of pure metal in place of the sample pan and heating under similar conditions to the melting point of the metal. The measured temperature at which the mass abruptly drops to zero is corrected (software) to the melting temperature of the metal. Indium (m.pt.=156.6°C) was used as the lower calibration point and aluminum (m.pt.=660.4°C) as the upper calibration point. Nitrogen gas is first allowed to flow over the sample while the material is heated at 10°C/min to the desired temperature. Hydrogen is then introduced into the system at 110 cm^3/min (average linear flow rate = 31.8 cm/min). Because of differences in the thermal conductivity between the two gases, the introduction of hydrogen is always observed in a thermogravimetric analysis (TGA) scan as a slight rise in temperature. The weight loss of the sample is then monitored isothermally as a function of time. Temperatures for the reductions ranged from 250 to 600 °C with reduction times of 1 to 4 h. The lower the reduction temperature, the longer the time needed for a complete reduction.

A different hydrogen flow rate of 55 cm^3/min was used to check on the effect of flow rate on the kinetics of the reaction. The rate of reduction was found to be independent of flow rate, at least over this range. The reduction rate was also found to be independent of the macroscopic geometry of the sample (e.g., there was no difference between the sample heaped in the pan and it being spread out as a relatively thin "coating."

3.2. Results

3.2.1. Uncoated particles

Figure 19 is a TGA curve of the reduction of uncoated iron oxide particles at 363°C. Essentially no weight is lost during the 15 minutes at 100°C, indicating that the oxide is dry. A small weight loss (Δw_i) that occurs on ramping up to the reduction temperature could be due to decomposition of some hydroxide species or even loss of surface oxygen. When the hydrogen is introduced, the temperature rises about 10°C (probably because of a difference in thermal conductivity between the nitrogen and hydrogen) and reduction begins. Reduction appears to be a two-step process. The first step accounts for a weight loss of 6-10%, which would indicate formation of FeO as an intermediate; the second step is the formation of the Fe. Reduction continues until no more weight is lost, at which point the total

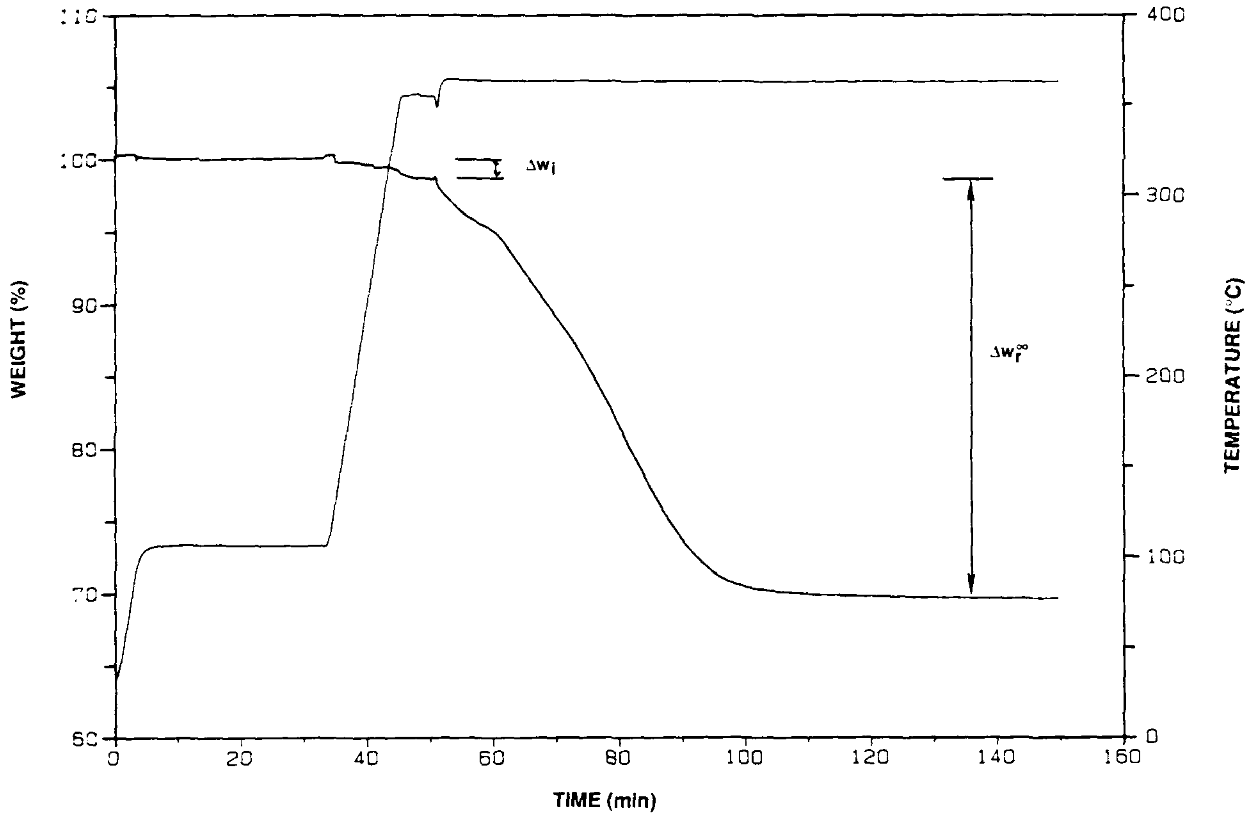

Figure 19. Thermogravimetric analysis plot of the reduction of uncoated iron oxide particles by hydrogen at 363°C.

weight loss is Δw_{tot}. The weight loss due to reduction Δw_r is taken to begin upon admission of the hydrogen. Thus the total weight loss is given by:

$$\Delta w_{tot} = \Delta w_i + \Delta w_r^{\infty} \tag{5}$$

where Δw_r^{∞} is the limiting weight loss resulting from reduction. The experimental data for the runs in pure hydrogen are summarized in Table 1, and those in which the partial pressure of hydrogen (p_{H_2}) was varied are summarized in Table 2.

Inspection of Table 1 shows that for all but the lowest temperatures studied the total weight loss is 30.7 ±0.6 %, and the total weight loss during reduction is 29.1 ±0.8 %. The theoretical weight loss of a sample is given by $\Delta w_{th} = 100 \times 48/159.7 = 30.05$ %. The mean values for both Δw_{tot} and Δw_r^{∞} thus differ from the theoretical value by more than two standard deviations. The larger than theoretical total weight loss is to be expected since weight loss occurs prior to the introduction of the hydrogen. This implies that some impurity (e.g., water from decomposition of hydroxyl) is being driven off. Even allowing for the initial weight loss as an impurity, the weight lost during reduction is too low by ~0.5 %. This is likely due to some prereduction (i.e., loss of surface oxygen) occurring before the hydrogen is introduced. The data were converted to extents of reaction α according to:

$$\alpha = \Delta w_r / \Delta w_r^{\infty} \tag{6}$$

where Δw_r is the weight loss at time t after introduction of the hydrogen. Therefore, it is possible that the α-t plots, which are shown in Figs. 20-25, should begin at 0.015 rather than 0.000.

It is seen from Figs. 20-25 that the higher the reduction temperature, the less distinguishable are the two steps. Indeed at the higher temperatures (>400°C) the data look similar to those reported by Rao and Moinpour[23]. An apparent rate

Table 1. **Experimental data for the reduction of hematite with pure hydrogen.**

Run #	Temp. (°C)	w_0 (mg)	Δw_i (%)	Δw_r^∞ (%)	Δw_{tot} (%)	t_r (min)
01	308	5.39	0.8	19.2	20.0	>350
51	325	8.31	1.7	24.8	26.5	>380
12	327	5.37	0.3	29.3	29.6	220
38	363	6.79	1.3	29.1	30.4	115
02	379	4.72	1.5	30.0	31.5	37
50	386	7.18	1.9	29.1	31.0	70
58	387	11.45	1.5	28.7	30.2	56
56	393	3.15	0.5	22.9	23.4	>116
37	414	7.30	1.8	29.2	31.0	31
57	415	3.32	1.0	29.8	30.8	38
55	428	10.29	1.8	28.9	30.7	53
10	435	7.68	1.3	29.3	30.6	26
61	446	9.99	2.0	29.0	31.0	32
59	447	11.38	2.0	28.7	30.7	21
70	452	10.84	2.3	28.3	30.6	33
33	452	7.85	1.6	29.2	30.8	39
35	458	7.74	1.8	28.9	30.7	22
60	464	9.99	1.8	28.9	30.7	28
21	478	7.46	1.5	28.8	30.3	11
20	510	9.19	1.7	28.8	30.5	15
25	525	7.80	1.8	29.0	30.8	6

Table 2. **Experimental data for the reduction of hematite with hydrogen/nitrogen mixtures.**

Run #	Temp. (°C)	p_{H_2}	w_0 (mg)	Δw_i (%)	Δw_r^∞ (%)	Δw_{tot} (%)	t_r (min)
65	416	0.05	9.18	1.6	24.4	26.0	>115
64	421	0.20	8.32	1.9	26.9	28.8	56
63	420	0.50	10.56	2.0	26.9	28.9	58
62	423	0.80	7.41	2.0	28.8	30.8	44
55	428	1.00	10.29	1.8	28.9	30.7	31

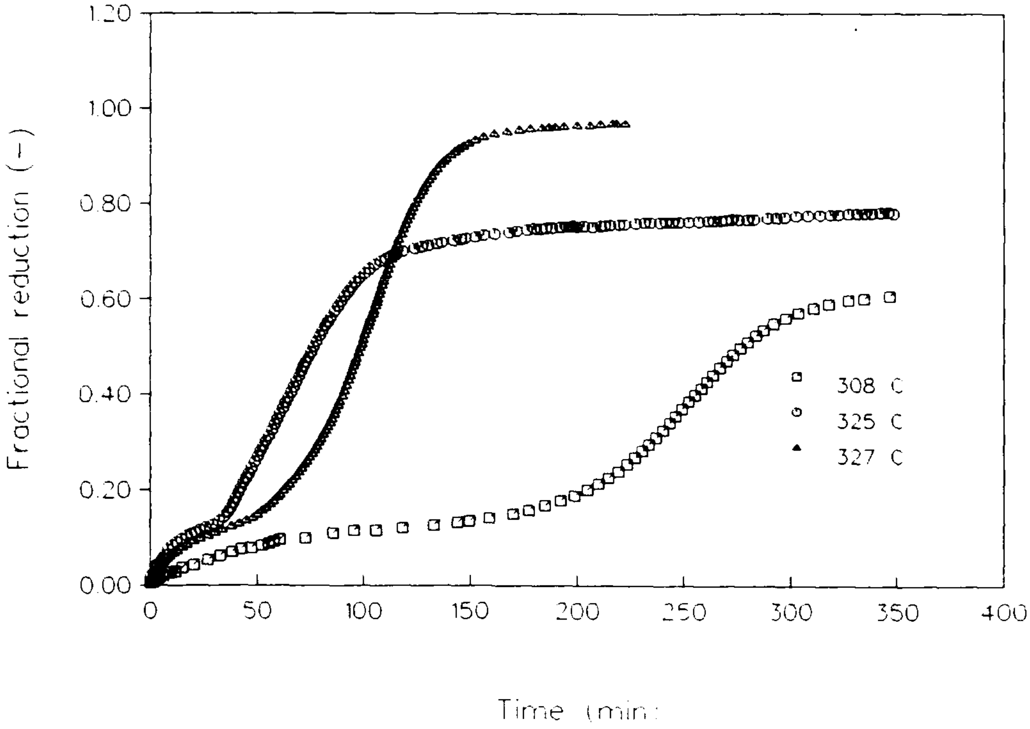

Figure 20. Reduction kinetics of uncoated iron oxide particles with pure hydrogen at 308, 325, and 327°C.

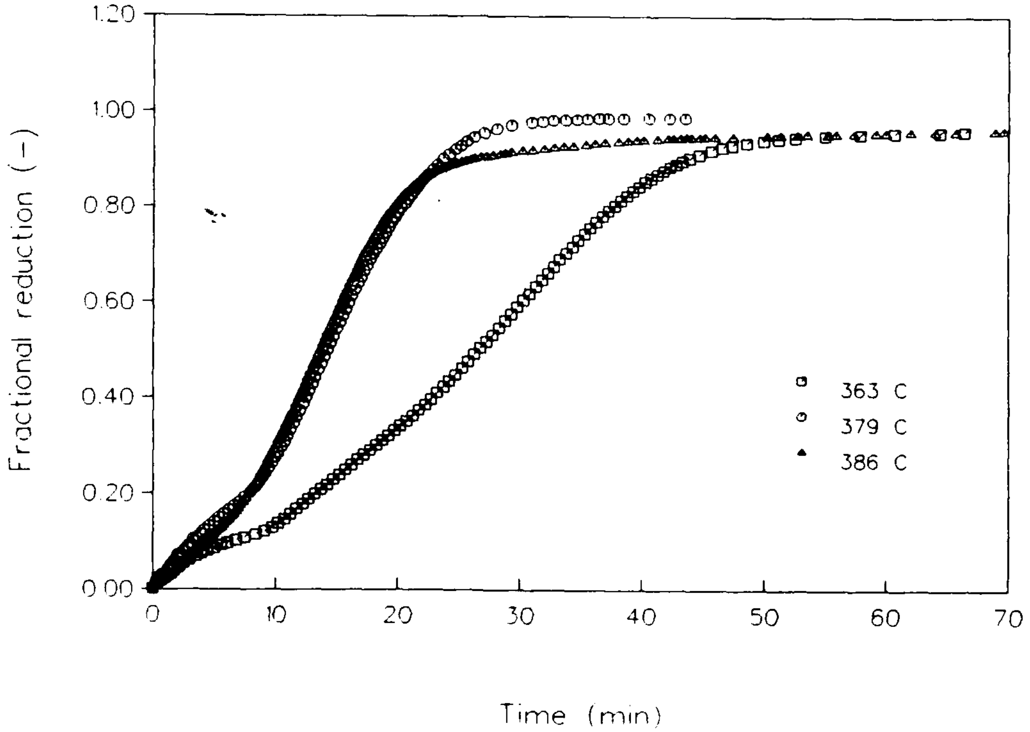

Figure 21. Reduction kinetics of uncoated iron oxide particles with pure hydrogen at 363, 379, and 386°C.

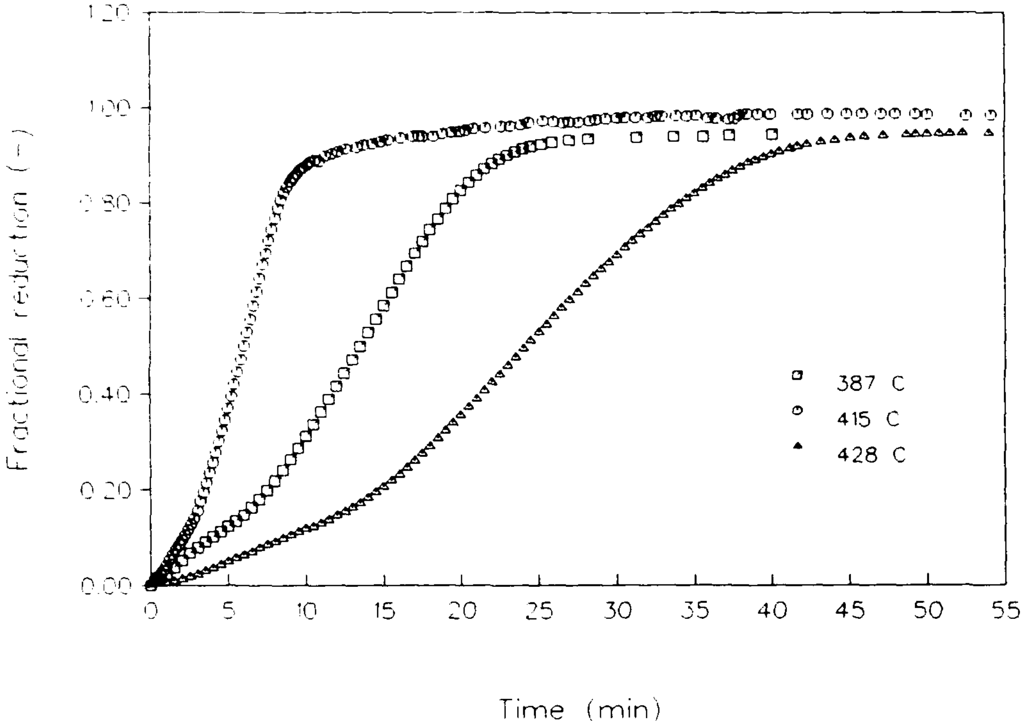

Figure 22. Reduction kinetics of uncoated iron oxide particles with pure hydrogen at 387, 415, and 428°C.

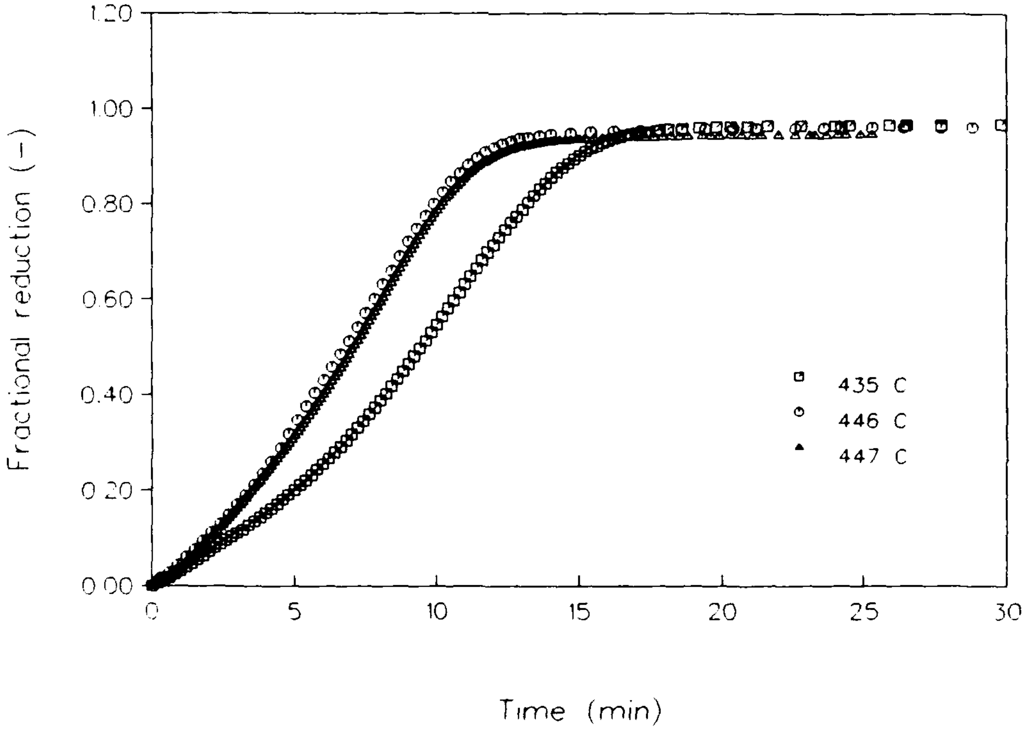

Figure 23. Reduction kinetics of uncoated iron oxide particles with pure hydrogen at 435, 446, and 447°C.

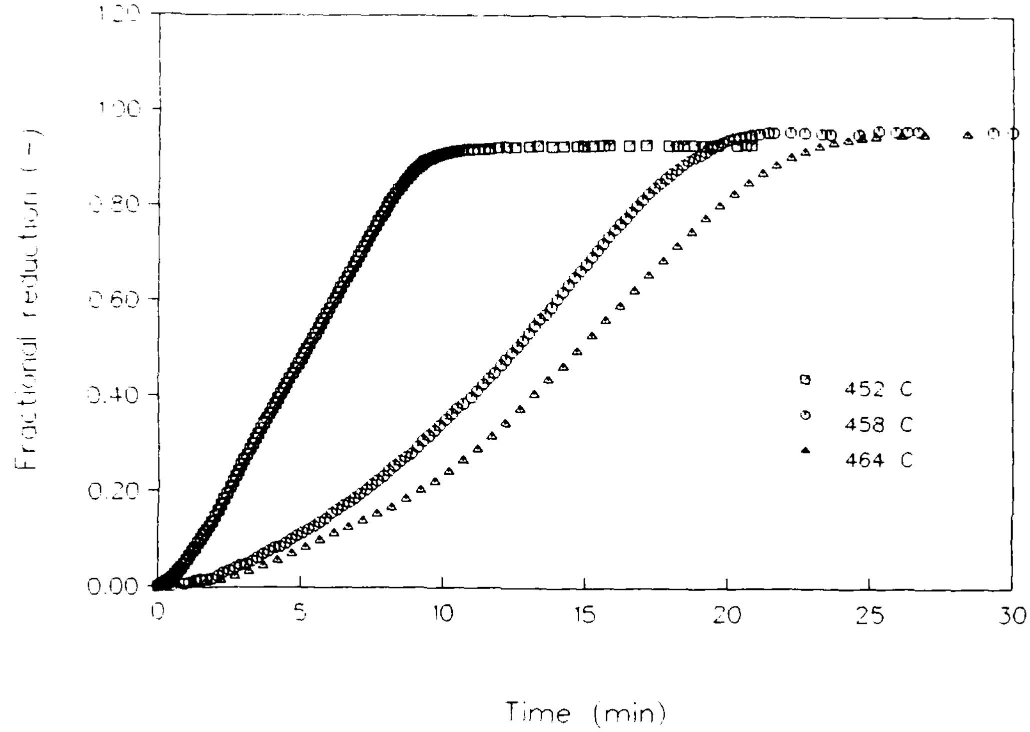

Figure 24. Reduction kinetics of uncoated iron oxide particles with pure hydrogen at 452, 458, and 464°C.

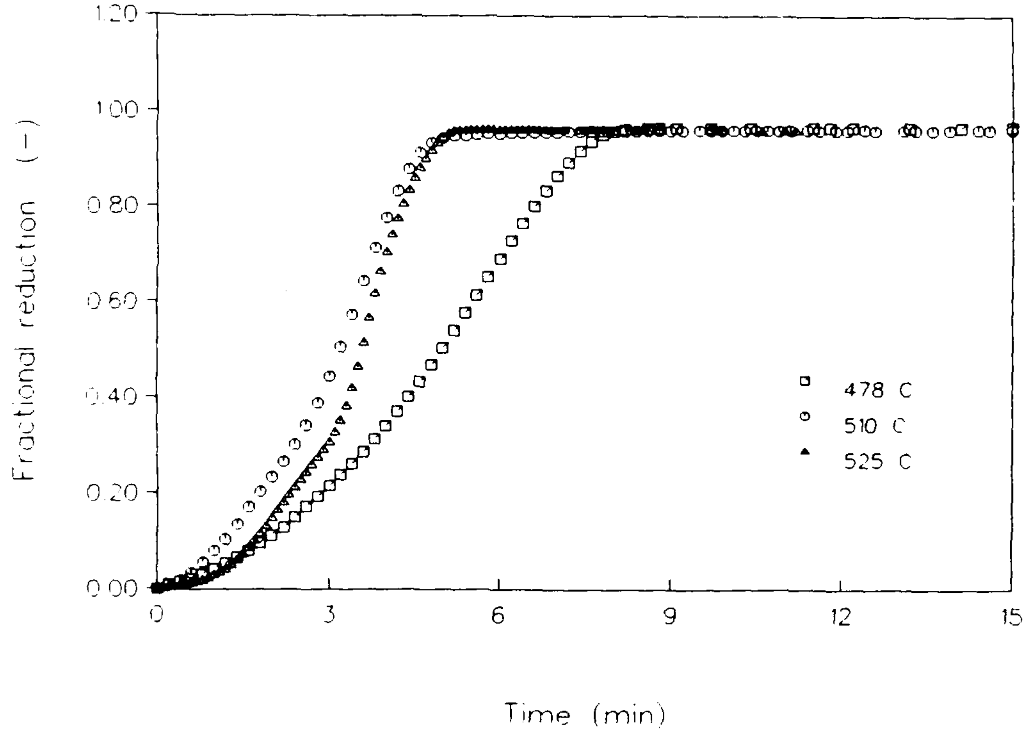

Figure 25. Reduction kinetics of uncoated iron oxide particles with pure hydrogen at 478, 510, and 525°C.

constant (k_{obs}) was obtained by measuring the slope ($d\alpha/dt$) for the middle ("steady state") period of the reaction. However, because these reductions are clearly not linear over a large extent of the reaction, the k_{obs} values do not necessarily represent a fundamental rate constant especially if the surface area of the sample is varying throughout the reduction. In order to extract fundamental rate constants from these data the rate plots need to be described using a model based of fundamental constants. The presence of the apparent two-step process meant that the data could not be analyzed by a simple method. Several were tested and these are described in the data analysis section below.

3.2.2. Sodium silicate-coated particles

The shapes of the TGA curves for the Na_2SiO_3-coated particles were similar to those of the uncoated. Table 3 shows experimental parameters obtained from these curves. The average total weight loss is 27.4 wt.% indicating that the coating accounts for approximately 11% of the total weight of the particles. It is also apparent that the reduction takes longer than for the uncoated particles shown in Table 1. The fractional reduction curves were calculated from Eq. 6 and these are shown in Figs. 26-29.

3.3. Data Analysis

An analysis was attempted using the variable heating rate method popularized by Flynn and Hall[24]. For this method the reaction is recorded at several heating (β) rates between 1 and 20°C/min. A constant degree of reaction is selected and the corresponding temperature (T) determined for each reaction profile. The measured values of temperature and heating rate are then used to compute (E_{act}) activation energy from:

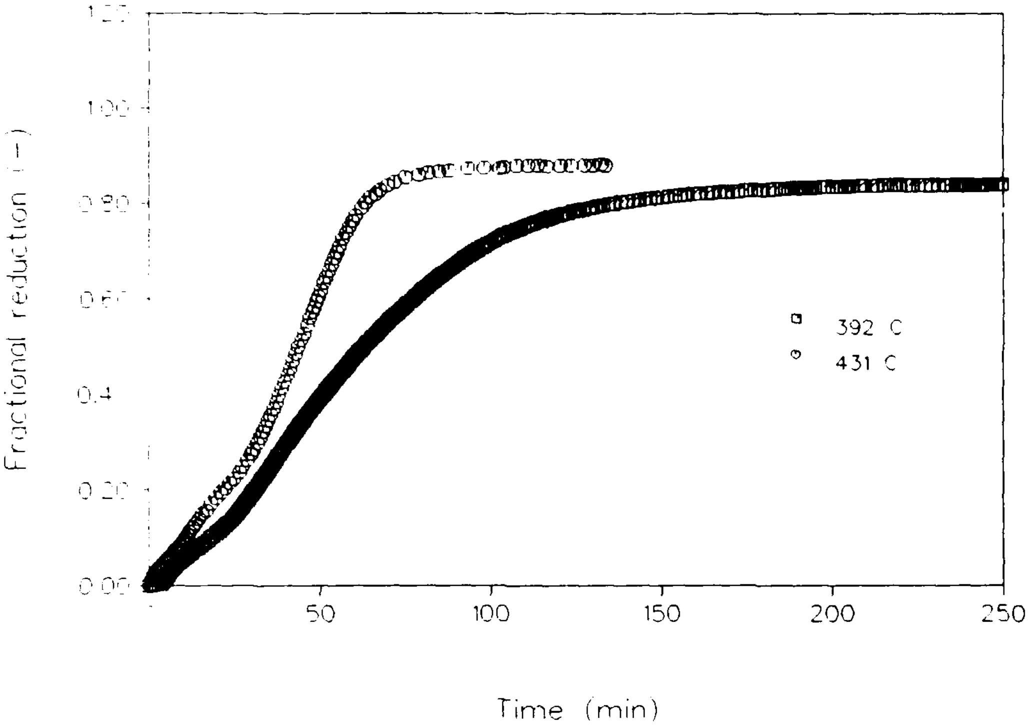

Figure 26. Reduction kinetics of Na_2SiO_3-coated iron oxide particles with pure hydrogen at 392 and 431°C.

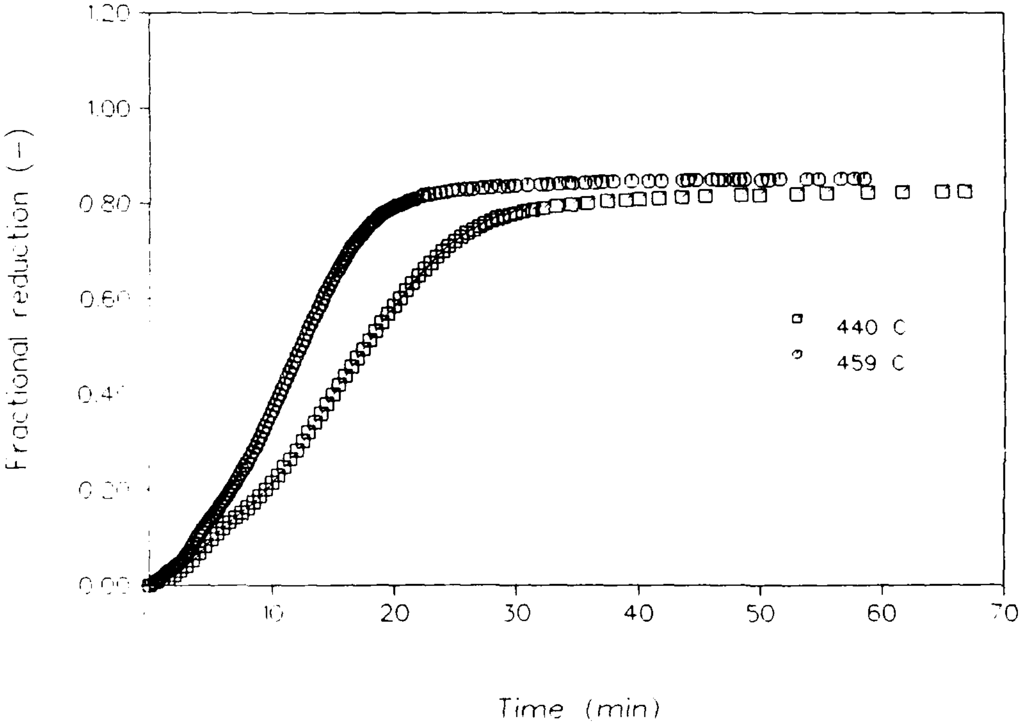

Figure 27. Reduction kinetics of Na_2SiO_3-coated iron oxide particles with pure hydrogen at 440 and 459°C.

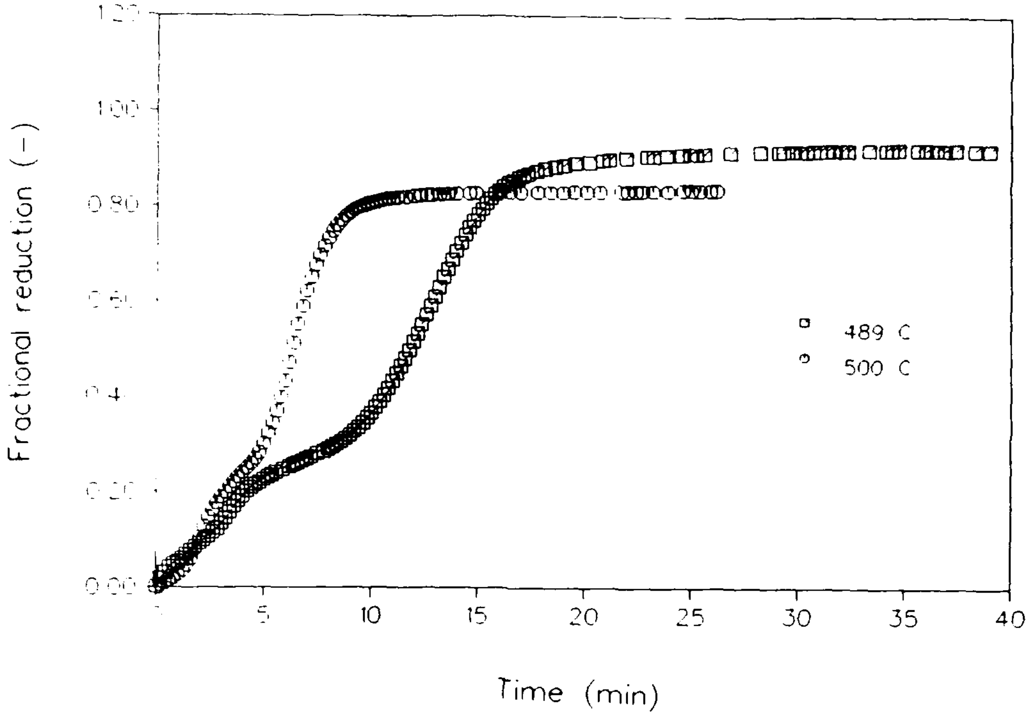

Figure 28. Reduction kinetics of Na_2SiO_3-coated iron oxide particles with pure hydrogen at 489 and 500°C.

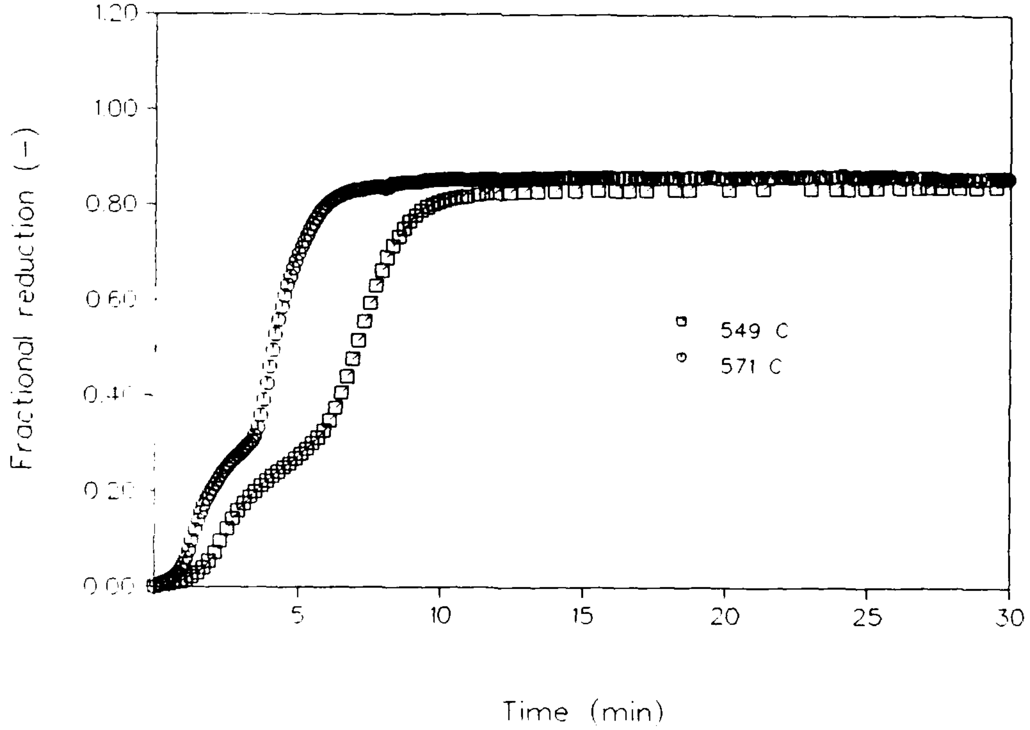

Figure 29. Reduction kinetics of Na_2SiO_3-coated iron oxide particles with pure hydrogen at 549 and 571°C.

Table 3. **Experimental data for the reduction of Na_2SiO_3-coated hematite with pure hydrogen.**

Run #	Temp. (°C)	w_0 (mg)	Δw_i (%)	Δw_r^∞ (%)	Δw_{tot} (%)	t_r (min)
36C	392	9.93	1.2	25.2	26.4	207
11C	431	3.99	1.0	26.5	27.5	109
27C	440	12.86	2.2	24.8	27.0	60
34C	459	8.64	2.1	25.6	27.7	51
01C	489	3.85	0.5	27.8	28.3	30
29C	500	13.45	2.4	25.1	27.6	23
32C	549	8.50	1.9	25.3	27.2	18
25C	571	9.99	1.5	25.9	27.4	13

$$E_{act} = -\frac{R}{b}\frac{d\ln\beta}{d(1/T)} \tag{7}$$

where R is the gas constant and b is an empirical constant whose value depends upon E_{act}. This analysis should yield parallel, linear plots of $\ln\beta$ vs $1/T$ for different extents of reaction. The data for this reaction which were analyzed by J. Flynn of DuPont Instruments did not give parallel, linear plots.

The isothermal data were subsequently analyzed using a travelling reaction interface approach as discussed by McKewan[25,26] and Lu[27]. The analysis was modified to allow for a two-step process and this is shown schematically in Fig. 30 for a spherical sample. The solid reactant (Fe_2O_3, phase 0) sphere has an initial radius r_0. As reaction proceeds the intermediate product (1), which may be Fe_3O_4, forms and the radius (r_1) of the unreacted core shrinks. Once sufficient intermediate product forms, reaction to the final product (2), in this case Fe, commences and the radius (r_2), which encompasses the unreacted core plus intermediate product, shrinks too. Three zones are thus defined: unreacted Fe_2O_3 ($0 \leq r \leq r_1$),

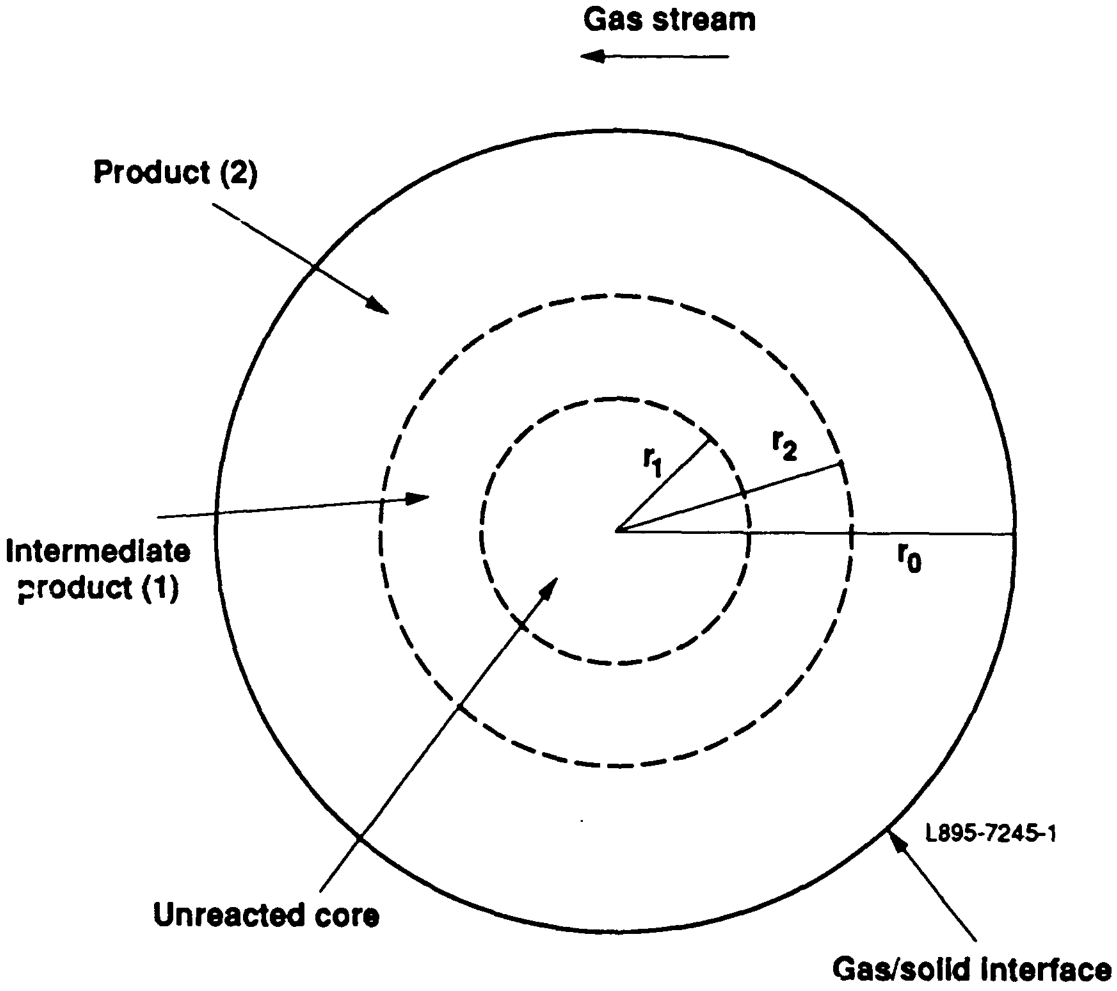

Figure 30. Schematic diagram of a gas-solid reaction for a spherical sample.

intermediate product ($r_1 \le r \le r_2$), and Fe ($r_2 \le r \le r_0$). At any point in time the iron is distributed among phases 0, 1, and 2. The mole fractions of the total iron in each phase are defined as χ_0, χ_1, and χ_2, so that $\chi_0 + \chi_1 + \chi_2 = 1$.

The general form of the gas-solid reaction is given by:

$$\frac{dn}{dt} = k_s C_s C_\gamma A \tag{8}$$

where n is the number of moles of solid reacted, and C_s and C_γ are the concentrations of solid and gas at the reaction surface. The concentration of a pure solid is constant and if the reaction is surface-area controlled (i.e., diffusion can be neglected) then:

$$\frac{dn}{dt} = k p_{\mathrm{H}_2} A \tag{9a}$$

or

$$\frac{d\alpha}{dt} = \frac{d(n/n_0)}{dt} = k p_{\mathrm{H}_2} A \frac{\bar{v}_m}{V_0} \tag{9b}$$

where p_{H_2} is the partial pressure of hydrogen in the flowing gas stream, $\bar{v}_m$ is the molar volume of the oxide, V_0 is the volume of oxide being reduced, and the rate constant k contains the product of true rate constant, the density of surface sites, and an adsorption constant for the hydrogen. Since

$$n = \frac{4}{3}\pi(r_0^3 - r^3)\frac{1}{\bar{v}_m} \tag{10}$$

then

$$-\frac{dr}{dt} = k p_{\mathrm{H}_2} \bar{v}_m \tag{11}$$

which can be integrated to give

$$r = r_0 - k p_{\mathrm{H}_2} \bar{v}_m t. \tag{12}$$

Equations 11 and 12 are the starting points for the analysis conducted in this work. From these equations other variables are readily derivable. For example, the fractional reduction α defined as the weight (or number of moles) of oxygen removed divided by the total amount of oxygen originally present in the oxide is related to r by

$$\alpha = 1 - \frac{r^3}{r_0^3} \tag{13}$$

and substituting into Eq. 12 noting that $\tilde{v}_m = M/\rho$, where M and ρ are the molar mass and density of the oxide, gives

$$r_0\rho[1-(1-\alpha)^{\frac{1}{3}}] = kMp_{H_2}t \tag{14}$$

which is the equation derived and tested by McKewan[25,26]. The weight lost from the sample is given by $\Delta w = \alpha\phi_O w_0$ where ϕ_O is the mass fraction of oxygen removable from the oxide and w_0 is the initial weight of the oxide.

Analysis of the two-step process depicted in Fig. 30 involves calculation of the mole fractions χ_1 and χ_2 of phases (1) and (2). The extent of reaction is then given by

$$\alpha = \chi_2 + \frac{\phi_{O1}}{\phi_O}\chi_1 \tag{15}$$

where ϕ_{O1} is the mass fraction of oxygen removed from the original oxide to form phase (1). The mole fractions can be expressed in terms of r_1 and r_2

$$\chi_2 = 1 - \frac{r_2^3}{r_0^3} \tag{16}$$

and

$$\chi_1 = \frac{1}{r_0^3}(r_2^3 - r_1^3). \tag{17}$$

In the first instance, both reaction rates were assumed to be surface area controlled so that:

$$\frac{r_1}{r_0} = 1 - \frac{k_1}{r_0} p_{\mathrm{H}_2} t \tag{18}$$

and

$$\frac{r_2}{r_0} = 1 - \frac{k_2}{r_0} p_{\mathrm{H}_2} t \tag{19}$$

where the rate constants k_1 and k_2 include the material constants such as $\bar{v}_m$. For a given $k_1 p_{\mathrm{H}_2}/r_0$ and $k_2 p_{\mathrm{H}_2}/r_0$, the dimensionless values r_1/r_0 and r_2/r_0 are calculated within the limitations $0 \leq r_1/r_0 \leq 1$, $0 \leq r_2/r_0 \leq 1$, and $r_1 - r_2 > \delta r_0$ for $r_1 > 0$ where δr_0 is an "incubation" parameter representing a delay between the formation of phase 1 and the beginning of reaction to form phase 2. The parameters $k_1 p_{\mathrm{H}_2}/r_0$, $k_2 p_{\mathrm{H}_2}/r_0$, and t_0, which allows for uncertainty in the exact start of the reaction, were adjusted using a multiparametric curve-fitting program. The "incubation" parameter δr_0 was varied but only within the limits of a few atomic layers. This analysis will be referred to as CASE 1.

An alternative analysis ret. ins the travelling reaction front associated with conversion to phase 1, but considers the region of phase 1 to be so porous that the gas has access to the entire region. The concept of the second travelling front and, of course, r_2, thus disappears. The rate equation for region 1 is now given by:

$$-\frac{dn_1}{dt} = k_2 p_{\mathrm{H}_2} n_1 \tag{20}$$

or, dividing both sides by $\frac{4}{3} \frac{\pi r_0^3}{\bar{v}_m}$ to express the quantity of intermediate as a mole fraction of the total iron,

$$-\frac{d\chi_1}{dt} = k_2 p_{\mathrm{H}_2} \chi_1. \tag{21}$$

Calculation of χ_1 involves treating region 1 (cf Fig. 30) as a series of shells at radius r with thickness dr, where $r_1 \leq r \leq r_0$. For each individual shell the first order conversion of intermediate (1) to final product begins at some time t_β after the start of the reduction where $t_\beta = (r_0 - r)/k_1$. The first order conversion for a given shell can therefore be written:

$$\chi_{1r} = \chi_{1r0} e^{-k_2'(t-t_\beta)} \tag{22}$$

where χ_{1r} and χ_{1r0} are the mole fractions of iron existing as (1) in the shell of radius r at times $t(>t_\beta)$ and t_β, respectively and $k_2' = k_2 p_{H_2}$. The initial quantity χ_{1r0} is given geometrically by

$$\chi_{1r0} = \frac{4\pi r^2 dr}{\frac{4}{3}\pi r_0^3}. \tag{23}$$

The value for χ_1 at any time can be obtained by integrating χ_{1r} between r_0 and r_1:

$$\chi_1 = \frac{3}{r_0^3} \int r^2 e^{-k_2'[t-(r_0-r)/k_1]} dr \tag{24}$$

which yields

$$\chi_1 = \frac{6}{{r_0}^{*3}} \left[(1 + r_0{}^* + \frac{{r_0}^{*2}}{2})(1 - e^{-k_2't}) - k_2't(1 + r_0{}^*) + \frac{1}{2}k_2'^2 t^2 \right] \tag{25}$$

for $t \leq r_0/k_1$ and

$$\chi_1 = \frac{6}{{r_0}^{*3}} \left[e^{r_0^*} - (1 + r_0{}^* + \frac{{r_0}^{*2}}{2}) \right] e^{-k_2't} \tag{26}$$

for $t > r_0/k_1 p_{H_2}$, and where $r_0{}^* = r_0 k_2/k_1$. Values for α can be calculated from Eq. 15 remembering that $\chi_0 + \chi_1 + \chi_2 = 1$ and $\chi_0 = (r1/r_0)^3$. The rate constant k_1 is as defined in CASE 1 and the first order rate constant k_2 is defined in Eq. 20. The incubation term defined in CASE 1 is not used. The data were fitted using the parameters r_0^*, k_2', and t_0. This will be referred to as CASE 2.

3.4. Discussion

In Figs. 31 and 32 the data from run #02 with the "best fits" obtained from CASE 1 and CASE 2 can be compared. It is apparent that CASE 2 (Fig. 32) gives the worse agreement between model and data from which it can be inferred that even the latter portions of the reduction do not follow an exponential law. Although better than CASE 2, CASE 1 (Fig. 31) also does not give a satisfactory fit. These observations were common throughout the various data sets. That the rate data do not follow an exponential law is quite reasonable, because gas-solid reactions generally have been found to depend upon interfacial area, or diffusion, rather than on the amount of solid present. Indeed the data of Rao and Moinpour show linear behavior over a wide range of α for the reduction of Fe_2O_3 films where interfacial area was taken to be constant. The travelling reaction-front model, which was developed for pellets, allows for curvature in the data because the interfacial area decreases as the reaction proceeds. The modification (CASE 1) of this model proposed herein, however, does not adequately describe the peculiarities seen in the current data.

Examination of the values extracted for the kinetic parameters also indicates the erroneous nature of CASE 1. Table 4 shows values for k_{obs} and for k_1 and k_2 obtained from CASE 1. It is apparent that k_1 and k_2 have remarkably similar values. What is not shown in Table 4 but was found also during the analysis is that if values for t_0 or α at completion are varied slightly then k_2 can change by an order of magnitude, which implies that the data are not very sensitive to k_2. This is preposterous since the step containing k_2 (i.e., $Fe_3O_4 \rightarrow Fe$) has been found in

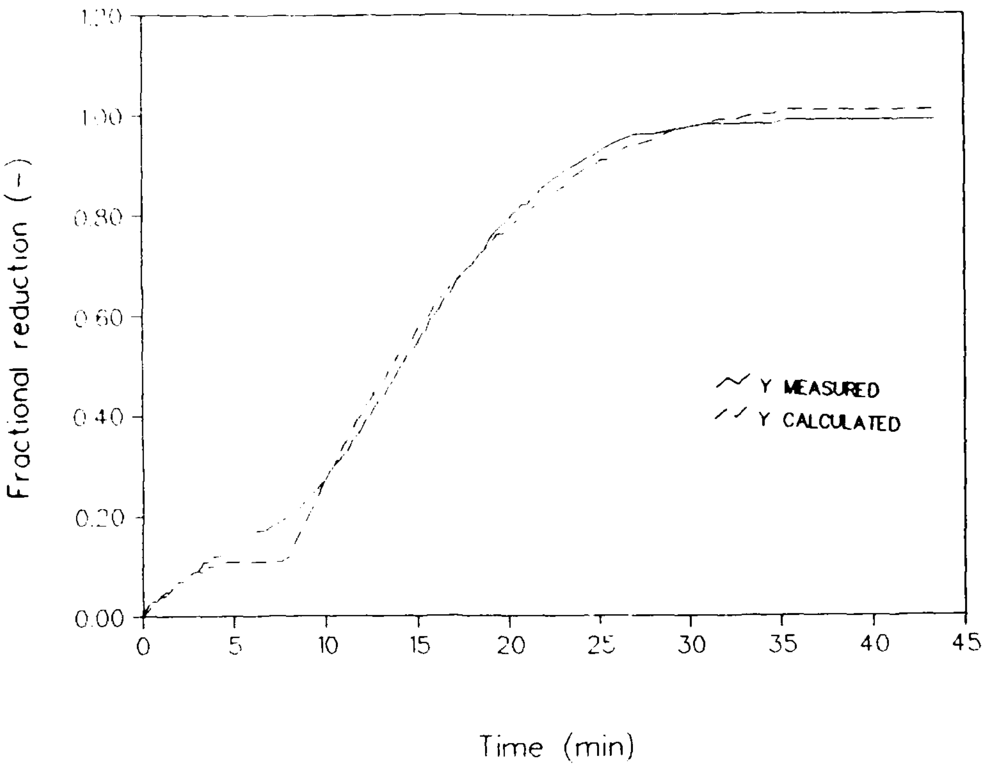

Figure 31. Best fit to kinetic data from run #02 using CASE 1.

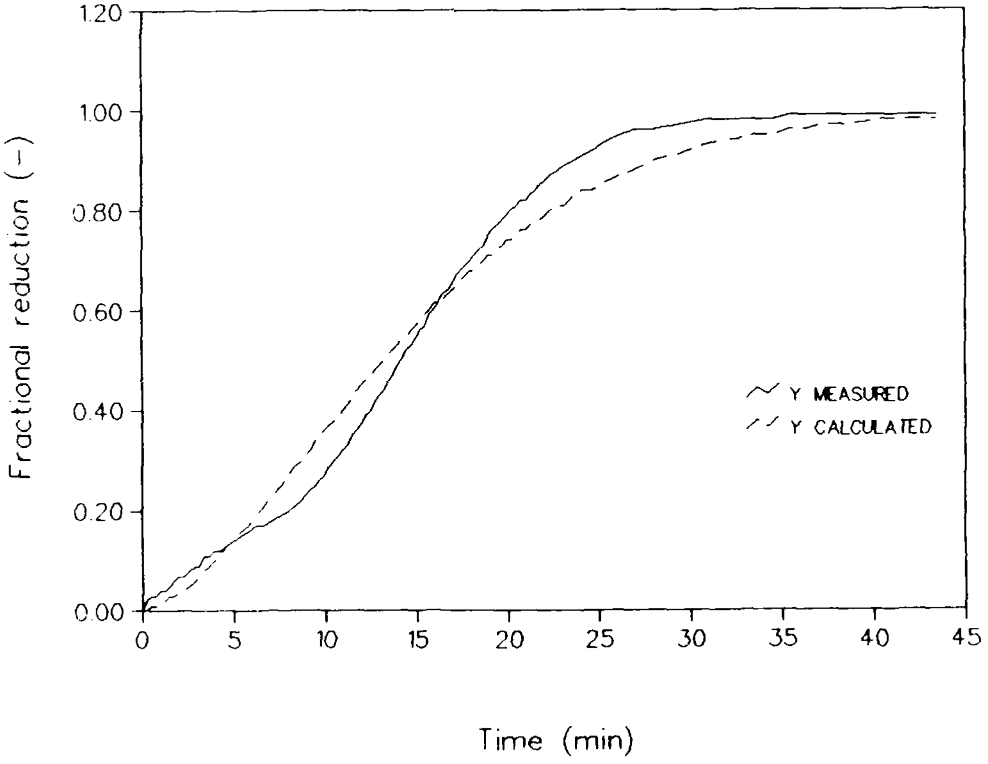

Figure 32. Best fit to kinetic data from run #02 using CASE 2.

previous work[21,22] to be the rate determining step. Therefore, we are forced to conclude that our treatment of the initial stage of the reaction was incorrect. It appears that there is only one rate process involved and that the initial stages of reaction must be rationalized in terms of diffusion or an equilibrium reaction.

Table 4. Kinetic parameters for the reduction of hematite with pure hydrogen.

Run #	Temp. (°C)	$k_{obs} \times 10^3$ (s^{-1})	$k_1 \times 10^3$ (s^{-1})	$k_2 \times 10^3$ (s^{-1})	$\bar{k}_s \times 10^6$ (g atom O m^{-2} s^{-1} atm^{-1})
01	308	0.0798	0.0605	0.0728	0.037
51	325	0.146	0.119	0.106	0.069
12	327	0.212	0.130	0.147	0.100
38	363	0.465	0.325	0.325	0.218
02	379	0.939	0.568	0.568	0.441
50	386	0.963	0.548	0.533	0.452
58	387	0.915			0.430
57	415	2.23			1.047
55	428	0.578			0.271
10	435	1.32	0.995	0.995	0.620
61	446	1.58			0.742
59	447	1.65			0.775
70	452	1.79			0.840
35	458	1.17	0.683	0.867	0.549
60	464	1.07			0.502
21	478	3.12	0.603		1.465
20	510	5.57	0.938	0.938	2.615
25	525	8.30			3.897

Figure 33 is an *Arrhenius* plot of the values for k_{obs}. One striking feature of the plot is the discontinuity that occurs around 420-450°C where k_{obs} apparently drops dramatically. Above and below this region the data give linear plots with an activation energy of 99 ±5 kJ/mole/. One possible explanation for this drop is that values of k_{obs} contain the surface area. It has been previously shown (Fig. 7)

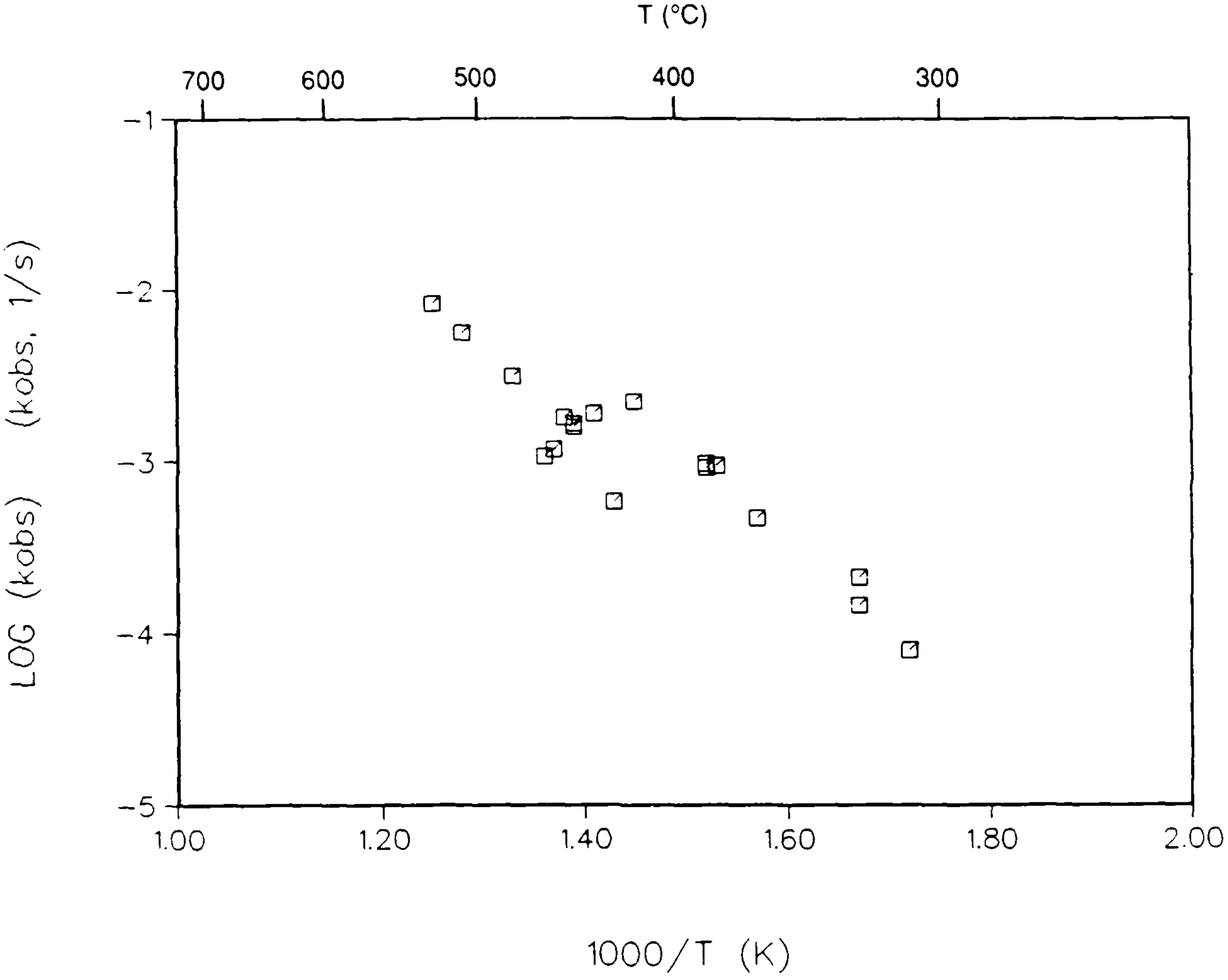

Figure 33. Arrhenius plot of apparent rate constants (k_{obs}) for the reduction of uncoated hematite by pure hydrogen.

that the surface area of these superfine particles goes through a maximum as the temperature is increased, with the maximum occuring around 400°C. The decrease in surface area with increasing temperature is associated with sintering of the particles. It is therefore likely that the interfacial reaction area is decreasing as the temperature is raised above 400°C and that this causes a decrease in k_{obs}.

The literature contains much data on the reduction of films or large pellets of Fe_2O_3 and it would be instructive to compare this literature data with the results obtained for superfine particles herein. The parameter required to convert the k values in Table 4 to useful values for comparison is the surface area of the particles. In the absence of a successful model to describe the kinetic behavior the values of k_{obs} will be used together with the maximum surface area measured by BET (see Fig. 7). The comparable (fundamental) rate constant is then given by

$$\bar{k}_s = k_{obs} \frac{\Delta w_{th}}{\Sigma} \frac{1}{1600} (\text{g·atom O·m}^{-2}\cdot\text{s}^{-1}\cdot\text{atm}^{-1}) \qquad (27)$$

where the specific surface area Σ is taken to be 40 m^2/g. Various values from the literature correlated by Rao and Moinpour[23] can be compared with the values for $\bar{k}_s$ obtained here in Fig. 34. It is seen that the data here are similar to those obtained for 10-μm particles using a fluidized-bed technique,[28] but are much lower than the values obtained from reduction of thick films. Given the failure to accurately describe the individual rate plots using a simple model, it is likely that the data reported herein are influenced by diffusion and this may be the cause of the low values. However, it is also possible that the use of the external area in the film work is incorrect and that the interfacial reaction area in the earlier work was really much larger due to porosity.

The above discussion referred to the reduction of hematite with pure hydrogen ($\rho_{H_2}=1$). In calculating $\bar{k}_s$ it was implicitly assumed that the rates of

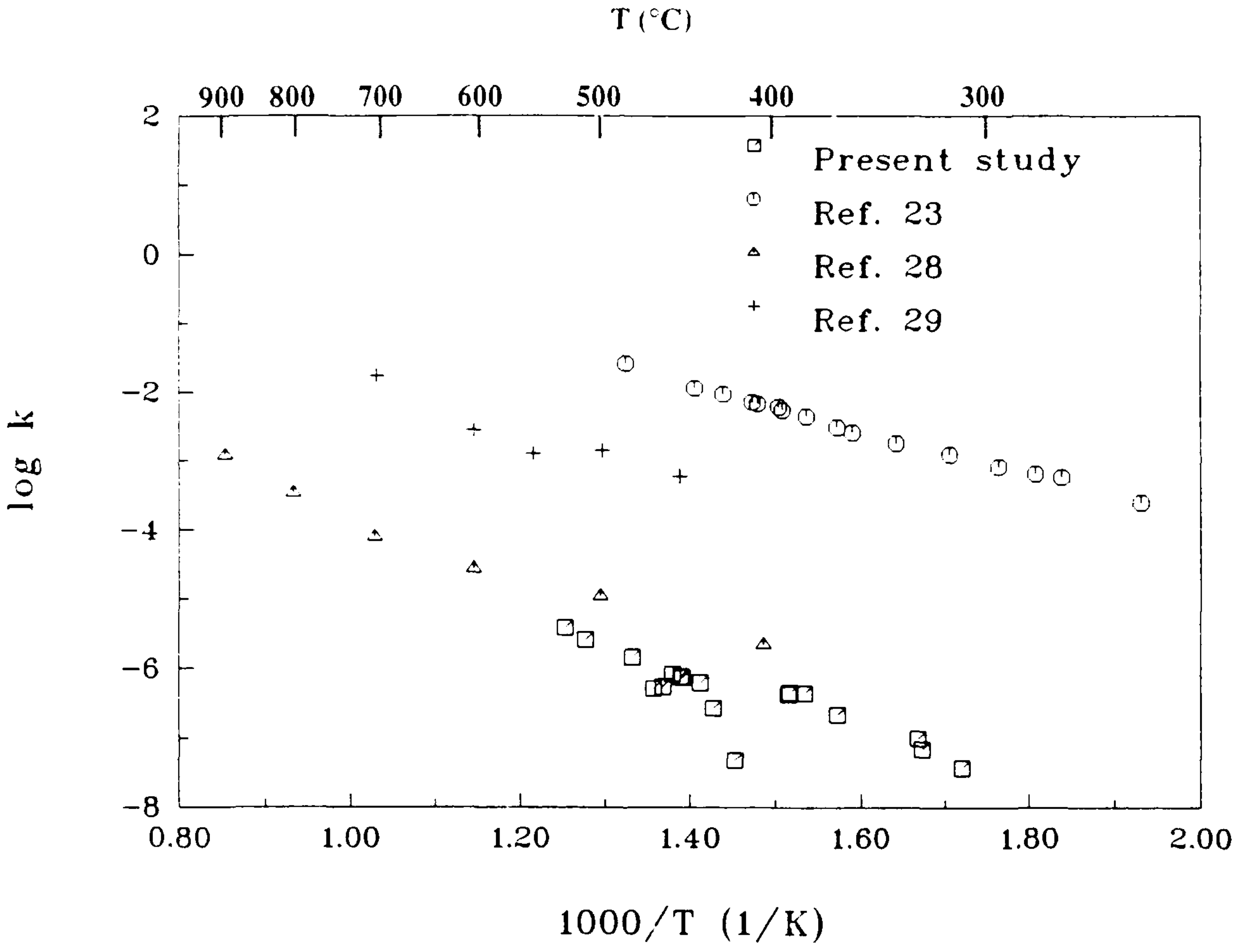

Figure 34. Comparison of the rate constant (k_s) data from the present study with those of other investigators.

reduction are directly proportional to p_{H_2}. Although this assumption appears reasonable it is still worthwhile to verify it. Table 5 and Fig. 35 show the variation of k_{obs} with p_{H_2}. It is unfortunate that the temperature chosen for this experiment corresponds to the region where there is a discontinuity and scatter in the Arrhenius plot for pure hydrogen, since this introduces considerable uncertainty into the data. Nevertheless, it appears that k_{obs} does indeed increase monotonically with p_{H_2}. The regression line shown in Fig. 35 has a slope of 1 but cannot be extrapolated to low p_{H_2} because it does not go through the origin. At low p_{H_2} an equilibrium must dominate since inspection of Table 2 shows that the reactions did not go to completion.

Table 5. Kinetic parameters for the reduction of hematite with hydrogen/nitrogen mixtures.

Run #	Temp. (°C)	p_{H_2}	$k_{obs} \times 10^3$ (s^{-1})
65	416	0.05	0.370
64	421	0.20	0.791
63	420	0.50	1.07
62	423	0.80	1.40
55	428	1.00	0.578
57	415	1.00	2.23

Table 6 shows the kinetic parameters obtained for the Na_2SiO_3-coated hematite particles. It is apparent both from the values of k_{obs} and also the approximate reduction times t_r shown in Tables 1 and 3 that the Na_2SiO_3 coating retards the reduction of hematite. Based on the arguments of Van der Giessen[21,22] this would

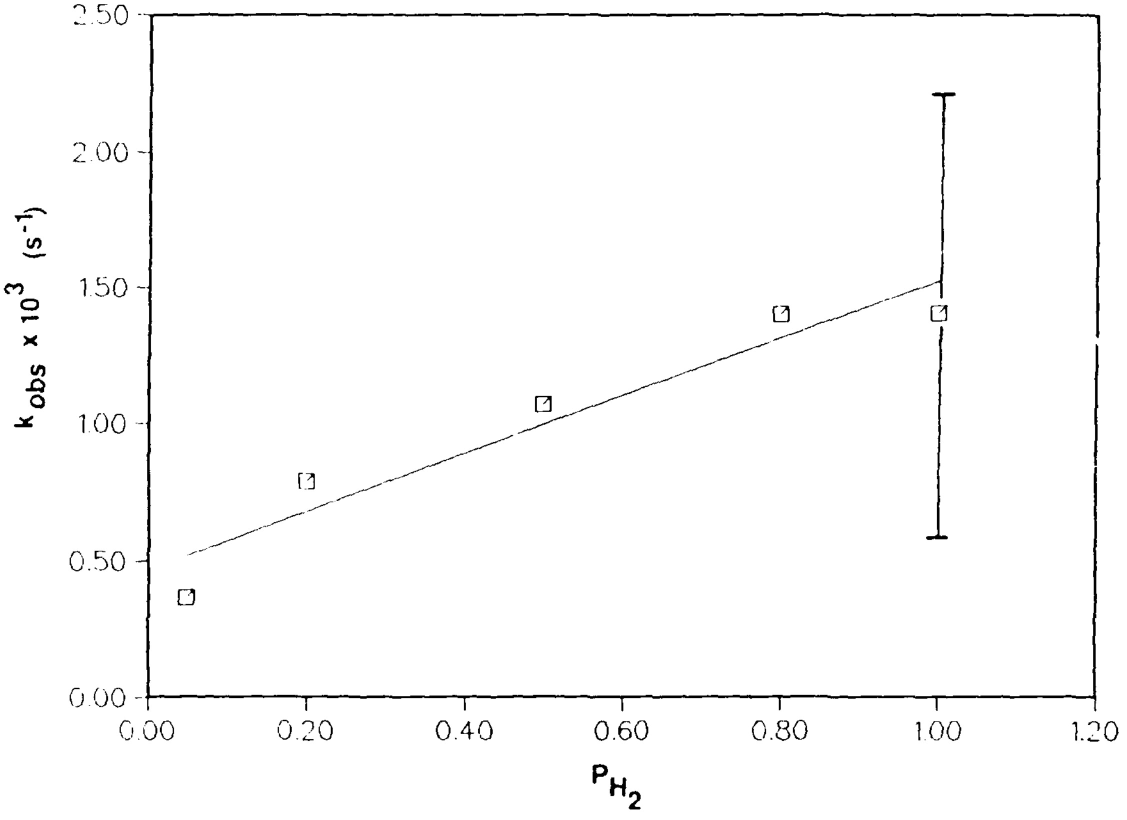

Figure 35. Variation of the rate constant (k_{obs}) with p_{H_2}.

not seem to make sense since the coating has been shown to enhance the coercivities of the iron particles formed. However, referring back to Fig. 14 it is noted that the peak coercivity of the uncoated iron particles, which occurs after reduction at 400°C, is greater than that of the coated particles. The coated particles have the preferred performance because of the indepence of H_c on reduction temperature.

Table 6. Kinetic parameters for the reduction of Na_2SiO_3-coated hematite with pure hydrogen.

Run ≠	Temp. (°C)	$k_{obs} \times 10^3$ (s^{-1})	$k_1 \times 10^3$ (s^{-1})	$k_2 \times 10^3$ (s^{-1})	$k_s \times 10^6$ (g atom O m^{-2} s^{-1} atm^{-1})
36C	392	0.160	0.098	0.095	0.075
11C	431	0.302	0.277	0.313	0.142
27C	440	0.630	0.475	0.475	0.296
34C	459	0.944	0.707	0.705	0.443
01C	489	1.60	1.135	1.297	0.751
29C	500	3.03	1.178	1.178	1.423
32C	549	3.16	1.950	2.367	1.484
25C	571	3.78	1.557	1.967	1.775

Figure 36 shows an Arrhenius plot for the reduction of the Na_2SiO_3-coated particles. The plot does not show the discontinuity seen in the plot for the uncoated hematite. The uncoated hematite particles had a discontinuity around 420°C, and referring back to Fig. 14 reveals that above this reduction temperature the coercivities of the iron particles dropped. The discontinuity in the Arrhenius plot and the decrease in H_c with temperature are the result of sintering of the uncoated iron particles. The Na_2SiO_3 coating provides a barrier to sintering and therefore shows neither the discontinuity nor the decrease in H_c. Above 500°C the plot has a lower slope indicating a transition in reaction rate control as discussed by Rao and

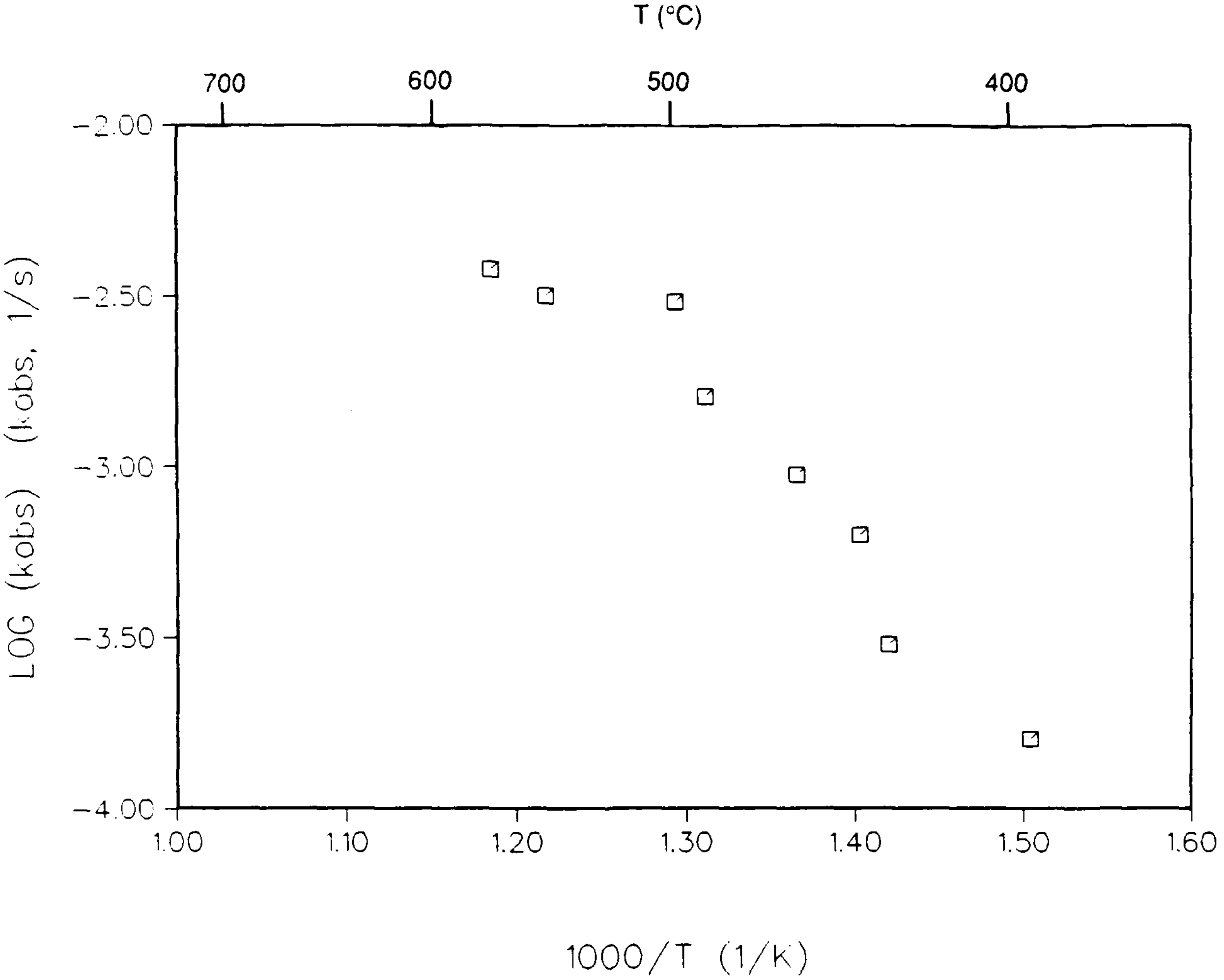

Figure 36. Arrhenius plot for the reduction of Na_2SiO_3-coated hematite particles.

Moinpour[23]. According to their description, above 500°C pore diffusion becomes significant and the overall process is under the simultaneous control of pore diffusion and chemical reaction. The chemical activation energy, calculated from the data below 500°C, was 105 ± 15 kJ/mole, which is considerably higher than the value obtained by other authors, but not significantly higher than the value obtained herein for the uncoated particles.

3.5. Conclusions

The lack of a suitable model for the reduction of the superfine hematite particles implies that the process is more complex than previously reported for films and coarser particles or pellets. It is highly likely that competition between diffusion control and interfacial area control gives rise to the characteristic shape of the reaction profiles. It is hoped that modelling of the data will eventually be possible. In the meantime a relatively simplistic approach derives rate constants which are much lower than those reported in the literature. Since it is desirable to have high reduction rates so that the iron particles can be formed with minimal sintering, these low rate constants are unfortunate. It is unlikely that this approach to making superfine iron particles would be viable commercially.

4. PREPARATION AND PROPERTIES OF SUPERFINE IRON ALLOYS

Ultrafine particles (or thin films) of iron alloys are of considerable interest for several reasons, including:

1. Higher coercivities can be obtained with the right alloys
2. Greater resistance to oxidation can be achieved
3. Novel properties, e.g., the Kerr magneto-optic effect, are observed.

In this work we have studied the variation of coercivity with alloying additions to superfine iron particles using two systems, Fe-Co and Fe-Ni-Zn.

4.1. Iron-Cobalt (Fe-Co) Particles.

Iron-cobalt alloy particles were prepared by reduction of cobalt ferrites in hydrogen. The cobalt ferrite particles were prepared using the technique reported by Tamura and Matijevic[12]. The procedure is as follows. A mixture of 18 cm^3 of 4.22 M KOH and 30 cm^3 of 2 M KNO_3 were added to 200 cm^3 distilled water in a round-bottomed flask. Nitrogen gas was bubbled through the solution for two hours with stirring. A mixture of 5 cm^3 of 1 M $Co(NO_3)_2$ and 10 cm^3 of 1 M $FeSO_4$ were then added and the solution together with the gelatinous precipitate that forms was purged for another hour. The reaction vessel was then immersed in a preheated oil bath and maintained at 90°C for 24 hours. The ferrite particles formed were separated with a magnet while the supernatant was decanted off. Subsequent washing was performed by redispersion using an ultrasonic bath, and centrifugation. Reductions, coating (if done) and packaging were performed as described in Section 2.2.

Table 7. Preparation of cobalt ferrite particles.

Sample	[Co]/[Fe]	[KOH]/([Co]+[Fe])	Particle Size (μm)
CO-1	0.5	5.06	0.11 ±0.04
CO-2	0.5	2.53	0.07 ±0.03
CO-3	0.5	0.56	0.21 ±0.07
CO-4[*]	0.5	1.41	highly aggregated primary ~0.02-0.07
CO-5[†]	0.5	1.41	0.10 ±0.03
CO-6[†]	1.0	1.06	0.14 ±0.04

[*] Reactants were gradually heated to 90°C

[†] KOH/KNO_3 solution was preheated to 90°C before addition of Co and Fe

Table 7 contains a summary of the preparation conditions for the cobalt ferrite particles and Fig. 37 shows TEM's of the products. The particles have a much broader size distribution than the hematite particles shown in section 2.2, and the mean sizes are larger. The particles vary in size and shape depending on the preparation conditions. The highest [KOH]/([Co]+[Fe]) ratio (CO-1, Fig. 37a) produced nearly spherical particles with some fine whiskers. Smaller particles without the whiskers were formed at a lower base/metal ratio (CO-2, Fig. 37b) but further reducing this ratio below 1.0 led to much larger particles. Preparations wherein the KOH and KNO_3 solutions were preheated to 90°C yielded more cubic particles (CO-5, Fig. 37c).

Table 8 shows the reduction conditions and properties of the reduced particles. The addition of cobalt to submicron iron particles is known to enhance coercivity. For example, Luborsky and Paine[30] reported coercivities as high as 1400 Oe for 44%Fe-56%Co particles vs 800 Oe for iron particles prepared by electrodeposition in mercury. Kawasaki and Higuchi[31] found an enhancement in H_c for acicular particles containing 10-50% cobalt. They prepared their particles by precipitating

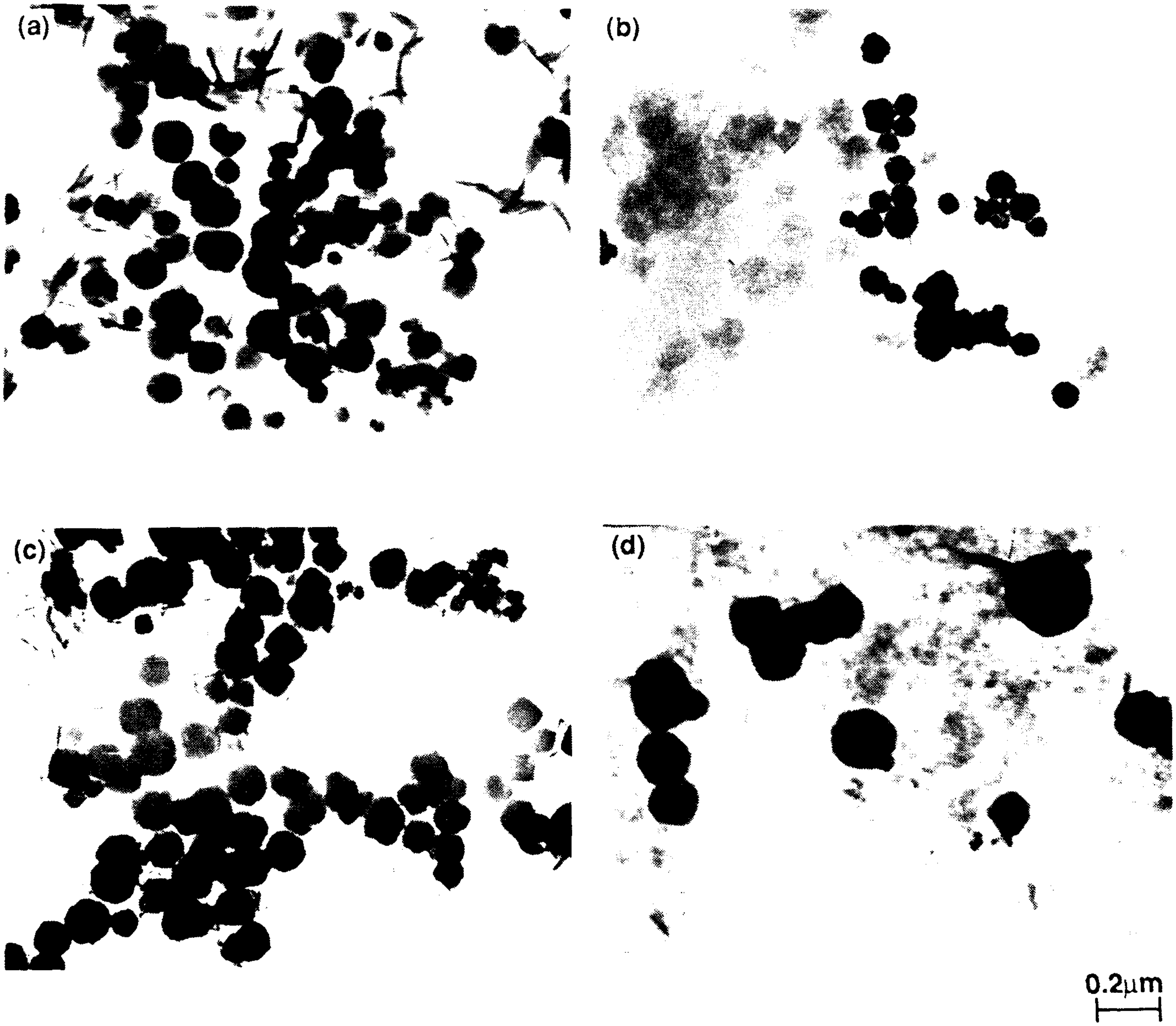

Figure 37. Transmission electron micrographs of cobalt ferrite particles: a) CO-1, b) CO-2, c) CO-5 and d) CO-6.

$Co(OH)_2$ onto goethite prepared by the standard method, heating the particles to 700°C to allow the cobalt to diffuse into the particles, and then reducing in hydrogen at 380°C for 6 h. Their work is at least comparable with the method reported here. It is therefore noteworthy that the H_c values reported in Table 8 are rather low. However, examination of Fig. 37 shows particle sizes ranging from 0.04 to 0.14 μm with the majority > 0.1 μm. These particles are too large to have high coercivities and certainly should not be compared with the iron particles discussed in section 2. Indeed for particles >0.1 μm Luborsky and Paine[30] did not find as dramatic a difference in H_c. Moreover their particles were not spherical, having axial ratios ~1.35, and the authors attributed effects on H_c to contributions to shape anisotropy.

Table 8. Properties of reduced cobalt ferrite particles.

Ferrite	Coating	Reduction conditions		Coercivity, H_c (Oe)	Magnetization, M_s (emu/g)
		T (°C)	Time (h)		
CO-1	none	400	1.0	496	100
CO-1	Na_2SiO_3	400	1.0	369	110
CO-2	none	400	1.0	498	59
CO-4	none	300	2.0	415	31
CO-4	none	400	1.0	89	87
CO-5	none	300	2.0	657	34
CO-5	none	400	1.0	233	61

The particles prepared herein are nominally spherical and outside the size range where interesting effects might be observed. Because, subsequent attempts to prepare smaller particles were not successful, this work was not continued.

4.2. Iron-nickel-zinc (Fe-Ni-Zn) particles

Nickel zinc ferrite ($Ni_xZn_{1-x}Fe_2O_4$) particles were prepared according to the method of Chen et al.[32] In this method a solution of ferric, nickel, and zinc nitrate is mixed with hydrazine hydrate ($4M$) and potassium hydroxide ($1M$). The resulting gelatinous precipitate is aged at 90°C for 1 h. The resulting magnetic particles are separated as described earlier. Particles used in this study were prepared with $[Me]_{tot} = 0.25\ M$, $[N_2H_4]/[Me]_{tot} = 1.33$, and $[KOH]/[N_2H_4] = 1.0$. Three ferrite compositions were prepared with $x = 0.80$, 0.65, and 0.50 and a TEM of each sample is shown in Fig. 38. The particles are highly aggregated but the primary particle sizes are as small as 100 Å. The aggregate size is approximately 1 μm. The $Ni_xZn_{1-x}Fe_2O_4$ particles were coated, reduced, and packaged as described for the hematite.

The first striking result is in the reaction kinetics. Whereas the reduction of hematite proceeded via a two-step process, the reduction of $Ni_xZn_{1-x}Fe_2O_4$ was a single step and was much more rapid as can be seen in Fig. 39, which shows TGA data for the reduction of hematite and $Ni_{0.65}Zn_{0.35}Fe_2O_4$ at approximately 330°C. Experimental parameters for the reduction of $Ni_{0.65}Zn_{0.35}Fe_2O_4$ are given in Table 9. The initial weight losses are a little higher than those listed in Table 1 for the hematite reductions. The stoichiometric weight loss for the reduction of $Ni_{0.65}Zn_{0.35}Fe_2O_4$ is 27% and whereas the values for Δw_r^{∞} (av.$=25.1 \pm 1.9$ %) are generally lower than this, the values for Δw_{tot} (av.$=27.5 \pm 0.9$ %) are higher. This behavior, like that of the hematite, is thought to result from loss of oxygen before the hydrogen is introduced. Figures 40 and 41 show fractional reduction curves for the ferrite. The α values were calculated as in Eq. 6, but the value of 27 % was used for Δw_r^{∞}. The curves for the higher temperatures (Fig. 41) show an initial "induction period" similar to that for the hematite, but only approximately 2 min

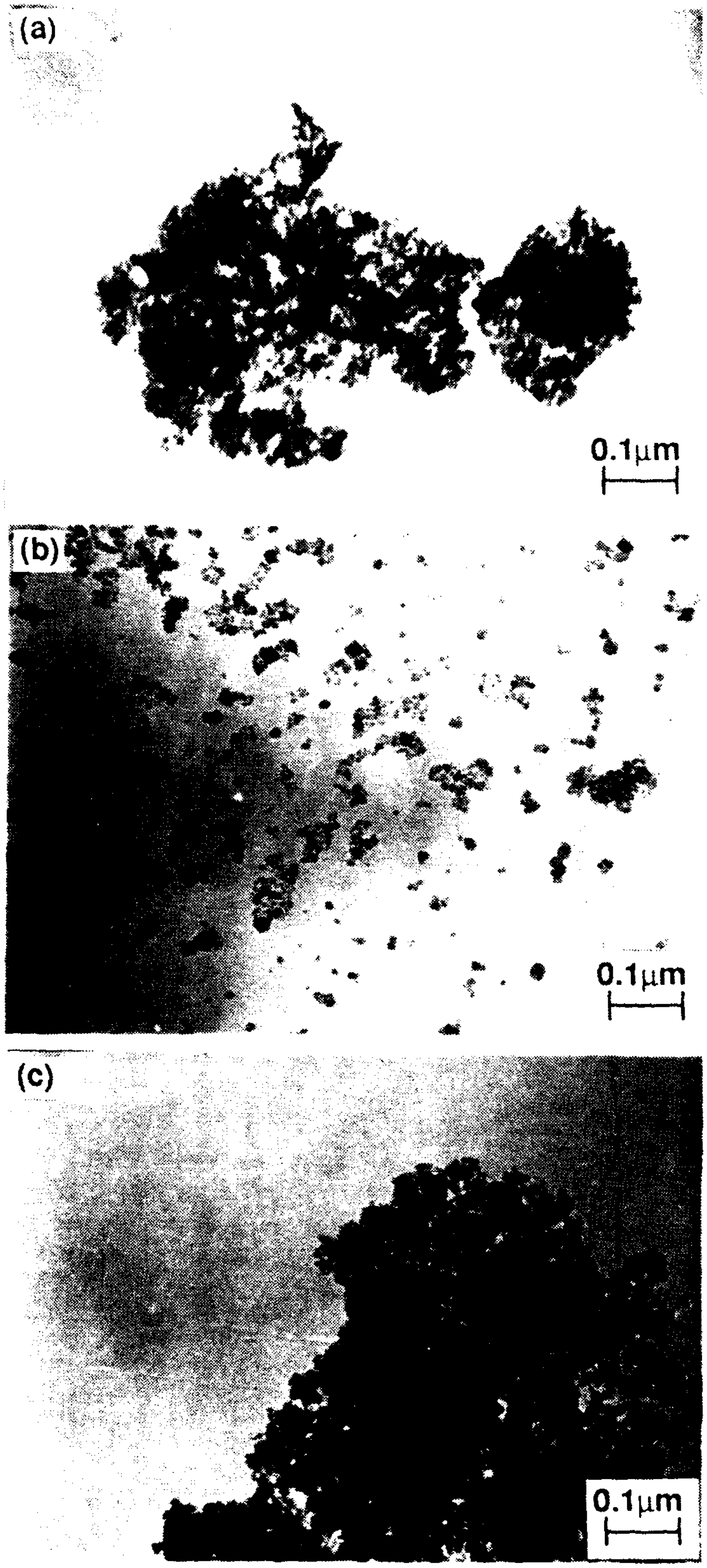

Figure 38. Transmission electron micrographs of nickel zinc ferrite particles ($Ni_xZn_{1-x}Fe_2O_4$) with x = a) 0.50, b) 0.65, and c) 0.80.

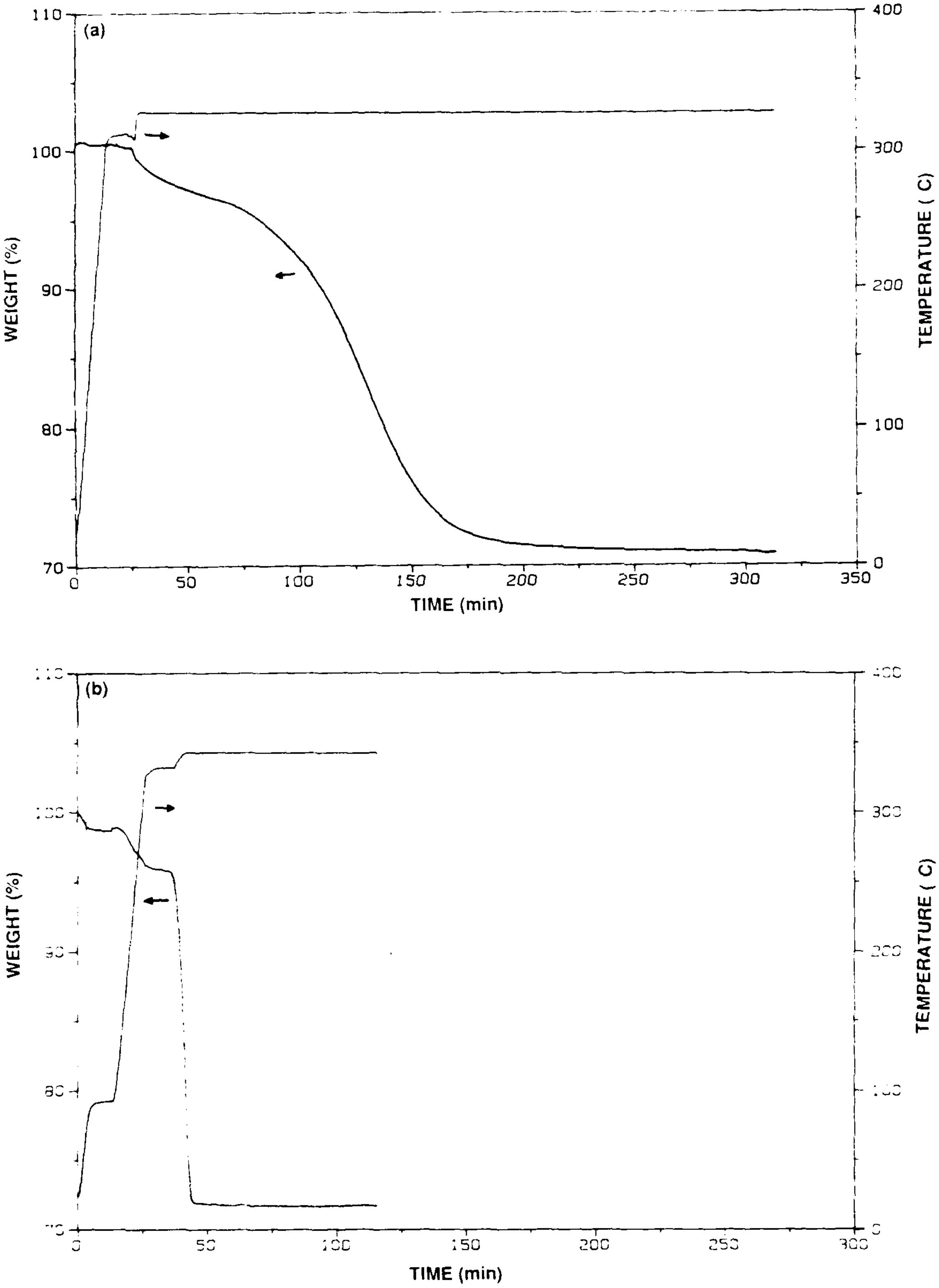

Figure 39. TGA plots of the reduction of uncoated a) hematite and b) nickel zinc ferrite particles by hydrogen at approximately 330°C.

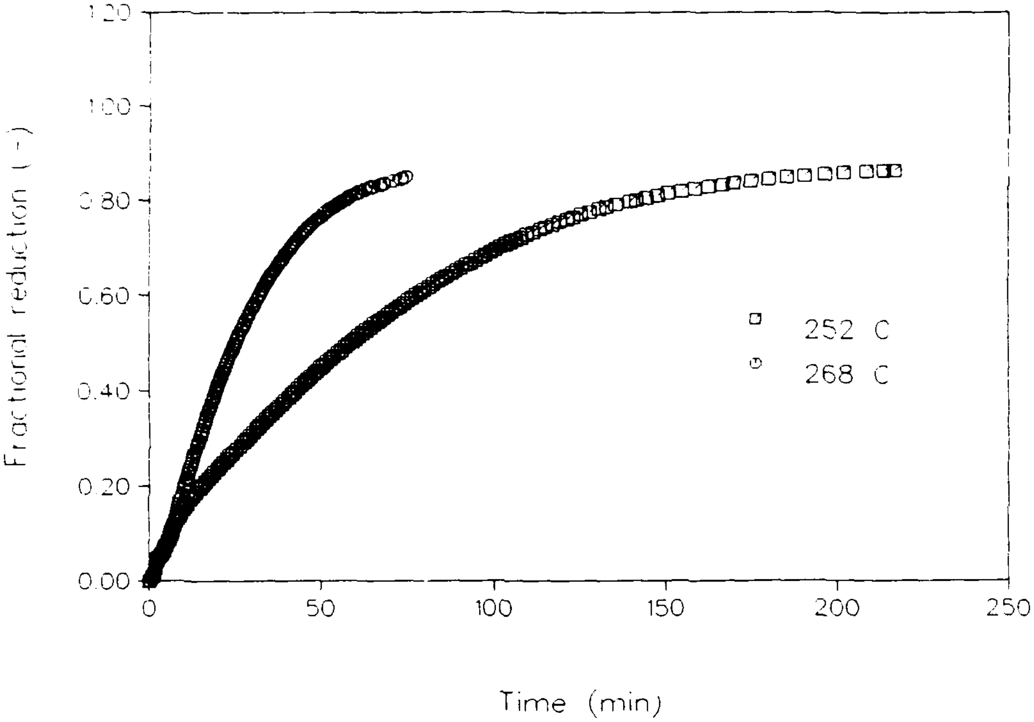

Figure 40. Reduction kinetics of uncoated $Ni_{0.65}Zn_{0.35}Fe_2O_4$ particles with pure hydrogen at 252 and 268°C.

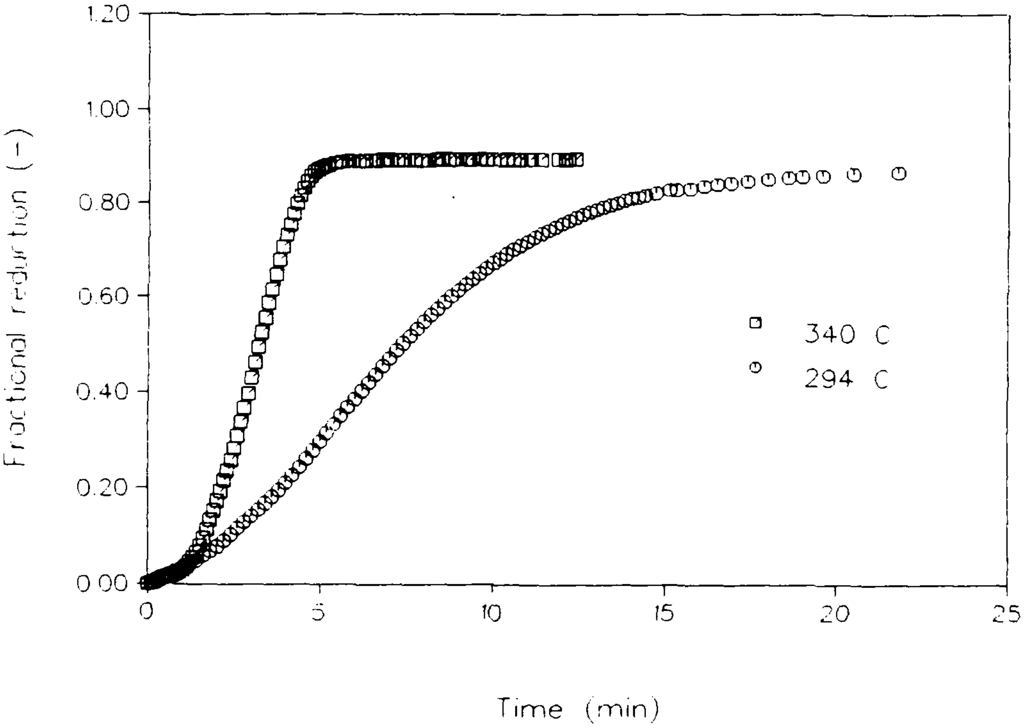

Figure 41. Reduction kinetics of uncoated $Ni_{0.65}Zn_{0.35}Fe_2O_4$ particles with pure hydrogen at 294 and 340°C.

Table 9. **Experimental data for the reduction of $Ni_{0.65}Zn_{0.35}Fe_2O_4$ with pure hydrogen.**

Run #	Temp. (°C)	w_0 (mg)	Δw_i (%)	Δw_r^* (%)	Δw_{tot} (%)	t_r (min)
54-17	252	8.27	3.5	23.3	26.8	>217
54-12	268	6.07	4.5	23.0	27.5	>76
54-25	278	4.74	1.2	26.0	27.2	170
54-10	294	4.53	3.4	23.6	27.0	>23
54-23	311	4.68	2.7	27.3	29.0	143
54-16	327	4.32	0.8	26.0	26.8	>25
54-13	340	7.87	4.3	23.9	28.2	14
54-14	340	5.26	3.4	24.2	27.6	12
54-11	432	2.94	0.0	28.8	28.8	20
54-15	437	5.71	1.3	24.7	26.0	>8

in duration which is similar to the mixing time for the introduction of hydrogen. Thus, the "induction periods" shown in Fig. 41 are presumably artifacts representing the mixing of the gasses. The induction period in the reduction of hematite has been attributed to the formation of iron nuclei[23]. It will be shown later in this report that the absence of this induction period is very important. The curves do not go to as sharp a completion as did the hematite ones and consequently the values for the reduction time t_r are rather inexact. Indeed the curves, especially for the lower temperatures, appear exponential in nature.

Table 10 shows kinetic parameters for the reduction of $Ni_{0.65}Zn_{0.35}Fe_2O_4$. The k_1 values were obtained from an exponential fit to the data, omitting the first 3 min during which mixing occurs. They, rather than k_{obs}, were used to calculate k_r, because the curves did not all show a linear region in the middle of the reaction period as was observed in the reduction of hematite. This makes the values of k_{obs}

Table 10. Kinetic parameters for the reduction of uncoated $Ni_{0.65}Zn_{0.35}Fe_2O_4$ with pure hydrogen.

Run #	Temp. (°C)	$k_{obs} \times 10^3$ (s^{-1})	$k_1 \times 10^3$ (s^{-1})	$\bar{k}_s \times 10^6$ (g atom O m^{-2} s^{-1} atm^{-1})
54-17	252	0.120	0.217	0.069
54-12	268	0.372	0.593	0.189
54-25	278	0.309	0.495	0.158
54-10	294	1.45	1.93	0.615
54-23	311	1.23	2.31	0.735
54-16	327	2.12	3.23	1.03
54-13	340	5.16	6.08	1.94
54-11	432	5.47	9.98	3.18
54-15	437	9.10	8.08	2.57

somewhat suspect. It is noteworthy that in every case but #54-15 k_1 is larger than k_{obs} which is to be expected for an exponential reaction since k_1 corresponds to the initial slope of the curve (assuming instantaneous mixing). The BET surface area used in calculating $\bar{k}_s$ was 53 m^2/g. Figure 42 is an Arrhenius plot for the ferrite reduction. It appears that a transition in reaction control occurs above 340°C. The activation energy for the lower temperature region is 97 ± 10 kJ/mole.

Table 11 shows magnetic data obtained for the reduced ferrite particles. The coercivities obtained depend strongly on the reduction conditions and the highest values are similar to those obtained from the superfine iron particles. Unlike the iron particles, however, the coercivities in some instances increase with increasing reduction temperature or time. This appears to be correlated with the degree of crystallinity in the reduced metal as can be seen in Fig. 43, which shows XRD patterns for the particles of $Ni_{0.5}Zn_{0.5}Fe_2$ as a function of reduction temperature and

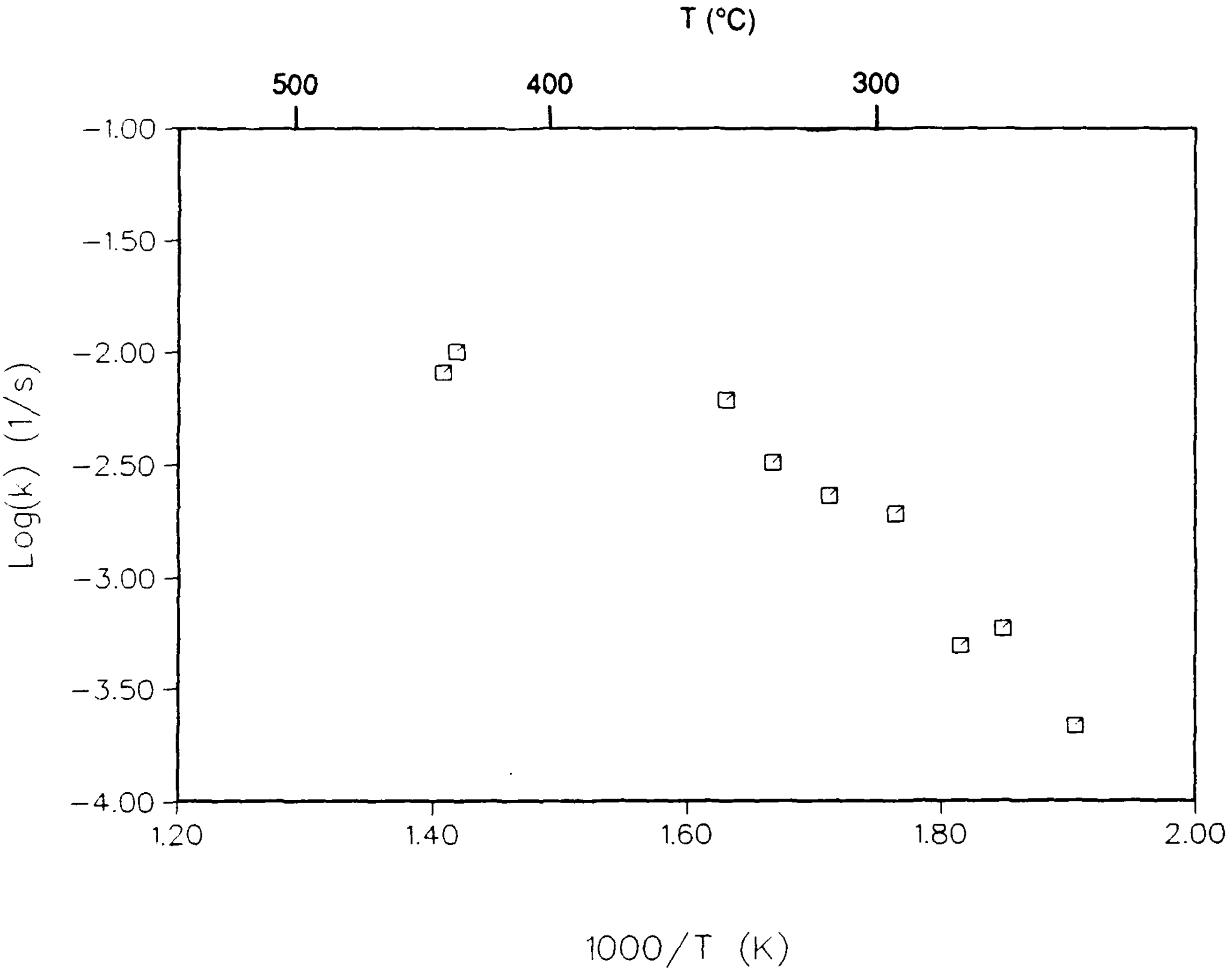

Figure 42. Arrhenius plot for the reduction of uncoated $Ni_{0.65}Zn_{0.35}Fe_2O_4$ particles.

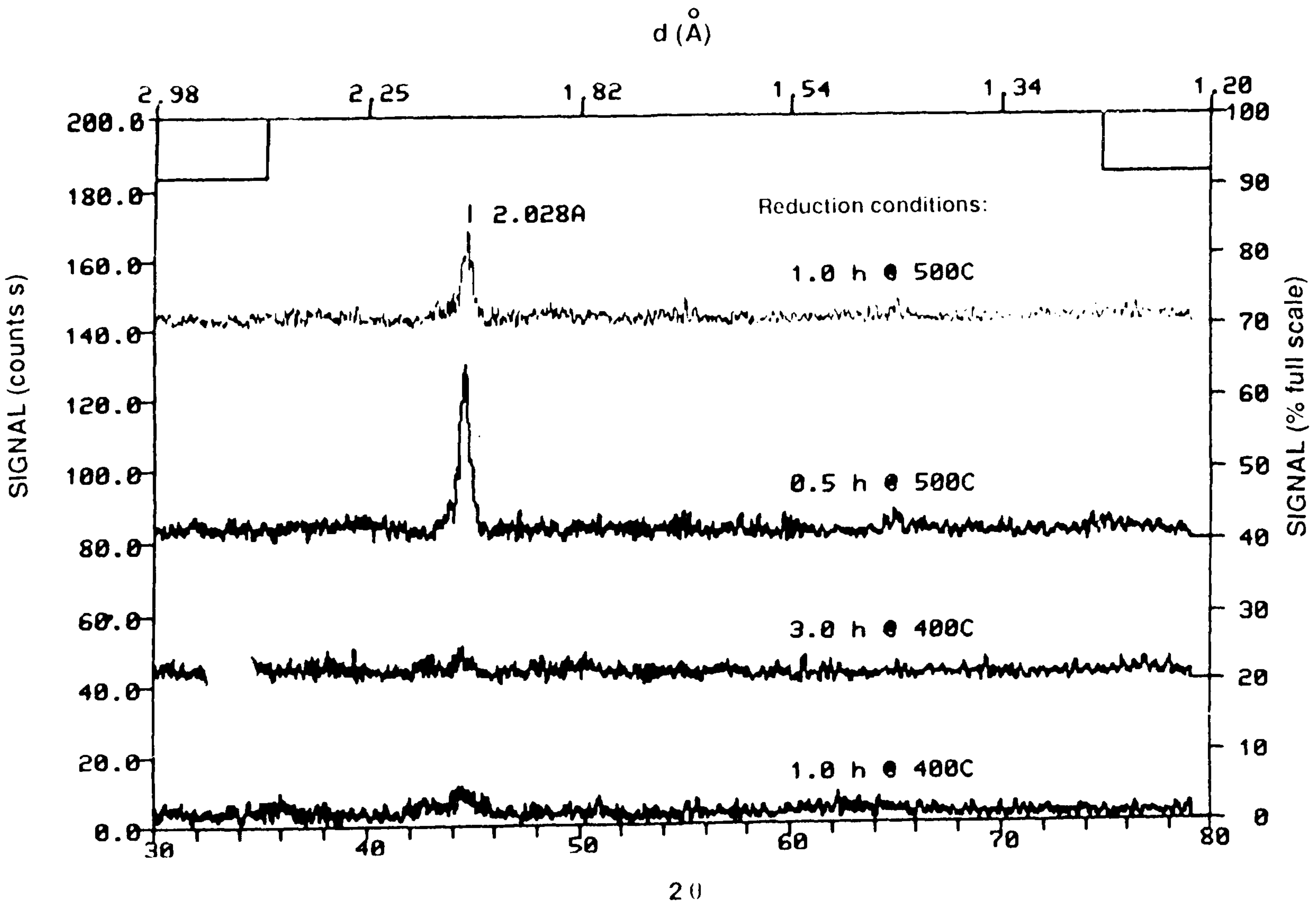

Figure 43. X-ray diffraction patterns of Na_2SiO_3-coated $Ni_{0.5}Zn_{0.5}Fe_2O_4$ after reduction in pure hydrogen under varying conditions.

time. The particles reduced at 400°C for 1 and 3 hours are essentially amorphous with just a hint of a peak at 2.038 Å.

Table 11. Magnetic properties of $Ni_xZn_{(1-x)}Fe_2O_4$ after reduction.

Coating/(ID #)	x	Reduction temp. (°C)	Reduction time (h)	Coercivity, H_c (Oe)	Magnetization σ (emu/g)
Uncoated:					
(29-2)	0.80	400	2.0	609	97
(30-2)	0.80	500	1.0	282	81
(32-2)	0.80	600	0.5	melted	
	0.65	275	3.0	225	66
	0.65	300	3.0	546	112
	0.65	400	3.0	376	133
(26-2)	0.50	400	1.0	374	65
(24-2)	0.50	400	3.0	517	85
(25-2)	0.50	500	0.5	652	
(27-2)	0.50	500	1.0	601	117
Na_2SiO_3:					
(29-1)	0.80	400	2.0	525	120
(30-1)	0.80	500	1.0	224	84
(32-1)	0.80	600	0.5	87	79
(26-1)	0.50	400	1.0	284	46
(24-1)	0.50	400	3.0	345	73
(25-1)	0.50	500	0.5	624	
(27-1)	0.50	500	1.0	590	102

The kinetics as measured by TGA indicate that the reduction should have gone to completion within 10 min at 400°C. This implies that the reduction proceeds by a rapid chemical step producing crystallites so small as to be amorphous to X-rays, followed by a slower step involving recrystallization/growth of these superfine crystallites, i.e.,:

$$Ni_xZn_{1-x}Fe_2O_4 + 4H_2 \rightarrow Ni_xZn_{1-x}Fe_2(\text{amorph}) + 4H_2O \qquad \text{(rapid)}$$

$$Ni_xZn_{1-x}Fe_2(\text{amorph}) \rightarrow Ni_xZn_{1-x}Fe_2(c). \qquad \text{(slow)}$$

All the weight loss occurs during the rapid chemical reaction shown in the first step, so this is the reaction followed by the TGA. The slower recrystallization step takes place without weight loss and so is not recorded by TGA. The TGA data did not show the induction period associated with nucleation which should have been detected. Thus, it is reasonable to assume that the above model is correct. This finding is partially supported by the Mössbauer data shown in Fig. 44. These spectra show that even after 3 h at 275°C the iron is essentially in the metallic form. However, the signals are much weaker than the carbonyl iron powder (CIP) used as a reference. It should be noted, however, that the CIP film had approximately 3× the amount of particles that was in the reduced ferrite films. Mossbauer spectra of the Na_2SiO_3-coated samples of $Ni_{0.5}Zn_{0.5}Fe_2$ (#24-1 and #27-1) show >80% iron as metallic Fe with an unidentified second phase -- no iron oxide split peaks were detected.

The amorphous metal powders prepared under the milder reduction conditions exhibit lower coercivities than the crystalline particles that are formed as the reduction temperature or time is increased. The magnetizations do not show any trend. The effect is more pronounced with the higher zinc content. It is feasible that the zinc is forming a barrier to crystallization of the iron and nickel. This could be due to incomplete reduction of the zinc. Figure 45 shows an Ellingham diagram for the reduction of ZnO to Zn by hydrogen. It is seen that reduction is only favored above 550°C for $p_{H_2O}/p_{H_2} = 10^{-4}$ (100 ppm) and only above 350 °C for $p_{H_2O}/p_{H_2} = 10^{-6}$ (1 ppm). It is likely that the water content in the gas stream falls

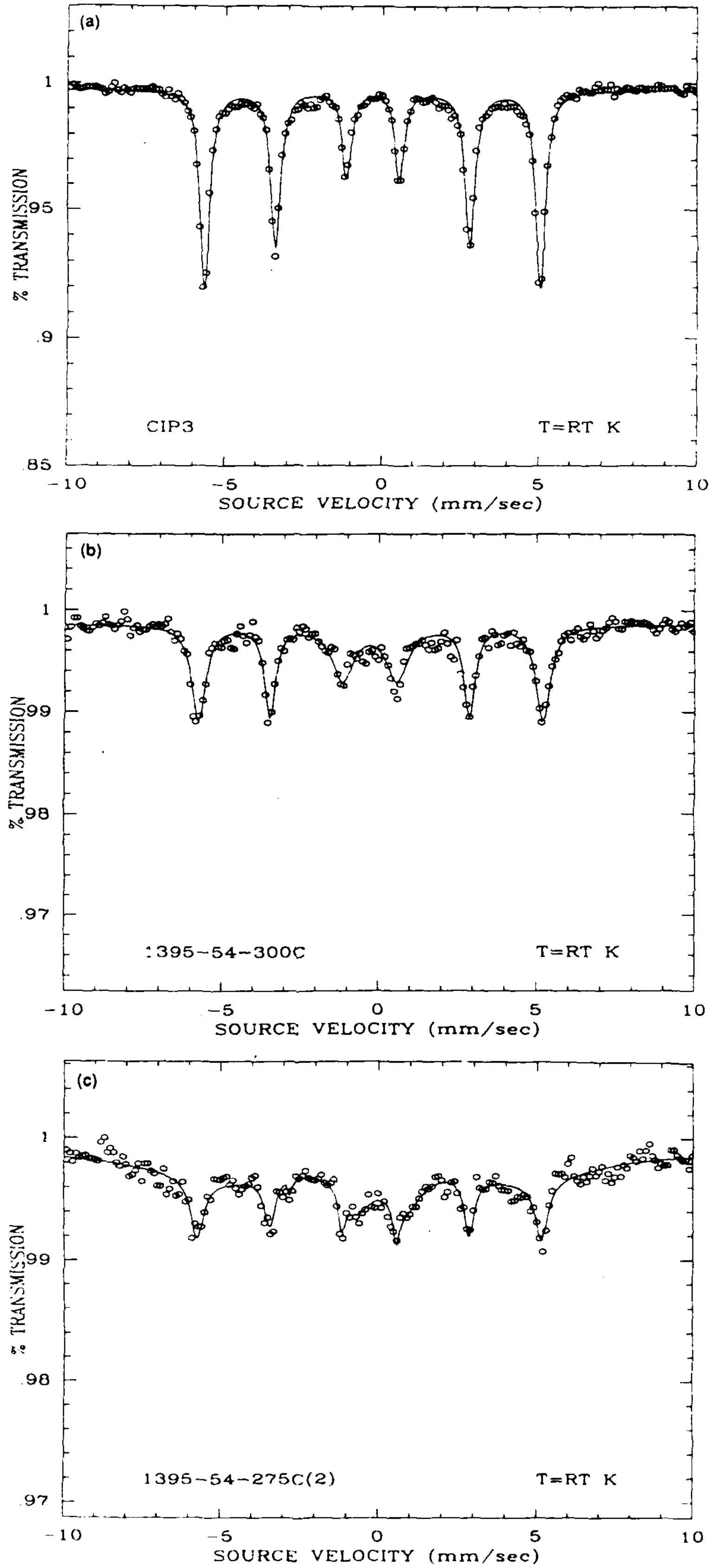

Figure 44. Mössbauer spectra for a) carbonyl iron powder (reference) and for $Ni_{0.65}Zn_{0.35}Fe_2O_4$ after reduction at b) 300°C and c) 275°C for 3 h.

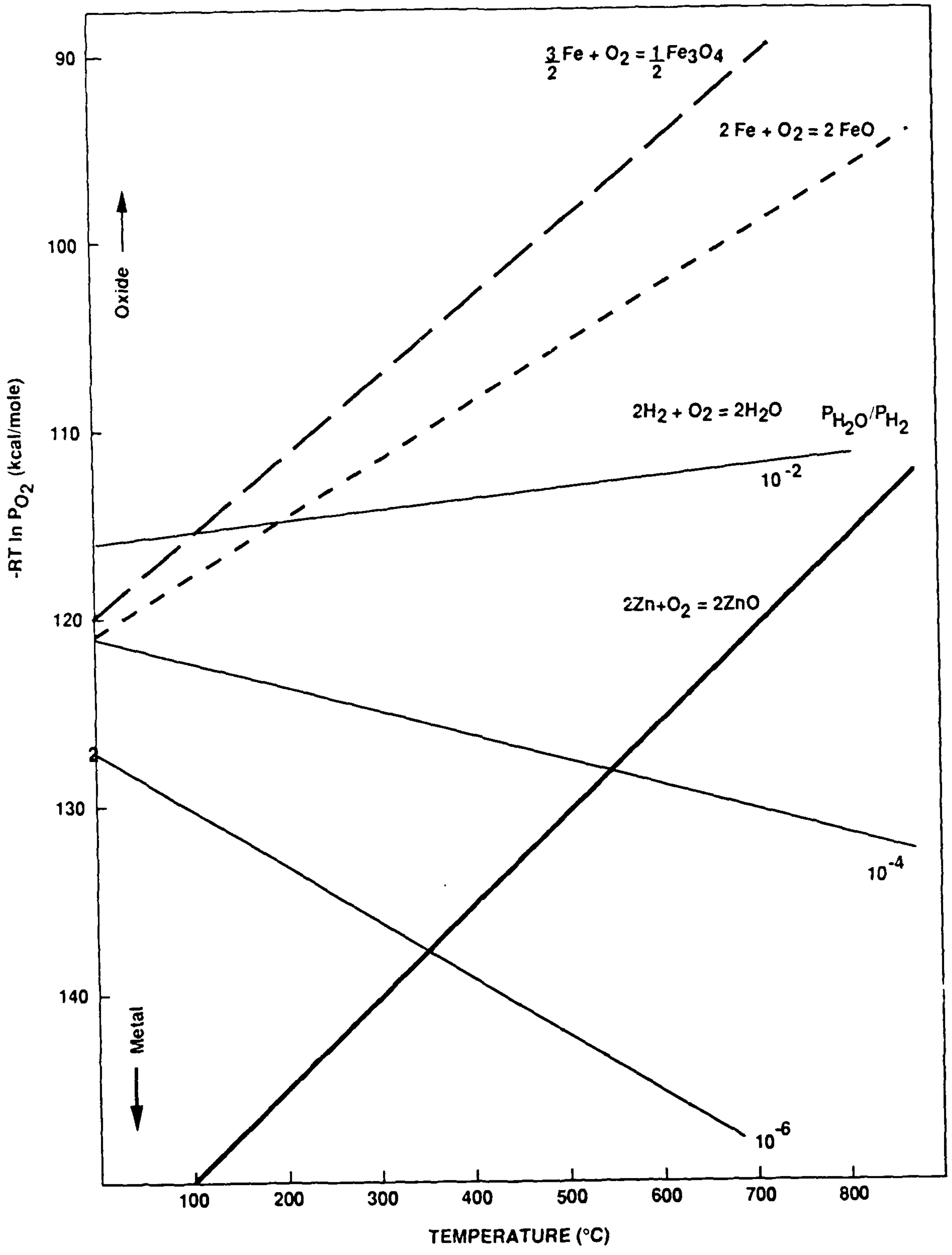

Figure 45. Ellingham diagram for the reduction of crystalline ZnO by hydrogen.

somewhere between these limits and so it is certainly possible that ZnO would not be reduced under the experimental conditions. However, these thermodynamic data refer to crystalline ZnO and it is not apparent that reduction of $Ni_xZn_{1-x}Fe_2O_4$ would lead to crystalline ZnO. Calculations of the weight losses from reduction of $Ni_xZn_{1-x}Fe_2O_4$ assuming first complete reduction and second (1-x)ZnO remains are tabulated in Table 12. The possible reactions are:

$$Ni_xZn_{1-x}Fe_2O_4 + 8H_2 = xNi + (1-x)Zn + 2Fe + 4H_2O$$

or

$$Ni_xZn_{1-x}Fe_2O_4 + (6+2x)H_2 = xNi + (1-x)ZnO + 2Fe + (3+x)H_2O.$$

Experimental values for the limiting extent of reaction at 400°C, included in Table 12 for comparison, were calculated assuming that Δw_i consists entirely of volatile impurities.

Table 12. Calculated weight losses for reduction of nickel zinc ferrite

x	Calc. wt. loss (%)		Limit extent of reaction, α		
	ZnO remains	Stoichiometric	ZnO remains	Stoichiometric	Exp.
0.50	23.6	26.9	0.877	1.000	0.95
0.65	24.7	27.0	0.915	1.000	0.95
0.80	25.8	27.1	0.952	1.000	

It is seen from Table 12 that, given the assumption, the reductions do not proceed to completion but rather the reaction ends with the zinc only partially reduced. This may explain the amorphous nature of the particles formed. The ZnO would be uniformly distributed throughout the powder so it can form a barrier to crystallization of the iron and nickel. However, this does depend upon the assumption that Δw_i represents a loss of impurities. Reference to Table 9 clearly shows that if Δw_i represents oxygen loss prior to the introduction of hydrogen then the samples go to complete reduction.

Figures 46-48 are TEM's of the metal particles formed. The powders containing the most Zn (i.e., x=0.5) show little variation in morphology with increasing reduction temperature and time. These powders have maintained the sponge-like nature, seen in the original ferrite powder, that arises from the aggregation of large numbers of superfine particles. The primary particle size in these samples ranges from 15-30 nm. It is noteworthy that the coercivities of the powders reduced at 500°C (Fig. 46 c and d) are considerably higher than those reduced at 400°C. As mentioned above this appears to correlate more with the degree of crystallinity than with the morphology. Powders containing the lesser amounts of Zn (i.e., x=0.8 or 0.65) exhibit more grain growth on reduction, Fig. 47 and 48. For x=0.8 the primary particles range between 15 - 30 nm after reduction at 400°C and between 15 - 60 nm after reduction at 500°C. For x=0.65 the primary particles range between 15 - 30 nm after reduction at 275°C and between 20 - 60 nm after reduction at 300°C. The sponge-like nature is not as evident in these samples and there are more individual particles as well as an appreciable amount of aggregation.

The x=0.65 and 0.8 powders gave higher magnetizations and greater degrees of crystallinity at lower reduction temperatures and times than the x=0.5 material. Indeed the 0.8 powders began to form the FeNi alloy phase after reduction at 500°C, and at 600°C for 0.5 h the uncoated powder melted but the Na_2SiO_3-coated material did not and it was found to consist entirely of the FeNi alloy phase, as can be seen from the XRD patterns in Fig. 49. It should be noted

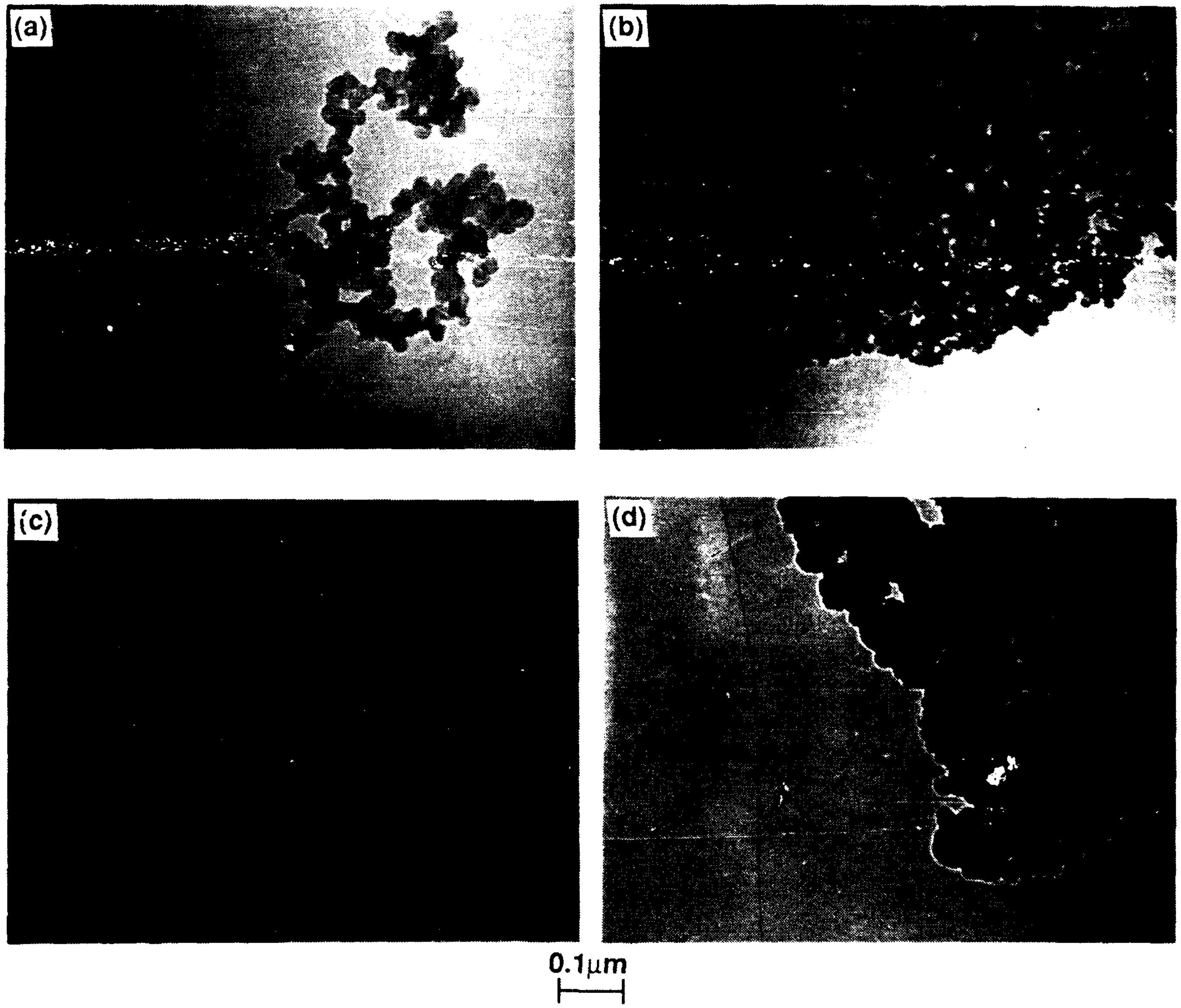

Figure 46. Transmission electron micrographs of nickel zinc ferrite particles ($Ni_{0.5}Zn_{0.5}Fe_2O_4$) reduced a) 1 h at 400°C, b) 3 h at 400°C, c) 0.5 h at 500°C, and d) 1 h at 500°C.

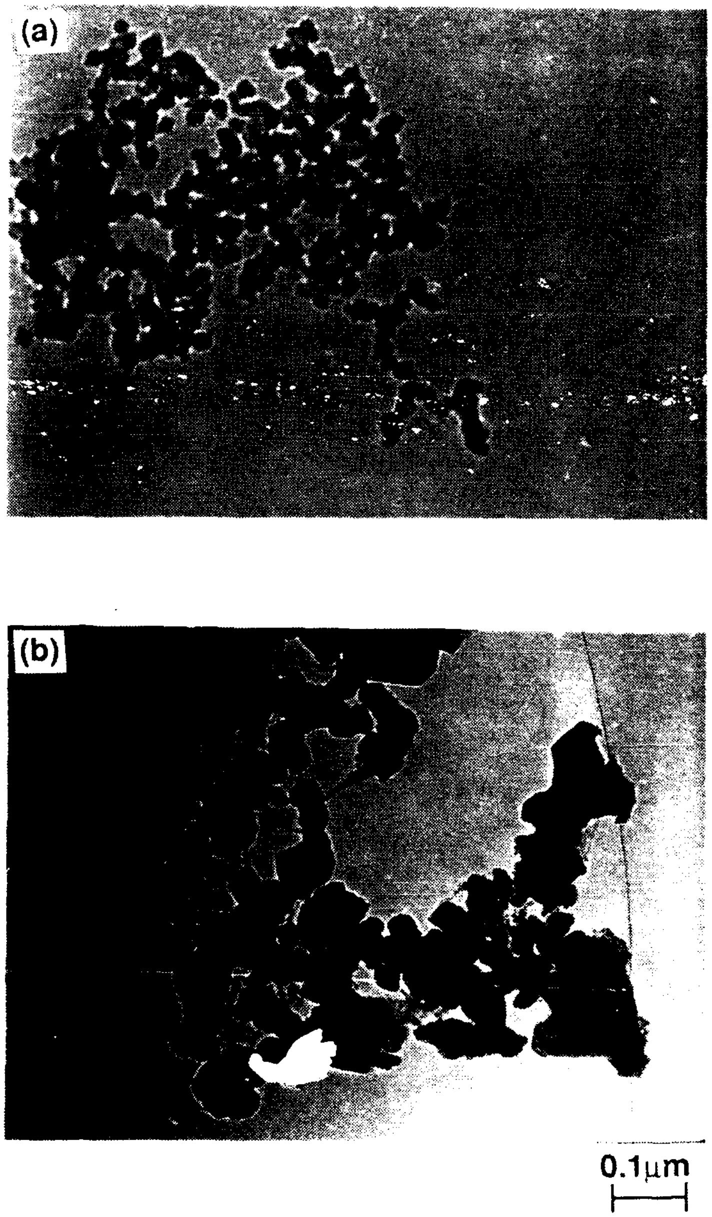

Figure 47. Transmission electron micrographs of nickel zinc ferrite particles ($Ni_{0.65}Zn_{0.35}Fe_2O_4$) reduced a) 3 h at 275°C, and b) 3 h at 300°C.

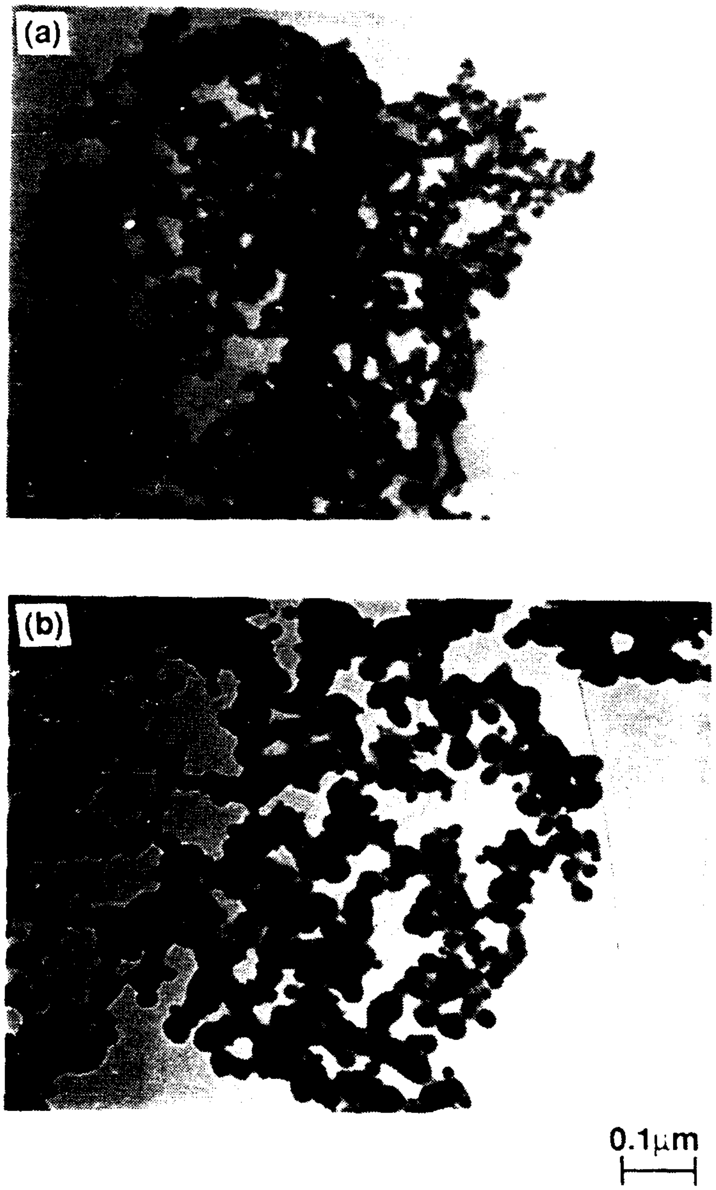

Figure 18. Transmission electron micrographs of nickel zinc ferrite particles ($Ni_{0.8}Zn_{0.2}Fe_2O_4$) reduced a) 2 h at 400°C and b) 1 h at 500°C.

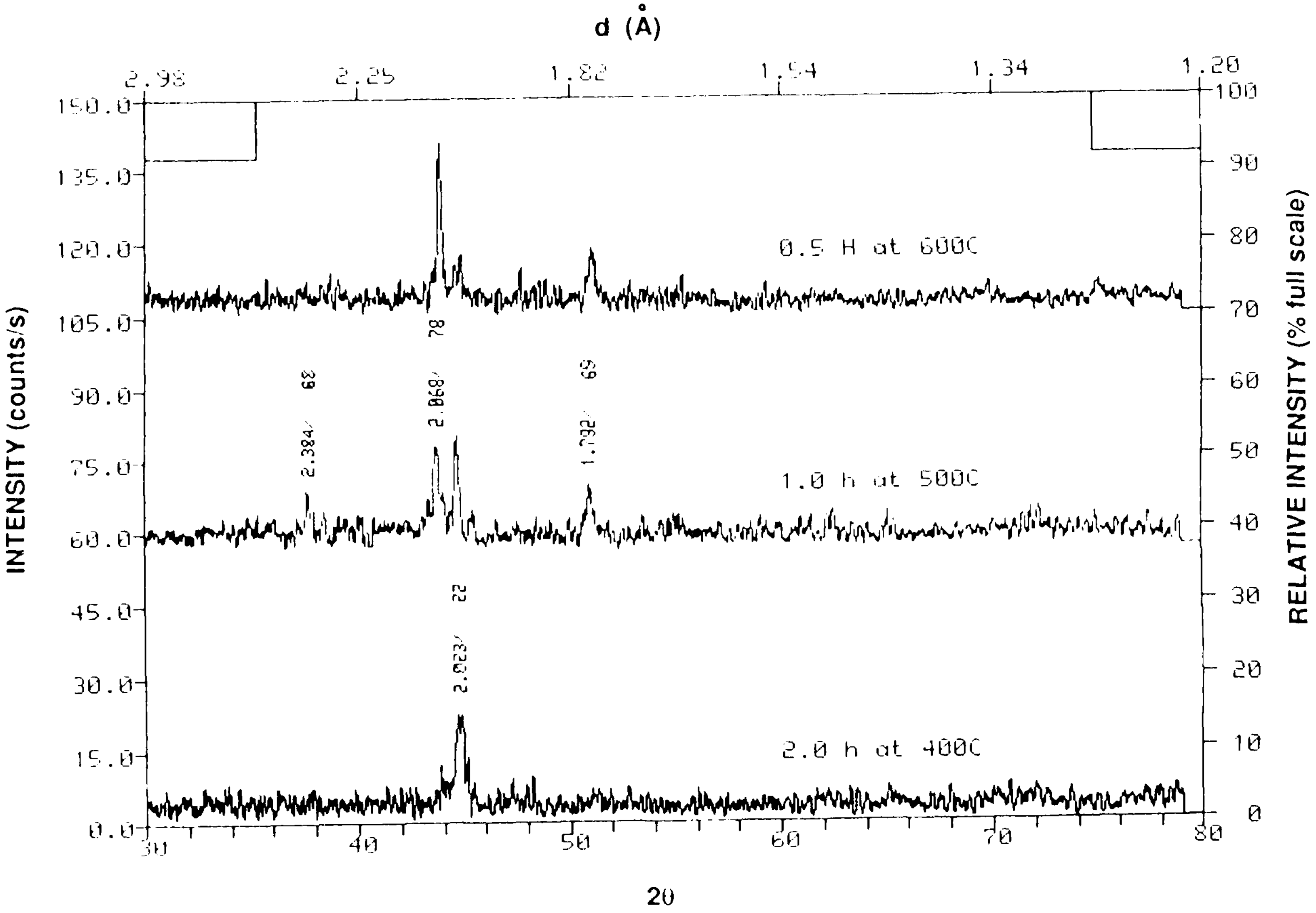

Figure 49. X-ray diffraction patterns of Na_2SiO_3-coated $Ni_{0.8}Zn_{0.2}Fe_2O_4$ after reduction in pure hydrogen under varying conditions.

AD-A211 661 THE PREPARATION AND PROPERTIES OF SUPERFINE METAL 2/2
PARTICLES(U) MARTIN MARIETTA LABS BALTIMORE MD
K BRIDGER 15 JUN 88 MML-TR-89-78C N00014-85-C-0637
UNCLASSIFIED F/G 11/7 NL

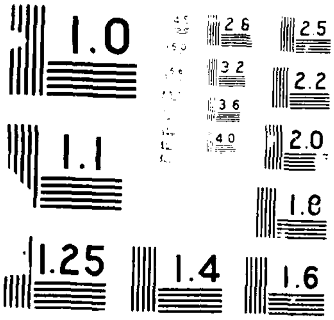
1.0
2.8
2.5
3.2
2.2
3.6
4.0
2.0
1.1
1.8
1.25
1.4
1.6

from Table 11 that this alloy phase has both lower coercivity and magnetization than the cubic iron.

The additions of nickel and zinc to the superfine iron particles do not seem to have enhanced the coercivities. In each case the limiting coercivity reached is approximately that of the 0.05-μm iron particles discussed in Chapter 2. However, the rates of reduction of the ferrite particles are very encouraging and given these rates it is much easier to prepare the superfine metal particles from the oxide. Obviously other alloying elements should be tried or else the oxides should be prepared by a different technique. For example, the alloying elements might only enhance coercivity when present at the surface of the particles. Therefore, it might be of interest to prepare magnetite Fe_3O_4 particles, coprecipitate the other oxides on the surface of these particles, and then reduce the coated magnetite particles. If such a process produced metal particles with enhanced coercivities, it would provide great insight into the mechanism by which the "alloying" elements enhance coercivity as well as provide a route to a potentially useful recording material.

5. REFERENCES

1. G. Bate in *Ferromagnetic Materials, Vol. 2*, E.P. Wohlfarth ed., North-Holland, New York (1980) p. 381.
2. K. Bridger, *MML TR 86-73c, Annual Report No. 1*, ONR Contract N00014-85-C-0637 (NR 653-047) (1986).
3. K. Bridger, *MML TR 87-75c, Annual Report No. 2*, ONR Contract N00014-85-C-0637 (NR 653-047) (1986).
4. K. Bridger et al., J. Appl. Phys., **61**, 3323 (1987).
5. K. Bridger, J. Watts and C.L. Chien, J. Appl. Phys., **63**, 3233 (1988).
6. (a) E. Matijevic, Langmuir, **2**, 12 (1986); (b) E. Matijevic, Acc. Chem. Res., **14**, 22 (1981).
7. E. Matijevic and P. Scheiner, J. Coll. Int. Sci., **63**, 509 (1978).
8. S. Hamada and E. Matijevic, J. Coll. Int. Sci., **84**, 274 (1981).
9. M. Ozaki, S. Kratohvil, and E. Matijevic, J. Coll. Int. Sci., **102**, 146 (1984).
10. T. Sugimoto and E. Matijevic, J. Coll. Int. Sci., **74**. 227 (1980).
11. R.S. Sapieszko and E. Matijevic, J. Coll. Int. Sci., **74**, 405 (1980).
12. H. Tamura and E. Matijevic, J. Coll. Int. Sci., **90**, 100 (1982).
13. A.E. Regazzoni and E. Matijevic, Corrosion, **38**, 212 (1982).
14. H. Naono and R. Fujiwara, J. Coll. Int. Sci., **73**, 406 (1980).
15. S. Hirokawa, T. Naito and T. Yamaguchi, J. Coll. Int. Sci.,**112**, 268 (1986).
16. T. Sueyoshi, K. Tashita, S. Hirai, M. Kishimoto, Y. Hayashi and M. Amemiya, J. Appl. Phys. **53**, 2570 (1982).
17. B.C. Lippens, B.G. Linsen and J.H. DeBoer, J. Catal., **3**, 32 (1964).
18. B.C. Lippens and J.H. DeBoer, J. Catal., **4**, 319 (1965).
19. J.H. DeBoer et al., J. Coll. Int. Sci., **21**, 405 (1966).
20. O. Fujii and Y. Hiraga, Japanese Patent, Application # 57 (1982)-7566.

21 A.A. Van der Giessen and G.J. Klomp, IEEE Trans. Mag., **MAG-5**, 317 (1969).

22. A.A. Van der Giessen, IEEE Trans. Mag., **MAG-9**, 191 (1973).

23. Y.K. Rao and M. Moinpour, Met. Trans. B, **14B**, 711 (1983).

24. J.H. Flynn and L.A. Wall, Polymer Lett., **19**, 323 (1966).

25. W.M. McKewan, Trans. Metallurg. Soc. AIME, **212**, 791 (1958).

26. W.M. McKewan, Trans. Metallurg. Soc. AIME, **218**, 2 (1960).

27. Wei-Kao Lu, Trans. Metallurg. Soc. AIME, **227**, 203 (1963).

28. E.T. Turkdogan and J.V. Vinters, Met. Trans., **3**, 1561 (1971).

29. W.A. Lloyd and N.R. Amundson, Ind. Eng. Chem., **53**, 19 (1961).

30. F.E. Luborsky and T.O. Paine, J. Appl. Phys. **31**, 68S (1960).

31. M. Kawasaki and S. Higuchi, IEEE Trans., **MAG-8**, 430 (1972).

32. C.J. Chen, K. Bridger, S.R. Winzer, and V. PaiVerneker, J. Appl. Phys., **63**, 3786 (1988).

END
FILMED
10-89
DTIC